



National Library
of Canada

Acquisitions and
Bibliographic Services Branch

395 Wellington Street
Ottawa, Ontario
K1A 0N4

Bibliothèque nationale
du Canada

Direction des acquisitions et
des services bibliographiques

395, rue Wellington
Ottawa (Ontario)
K1A 0N4

Your file Votre référence

Our file Notre référence

NOTICE

The quality of this microform is heavily dependent upon the quality of the original thesis submitted for microfilming. Every effort has been made to ensure the highest quality of reproduction possible.

If pages are missing, contact the university which granted the degree.

Some pages may have indistinct print especially if the original pages were typed with a poor typewriter ribbon or if the university sent us an inferior photocopy.

Reproduction in full or in part of this microform is governed by the Canadian Copyright Act, R.S.C. 1970, c. C-30, and subsequent amendments.

AVIS

La qualité de cette microforme dépend grandement de la qualité de la thèse soumise au microfilmage. Nous avons tout fait pour assurer une qualité supérieure de reproduction.

S'il manque des pages, veuillez communiquer avec l'université qui a conféré le grade.

La qualité d'impression de certaines pages peut laisser à désirer, surtout si les pages originales ont été dactylographiées à l'aide d'un ruban usé ou si l'université nous a fait parvenir une photocopie de qualité inférieure.

La reproduction, même partielle, de cette microforme est soumise à la Loi canadienne sur le droit d'auteur, SRC 1970, c. C-30, et ses amendements subséquents.

**A Finite Element Calculation Method for the Heat Transfer Effects on the
Current-Carrying Capacity of Underground Electrical Cables**

Mohamed Chaaban

**A Thesis
in
The Department
of
Mechanical Engineering**

**Presented in Partial Fulfillment of the Requirements
for the Degree of Doctor of Philosophy at
Concordia University
Montréal, Québec, Canada**

March 1995

© Mohamed Chaaban



National Library
of Canada

Acquisitions and
Bibliographic Services Branch

395 Wellington Street
Ottawa, Ontario
K1A 0N4

Bibliothèque nationale
du Canada

Direction des acquisitions et
des services bibliographiques

395, rue Wellington
Ottawa (Ontario)
K1A 0N4

Your file *Votre référence*

Our file *Notre référence*

THE AUTHOR HAS GRANTED AN
IRREVOCABLE NON-EXCLUSIVE
LICENCE ALLOWING THE NATIONAL
LIBRARY OF CANADA TO
REPRODUCE, LOAN, DISTRIBUTE OR
SELL COPIES OF HIS/HER THESIS BY
ANY MEANS AND IN ANY FORM OR
FORMAT, MAKING THIS THESIS
AVAILABLE TO INTERESTED
PERSONS.

L'AUTEUR A ACCORDE UNE LICENCE
IRREVOCABLE ET NON EXCLUSIVE
PERMETTANT A LA BIBLIOTHEQUE
NATIONALE DU CANADA DE
REPRODUIRE, PRETER, DISTRIBUER
OU VENDRE DES COPIES DE SA
THESE DE QUELQUE MANIERE ET
SOUS QUELQUE FORME QUE CE SOIT
POUR METTRE DES EXEMPLAIRES DE
CETTE THESE A LA DISPOSITION DES
PERSONNE INTERESSEES.

THE AUTHOR RETAINS OWNERSHIP
OF THE COPYRIGHT IN HIS/HER
THESIS. NEITHER THE THESIS NOR
SUBSTANTIAL EXTRACTS FROM IT
MAY BE PRINTED OR OTHERWISE
REPRODUCED WITHOUT HIS/HER
PERMISSION.

L'AUTEUR CONSERVE LA PROPRIETE
DU DROIT D'AUTEUR QUI PROTEGE
SA THESE. NI LA THESE NI DES
EXTRAITS SUBSTANTIELS DE CELLE-
CI NE DOIVENT ETRE IMPRIMES OU
AUTREMENT REPRODUITS SANS SON
AUTORISATION.

ISBN 0-612-01281-6

Name CHAABAN MOHAMED

Dissertation Abstracts International is arranged by broad, general subject categories. Please select the one subject which most nearly describes the content of your dissertation. Enter the corresponding four-digit code in the spaces provided.

Heat and Thermodynamics

SUBJECT TERM

0348

SUBJECT CODE

U·M·I

Subject Categories

THE HUMANITIES AND SOCIAL SCIENCES

COMMUNICATIONS AND THE ARTS

Architecture 0729
Art History 0377
Cinema 0900
Dance 0378
Fine Arts 0357
Information Science 0723
Journalism 0391
Library Science 0399
Mass Communications 0708
Music 0413
Speech Communication 0459
Theater 0465

EDUCATION

General 0515
Administration 0514
Adult and Continuing 0516
Agricultural 0517
Art 0273
Bilingual and Multi-cultural 0282
Business 0688
Community College 0275
Curriculum and Instruction 0727
Early Childhood 0518
Elementary 0524
Finance 0277
Guidance and Counseling 0519
Health 0680
Higher 0745
History of 0520
Home Economics 0278
Industrial 0521
Language and Literature 0279
Mathematics 0280
Music 0522
Philosophy of 0998
Physical 0523

Psychology 0525
Reading 0535
Religious 0527
Sciences 0714
Secondary 0533
Social Sciences 0534
Sociology of 0340
Special 0529
Teacher Training 0530
Technology 0710
Tests and Measurements 0288
Vocational 0747

LANGUAGE, LITERATURE AND LINGUISTICS

Language 0679
General 0289
Ancient 0290
Linguistics 0291
Modern 0291
Literature 0401
General 0294
Classical 0295
Comparative 0297
Medieval 0298
Modern 0316
African 0591
American 0305
Asian 0352
Canadian (English) 0355
Canadian (French) 0593
English 0311
Germanic 0312
Latin American 0315
Middle Eastern 0313
Romance 0314
Slavic and East European 0314

PHILOSOPHY, RELIGION AND THEOLOGY

Philosophy 0422
Religion 0318
General 0321
Biblical Studies 0319
Clergy 0320
History of 0322
Philosophy of 0469
Theology 0323

SOCIAL SCIENCES

American Studies 0323
Anthropology 0324
Archaeology 0326
Cultural 0327
Physical 0310
Business Administration 0272
General 0770
Accounting 0454
Banking 0338
Management 0385
Marketing 0501
Canadian Studies 0503
Economics 0505
General 0508
Agricultural 0509
Commerce-Business 0510
Finance 0511
History 0558
Labor 0366
Theory 0351
Folklore 0578
Geography 0366
Gerontology 0351
History 0578
General 0578

Ancient 0579
Medieval 0581
Modern 0582
Black 0328
African 0331
Asia, Australia and Oceania 0332
Canadian 0334
European 0335
Latin American 0336
Middle Eastern 0333
United States 0337
History of Science 0585
Law 0398
Political Science 0615
General 0616
International Law and Relations 0617
Public Administration 0617
Recreation 0814
Social Work 0452
Sociology 0626
General 0627
Criminology and Penology 0938
Demography 0631
Ethnic and Racial Studies 0628
Individual and Family Studies 0629
Industrial and Labor Relations 0630
Public and Social Welfare 0700
Social Structure and Development 0344
Theory and Methods 0709
Transportation 0999
Urban and Regional Planning 0453
Women's Studies 0453

THE SCIENCES AND ENGINEERING

BIOLOGICAL SCIENCES

Agriculture 0473
General 0285
Agronomy 0475
Animal Culture and Nutrition 0476
Animal Pathology 0359
Food Science and Technology 0478
Forestry and Wildlife 0479
Plant Culture 0480
Plant Pathology 0817
Plant Physiology 0777
Range Management 0746
Wood Technology 0306
Biology 0287
General 0308
Anatomy 0309
Biostatistics 0379
Botany 0329
Cell 0353
Ecology 0369
Entomology 0793
Genetics 0410
Limnology 0307
Microbiology 0317
Molecular 0416
Neuroscience 0433
Oceanography 0821
Physiology 0778
Radiation 0472
Veterinary Science 0786
Zoology 0760
Biophysics 0425
General 0996
Medical 0996

EARTH SCIENCES

Biogeochemistry 0425
Geochemistry 0996

Geodesy 0370
Geology 0372
Geophysics 0373
Hydrology 0388
Mineralogy 0411
Paleobotany 0345
Paleoecology 0426
Paleontology 0418
Paleozoology 0985
Palyology 0427
Physical Geography 0368
Physical Oceanography 0415

HEALTH AND ENVIRONMENTAL SCIENCES

Environmental Sciences 0768
Health Sciences 0566
General 0300
Audiology 0992
Chemotherapy 0567
Dentistry 0350
Education 0769
Hospital Management 0758
Human Development 0982
Immunology 0564
Medicine and Surgery 0347
Mental Health 0569
Nursing 0570
Nutrition 0380
Obstetrics and Gynecology 0354
Occupational Health and Therapy 0381
Ophthalmology 0571
Pathology 0419
Pharmacology 0572
Pharmacy 0382
Physical Therapy 0573
Public Health 0574
Radiology 0575
Recreation 0575

Speech Pathology 0460
Toxicology 0383
Home Economics 0386

PHYSICAL SCIENCES

Pure Sciences

Chemistry 0485
General 0749
Agricultural 0486
Analytical 0487
Biochemistry 0488
Inorganic 0738
Nuclear 0490
Organic 0491
Pharmaceutical 0494
Physical 0495
Polymer 0754
Radiation 0405
Mathematics 0605
Physics 0986
General 0606
Acoustics 0608
Astronomy and Astrophysics 0748
Atmospheric Science 0607
Atomic 0798
Electronics and Electricity 0759
Elementary Particles and High Energy 0609
Fluid and Plasma 0610
Molecular 0752
Nuclear 0756
Optics 0611
Radiation 0463
Solid State 0346
Statistics 0984

Applied Sciences

Applied Mechanics 0346
Computer Science 0984

Engineering 0537
General 0538
Aerospace 0539
Agricultural 0540
Automotive 0541
Biomedical 0542
Chemical 0543
Civil 0544
Electronics and Electrical 0545
Heat and Thermodynamics 0546
Hydraulic 0547
Industrial 0794
Marine 0548
Materials Science 0743
Mechanical 0551
Metallurgy 0552
Mining 0549
Nuclear 0765
Packaging 0554
Petroleum 0790
Sanitary and Municipal 0428
System Science 0796
Geotechnology 0795
Operations Research 0795
Plastics Technology 0994
Textile Technology 0994

PSYCHOLOGY

General 0621
Behavioral 0384
Clinical 0622
Developmental 0620
Experimental 0623
Industrial 0624
Personality 0625
Physiological 0989
Psychobiology 0349
Psychometrics 0632
Social 0451



ABSTRACT

A Finite Element Calculation Method for the Heat Transfer Effects on
Current-Carrying Capacity of Underground Electrical Cables

Mohamed Chaaban, Ph.D.
Concordia University, 1995

This thesis presents a combined numerical and experimental study of the heat transfer modes that take place in cavities embedded within solid bodies. The motivation is to develop a practical numerical approach to quantify the role of various regions in the global heat dissipation around underground electrical cable installations, used in electricity transmission and distribution.

A detailed numerical solution of the complex heat transfer present; conduction, free convection and radiation, with unknown boundary values at the air-solid interfaces, is first developed. For the convective flows in the cavities, the Navier-Stokes equations are solved, in stream-function vorticity form, using a Newton-Galerkin finite element approach. For the radiation part in these cavities, the shape factors of surface elements of cables and ducts are calculated by a crossed-string technique.

A series of simplifications are then made to avoid the solution of the Navier-Stokes equations. First, the cables and their surrounding backfills are discretized in one common mesh, together with the intermediate air gaps, in such a way that only the Fourier partial

differential equation is solved. To be able to do so, the air gaps are considered as fictitious solid materials with a specific thermal conductivity and a negligible thermal capacity. The individual thermal conductivity of each air gap is calculated by assuming the convection and radiation heat exchanges as separate thermal resistances acting in parallel between cables and ducts. The convection component is calculated by solving a concentric annuli problem. Results in the form of equivalent conductivity at various Rayleigh number and diameter ratios are then derived to cover the range of interest encountered in underground installations. The same approach is used to analyze the heat transfer in empty ducts by considering such ducts as populated by small fictitious unloaded cables.

The demanding resources of cable ampacity finite element conduction code are further alleviated through a new technique dubbed EFECAC (Economic Finite Element for Cable Ampacity Calculation). This technique takes advantage of the fact that the heat dissipation in cables is nearly axisymmetric and hence couples the 2D solution in the surroundings to a 1D axisymmetric grid inside the cable.

The Finite Element suite of codes thus developed are used to analyze conventional and non-conventional cable installations. These codes, equipped with an automatic mesh generator, currently enable industrial users to rapidly analyze a variety of complex underground installations.

Acknowledgments

I wish first to express my sincere thanks and appreciation to Dr. W.G. Habashi for his friendly and knowledgeable guidance throughout the course of this thesis.

I wish also to thank the Research Institute of Hydro-Québec (IREQ) for making available the opportunity to accomplish this work and for supporting my efforts throughout the various stages of this research. Special thanks to my colleagues at work for their help particularly Jean Leduc.

This thesis is dedicated to Mona and Rima.

Table of Contents

List of Figures	ix
List of Tables	xiii
Nomenclature	xiv
 1. Introduction	 1
1.1 Motivation and Objectives of the Study	1
1.2 Difficulties of the Problem	5
1.2.1 Mesh Generation	5
1.2.2 Solution of Large Size Matrices	7
1.2.3 Handling the Air Gap Between Cable and Retaining Duct	9
1.2.4 Accounting for Empty or Unloaded Ducts	10
1.3 The Proposed Approach	11
 2. Combined Radiation, Natural Convection and Conduction Heat Transfer Through Cavities Embedded in a Solid Body	 13
2.1 Modeling of the Problem	14
2.2 Justification of the Discretization Method	16
2.3 Finite Element Formulation of the Conduction-Convection Problem	18
2.3.1 Formulation in the Cavity	18
2.3.2 Formulation in the solid regions (Cables and Backfills)	26
2.4 Finite Element Formulation of the Radiation Problem	31
2.5 Applications to Empty Cavities	34

2.5.1	Simple Cavity Problems.....	34
2.5.2	Cavities Embedded in a Square Domain; a Segregated FEM Strategy	36
2.6	Cavity With Internal Heat Source: Applications to the heat transfer Between Cable and Duct.....	47
2.7	Effect of a Non-Isothermal Duct Surface on the Overall Heat Exchange	61
2.8	Empty Duct Analysis, Revisited	67
3.	A Special Finite Element for Ampacity Calculation	69
3.1	Basic Principles of the Approach.....	69
3.2	A Practical Example.....	75
4.	Industrial Applications.....	80
4.1	Cables in Troughs and in a Tunnel.....	81
4.2	Cable Inside the Air Space of a Tunnel.....	94
4.3	Aboveground Cables Exposed to the Elements	96
4.4	Cables in Duct Banks.....	98
5.	Experimental Verifications	104
5.1	Verification in Full-Size Installations	104
5.1.1	St. Lawrence River Crossing Project With 500 kV DC Cables.....	104
5.1.1.1	Prototype Test	105
5.1.1.2	Demonstration Test.....	106
5.1.2	Distribution Duct Bank	111

5.2	Verification in Laboratory Installations	118
5.2.1	1 by 3 Duct Configuration	121
5.2.1.1	Steady-State, Cables Equally Loaded	121
5.2.1.2	Steady-State, Middle Cable Unloaded	123
5.2.1.3	Transient Test, Middle Cable Unloaded	125
5.2.2	3 by 3 Duct Configuration	126
5.2.2.1	Steady-State, Cables Equally Loaded	127
5.2.2.2	Steady-State, Cables Unequally Loaded	129
5.2.3	Cables Exposed to Air.....	131
6.	Conclusions and Recommendations	134
6.1	Conclusions.....	134
6.1	Recommendations.....	136
	References.....	139

List of Figures

Figure 1.1	Typical underground duct bank installation	1
Figure 1.2	Typical underground cable construction.....	2
Figure 1.3	Cables under the floor of a tunnel (recent installation at Hydro-Québec) ...	4
Figure 1.4	Finite element mesh of the duct bank installation of figure 1.1	6
Figure 1.5	Heat flow path through an underground duct bank (Heat Flux Approach)	9
Figure 2.1	Natural convection inside cavities embedded in a solid body	14
Figure 2.2	Application of the wall boundary conditions.....	24
Figure 2.3	Crossed-string technique.....	32
Figure 2.4	Classical square cavity problem (isotherms distribution)	35
Figure 2.5	Classical square cavity problem (streamlines distribution).....	35
Figure 2.6	Cases studied: square and cylindrical empty cavities inside a square solid domain.....	37
Figure 2.7	Isotherms (°C) inside the solid domain (adiabatic cavity wall)	40
Figure 2.8	Isotherms (°C) for the whole domain, including the cavities	42
Figure 2.9	Free convection heat flux distribution along the cylindrical cavity wall ...	43
Figure 2.10	Equivalent free-convection coefficient along the cylindrical cavity wall ..	43
Figure 2.11	Temperature distribution with detailed and simplified calculations.....	46
Figure 2.12	Simulation of three-phase circuit in duct by one phase	48
Figure 2.13	Experimental sand box	51
Figure 2.14	Isotherms and streamlines distribution in annuli ($Ra = 50,000$; $Pr = 0.7$; $L/D_i = 0.8$).....	55
Figure 2.15	Local equivalent conductivity distribution ($Ra = 50,000$; $Pr = 0.7$; $L/D_i = 0.8$).....	56
Figure 2.16	Local equivalent conductivity distribution at various Rayleigh numbers ($Pr = 0.7$; $L/D_i = 0.25$).....	57

Figure 2.17	Average equivalent conductivity distribution at various Rayleigh numbers ($Pr = 0.7$; $L/D_i = 0.25$).....	57
Figure 2.18	Measured temperatures in cable/duct installation exposed to air (test 26-1).....	58
Figure 2.19	Average equivalent conductivity distribution at various L/D_i ratios.....	60
Figure 2.20	Isotherms ($^{\circ}C$) inside the cable, the air gap and the sand box	63
Figure 2.21	Comparison between measured and computed temperature distributions (detailed analysis).....	64
Figure 2.22	Convective and radiative heat flux distribution along the duct wall.....	65
Figure 2.23	Comparison between measured and computed temperatures distributions (simplified analysis).....	66
Figure 2.24	Temperatures distributions in the cylindrical empty cavity (fictitious cable approach).....	68
Figure 3.1	Link between Cartesian and polar finite element meshes	71
Figure 3.2	Example of a three-phase circuit buried in concrete slab.....	75
Figure 3.3	Finite element mesh: conventional Full-Mesh approach	76
Figure 3.4	Finite element mesh: EFECAC approach	76
Figure 3.5	Comparison between the Full-Mesh approach and the EFECAC approach (transient analysis, middle cable).....	78
Figure 3.6	EFECAC approach applied to 3D finite element mesh	79
Figure 4.1	Constant temperature boundary locations in deep tunnel installation	84
Figure 4.2	Longitudinal profile of the St. Lawrence river crossing	86
Figure 4.3	Typical cross-section of the land part of the St. Lawrence crossing.....	87
Figure 4.4	Finite element mesh of the St. Lawrence river crossing (tunnel section) ..	88
Figure 4.5	Expected air and hottest cable temperature variation inside the tunnel	89
Figure 4.6	Finite element mesh of the St. Lawrence river crossing (land part)	89
Figure 4.7	Expected hottest cable temperature variation in the land part of the crossing.....	90

Figure 4.8	Finite element mesh of a tunnel installation with one lateral water pipe cooling	91
Figure 4.9	Finite element mesh of a tunnel installation with two lateral water pipes cooling	92
Figure 4.10	Expected cable and air temperatures inside the tunnel: forced cooling	93
Figure 4.11	Expected cable and air temperatures inside the tunnel: natural cooling	93
Figure 4.12	Typical cable installation inside the air space of a tunnel.....	94
Figure 4.13	Effective solar heat flux striking the cable surface	98
Figure 4.14	Typical symmetric distribution duct bank.....	101
Figure 4.15	Typical residential daily load cycle at Hydro-Québec	101
Figure 4.16	Temperature variation following an emergency overload	103
Figure 5.1	Test loop for the prototype test	106
Figure 5.2	Prototype test: comparison between calculated and measured temperatures	107
Figure 5.3	Test loop for the demonstration test	107
Figure 5.4	Typical cross-section in the demonstration test loop	108
Figure 5.5	Finite element mesh of the trough	109
Figure 5.6	Experimental and numerical heating current levels in the demonstration test	110
Figure 5.7	demonstration test: comparison between calculated and measured temperatures	110
Figure 5.8	IREQ's experimental duct bank.....	111
Figure 5.9	Cross-section of IREQ's experimental duct bank	112
Figure 5.10	Applied daily load cycle	113
Figure 5.11	Comparison between numerical and experimental results (hottest cable, duct #14).....	115
Figure 5.12	Comparison between numerical and experimental results (coldest cable, duct #18)	115

Figure 5.13	Comparison between numerical and experimental results (Cable surface temperature in duct #9)	116
Figure 5.14	Comparison between numerical and experimental results (surface temperature of duct #3)	116
Figure 5.15	Comparison between numerical and experimental results (surface temperature of duct #20)	117
Figure 5.16	Comparison between numerical and experimental results (Side wall of the concrete backfill: thermocouple #90).....	117
Figure 5.17	Experimental laboratory mockup.....	118
Figure 5.18	Finite element mesh of the mockup (configuration 1 by 3).....	122
Figure 5.19	Comparison between numerical and experimental results (steady-state, cables equally loaded, configuration 1 by 3)	123
Figure 5.20	Comparison between numerical and experimental results (steady-state, cables unequally loaded, configuration 1 by 3).....	124
Figure 5.21	Comparison between numerical and experimental results (cyclic loading, cables equally loaded, configuration 1 by 3).....	125
Figure 5.22	Comparison between numerical and experimental results (emergency loading, cables unequally loaded, configuration 1 by 3).....	126
Figure 5.23	Finite element mesh of the mockup (configuration 3 by 3).....	127
Figure 5.24	Comparison between numerical and experimental results (steady-state, cables equally loaded, configuration 3 by 3).....	128
Figure 5.25	Comparison between numerical and experimental results (steady-state, cables unequally loaded, configuration 3 by 3).....	130
Figure 5.26	Comparison between numerical and experimental results (transient analysis, cable naked exposed to air)	132
Figure 5.27	Comparison between numerical and experimental results (transient analysis, cable in duct exposed to air).....	133

List of Tables

Table 2.1	Classical square cavity problem (comparison with other authors).....	34
Table 2.2	Calculation procedure in a cavity problem	39
Table 2.3	Experimental data: buried cable/duct installation.....	52
Table 2.4	Experimental data: cable/duct installation exposed to air.....	53
Table 2.5	Comparison between measured and analytically calculated temperatures.....	53
Table 2.6	Comparison between measured and numerically calculated values	58
Table 2.7	Configurations encountered in underground cable installations.....	60
Table 2.8	Iterative calculation procedure in cable/duct/backfill configuration	62
Table 3.1	Comparison between the conventional Full-Mesh Approach and the EFECAC technique	77
Table 4.1	Maximum nominal current distribution prior to emergency.....	102
Table 5.1	Thermal characteristics of the mockup materials	120

Nomenclature

C	thermal capacity
D	diameter
F	view factor
g	gravitational constant
h	depth
H	convection coefficient
K	thermal conductivity
L	size of the air gap in annuli
M	month of the year
MCM	cable cross-sectional area unit (1 MCM = 0.5067 mm ²)
n	normal to boundary
N	interpolation function
P	pressure
Pr	Prandtl number
q	heat flux
Q	heat loss or gain
R	thermal resistance
R	residual of a differential equation
Ra	Rayleigh number
t	time
T	temperature
U,V	velocities

Greek symbols

α	thermal diffusivity
β	volumetric expansion coefficient

ε	emissivity
γ	absorbitivity
ν	kinematic viscosity
ρ	density
σ	Stefan-Boltzmann constant ($\sigma = 5.6693 \cdot 10^{-8}$)
ω	vorticity
ψ	stream function

Subscripts

a	related to air
c	related to cable
cs	related to cable surface
cv	related to convection
d	related to duct
rd	related to radiation
s	related to solid
T	related to temperature
ω	related to vorticity
ψ	related to stream function

1. Introduction

1.1 Motivation and Objectives of the Study

In an underground cable installation, the medium and high-voltage power cables are either directly buried or laid down in PVC ducts embedded in a concrete bed and covered by various types of backfills and surrounded by native soil (figure 1.1). Often, few ducts are left empty in the installation in anticipation of future expansion.

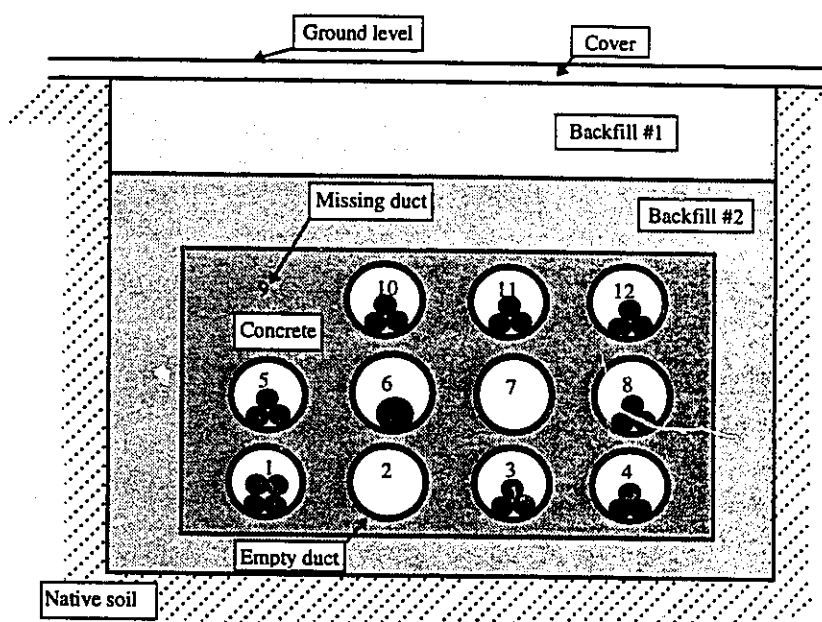


Figure 1.1 Typical underground duct bank installation

The current-carrying capacity (ampacity) of an underground cable is limited by the conductor temperature which must not exceed some norms imposed by the manufacturer in order to insure the integrity of the electric insulation material of the cable. The heat generated in the various layers of the cable, namely the conductor, the dielectric material

and the metallic sheath (figure 1.2), has to dissipate to the atmosphere; first through the air gap between the cable and the cable-retaining duct, then across the concrete bed that may include empty ducts, and finally through the various surrounding backfills and the native soil. The temperatures can be specified at the ground surface and at a certain distance away from and below the duct bank; the heat generation rate in the cable is also known. The temperature distribution inside the cables is then calculable by solving the Fourier partial differential equation using, either analytical or numerical methods.

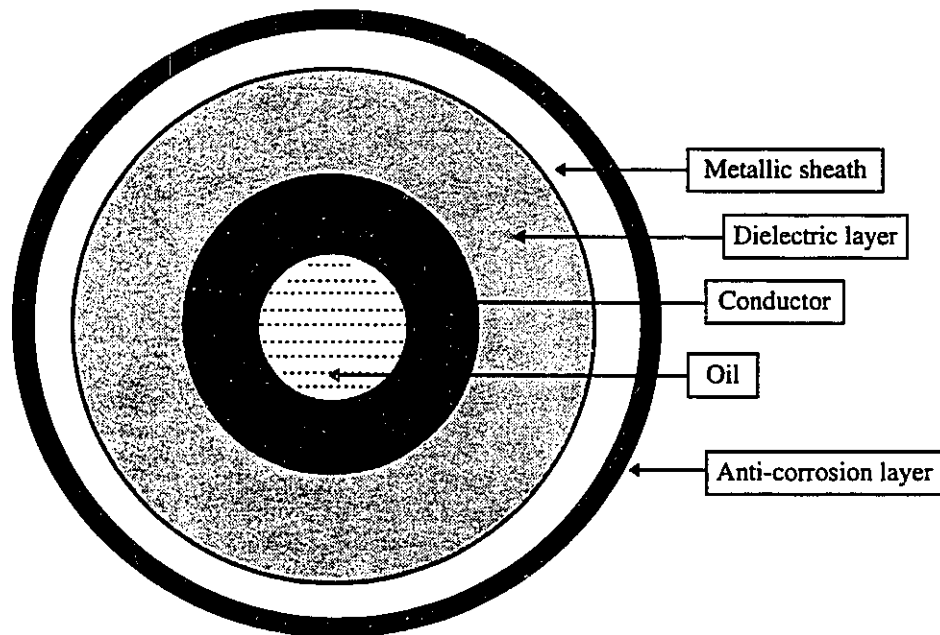


Figure 1.2 Typical underground cable construction

Due to its simplicity, the common analytical method used by electric utilities for cable ampacity calculation is the Neher-McGrath method, published in the 1950's [1]. The method employs the theory of images, first advanced by Kennelly [2], for the analysis of

the heat dissipation from a heat source in a semi-infinite medium. Some of the assumptions and limitations of the method are:

- the cable-retaining duct surface and the ground surface are considered isotherms;
- empty ducts cannot be accounted for;
- the method cannot be used for transient analysis;
- the method does not lend itself to the study of forced cooling of the cables;
- a uniform resistivity is assumed throughout the soil, independent of time or temperature;
- an estimated single-value ambient boundary condition (soil temperature) is applied.

In the case of conventional installations, where cables are installed at a depth of 1 to 2 meters in small-size isolated duct banks with few uniform backfills, such analytical methods give an acceptable accuracy. Several enhancements to the method were carried out recently to reduce some of its restrictions [3,4]. Nevertheless, they do not allow the method to be used for large size duct banks with several empty ducts, or unconventional cable installations such as duct banks crossing each other, cable and splice interfaces, cables buried in concrete troughs close to the ground surface or deep in a tunnel (figure 1.3). On the other hand, computational methods, particularly the finite element method, are well suited to analyze such complex problems. They are quite versatile and permit the consideration of practically all parameters that influence the heat flow, while requiring a minimum of simplifying assumptions. Therefore, better accuracy can be achieved, with more flexibility to analyze complex conventional and non-conventional installations.

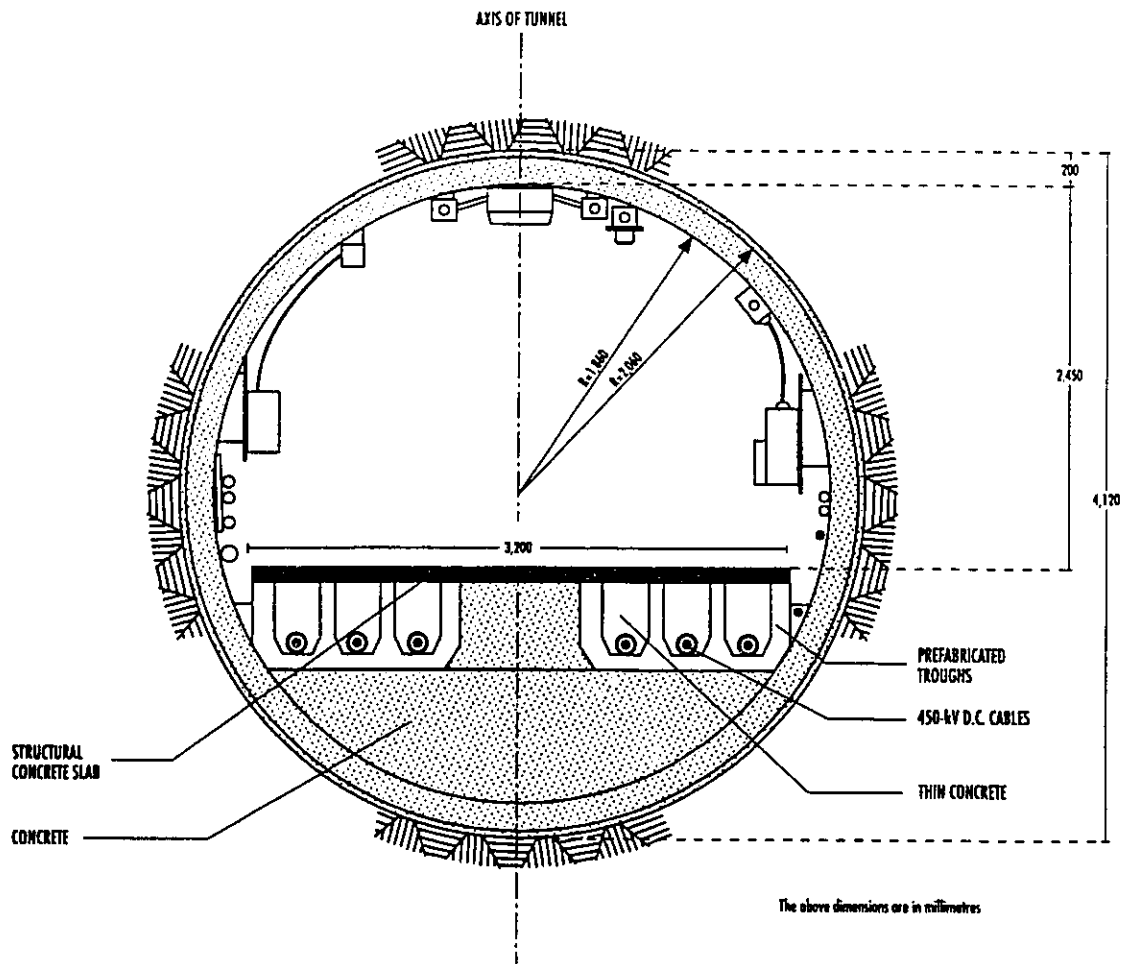


Figure 1.3 Cables under the floor of a tunnel (recent installation at Hydro-Québec)

The advantages of applying a finite element method to cable ampacity calculation can therefore be summarized as follows:

- the domain surrounding the cables can be subdivided into any number of sub-regions of different thermal properties, thus improving the accuracy of the analysis;
- forced cooling and transient analysis can be investigated with ease;
- any empty ducts can be accounted for;
- any number and type of external heat sources can be included;

- soil temperature distribution along the depth can be imposed as a variable boundary condition, depending on the season and on the geographical location of the duct bank; thus allowing the study to be carried out for year-round conditions. This feature is particularly important when conducting an emergency overload analysis because the ampacity depends on the prevailing temperature distribution, inside and around the cables, prior to the emergency;
- convective and radiative boundary conditions can be imposed on the ground surface.

1.2 Difficulties of the Problem

Several hurdles arise when applying the finite element method to the thermal analysis of underground cable installations. Some are caused by the large amount of data at the pre-processing and post-processing stages and some are related to the formulation itself. These difficulties are summarized in the following:

1.2.1 Mesh Generation

One of the major difficulties of a numerical technique is the meshing of the domain of analysis. The process consists in subdividing the various regions into triangular or quadrilateral elements and assemble the conductivity matrix and all other pertinent information required by the finite element analysis.

Several commercial codes are available to assist the user in the finite element meshing. In the field of cable ampacity calculation, the choice of commercially available mesh generation codes is not practical. Instead, it was preferable to develop a more specialized mesh generator to handle the configurations encountered in cable installations. The mesh generation program is based on mapping. Figure 1.4 shows part of the finite element mesh of the duct bank installation shown in figure 1.1.

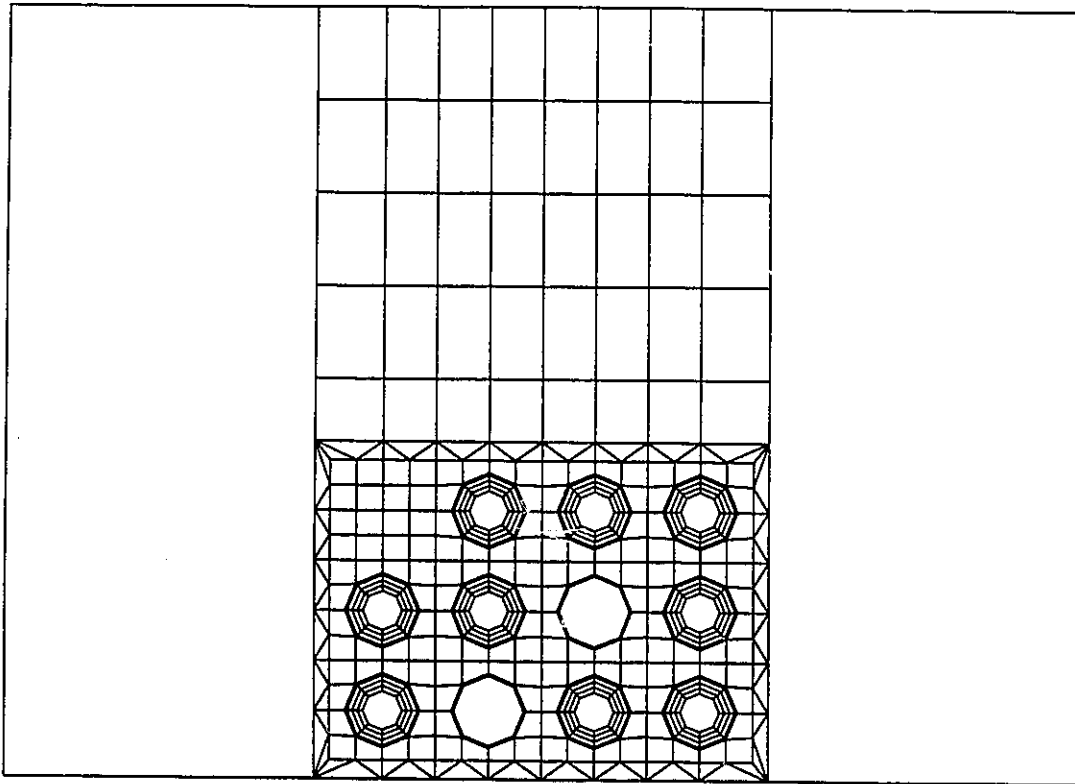


Figure 1.4 Finite element mesh of the duct bank installation of figure 1.1

1.2.2 Solution of Large Size Matrices

The accuracy of a finite element analysis improves with finer mesh density, particularly inside and around the cable where the temperature gradient is high. In some electrical installations, where several cable circuits are laid down close to each other, the size of the numerical problem can easily exceed the memory capacity of personal computers. This is caused by the large number of nodes, hence algebraic equations, that result from the meshing of the domain surrounding the cables, and, particularly, from the meshing of the cables themselves.

Usually, in conventional steady-state analysis by the "Heat Flux Approach", the meshing of the cables is not carried out. The meshing of the domain stops at the cable's or duct's outside surface, where a constant heat flux boundary condition is imposed. This flux is calculated from the heat sources generated in the various layers of the cables. Therefore, in such cases, the size of the problem remains moderate due to a relatively smaller mesh. Based on this information, and using semi-empirical equations or a numerical solution, the temperature distribution in the surrounding domain and at the surface of the duct or the cable could be calculated. Similar procedures can be used in transient analysis by updating the heat fluxes at each time step.

The drawback of these methods is that the thermal capacity of the cables cannot be accounted for. This makes short-term transient analyses (emergency overload conditions, for example) not meaningful since the thermal capacity of the cable plays an important

role in the evolution of temperature in time. In addition, having the mesh covering the regions outside the cables only, the accuracy of the analysis becomes adversely affected, since imposing a constant heat flux boundary on the outside surface of a particular cable or cable-retaining duct, automatically excludes the medium inside this cable or duct from actively participating in the evacuation of the heat generated elsewhere in the neighboring ducts. This leads to conservative results (lower current-carrying capability), especially if the backfill material around the ducts has high thermal resistivity.

Figure 1.5 illustrates schematically the heat flow path leaving the middle cable of the lower row of a typical duct bank. Similar heat flows are actually taking place simultaneously from all the other neighboring populated ducts but are not shown for clarity. The constant heat flux boundary conditions are illustrated by small arrows along the inner duct surfaces.

A more appropriate way to overcome this problem consists of extending the finite element mesh through the various layers of the cable, where the different heat sources are localized. This procedure can lead to excessively large size problems, particularly in densely populated underground installations. This approach, as well as two major simplifications, form the impetus of this Thesis.

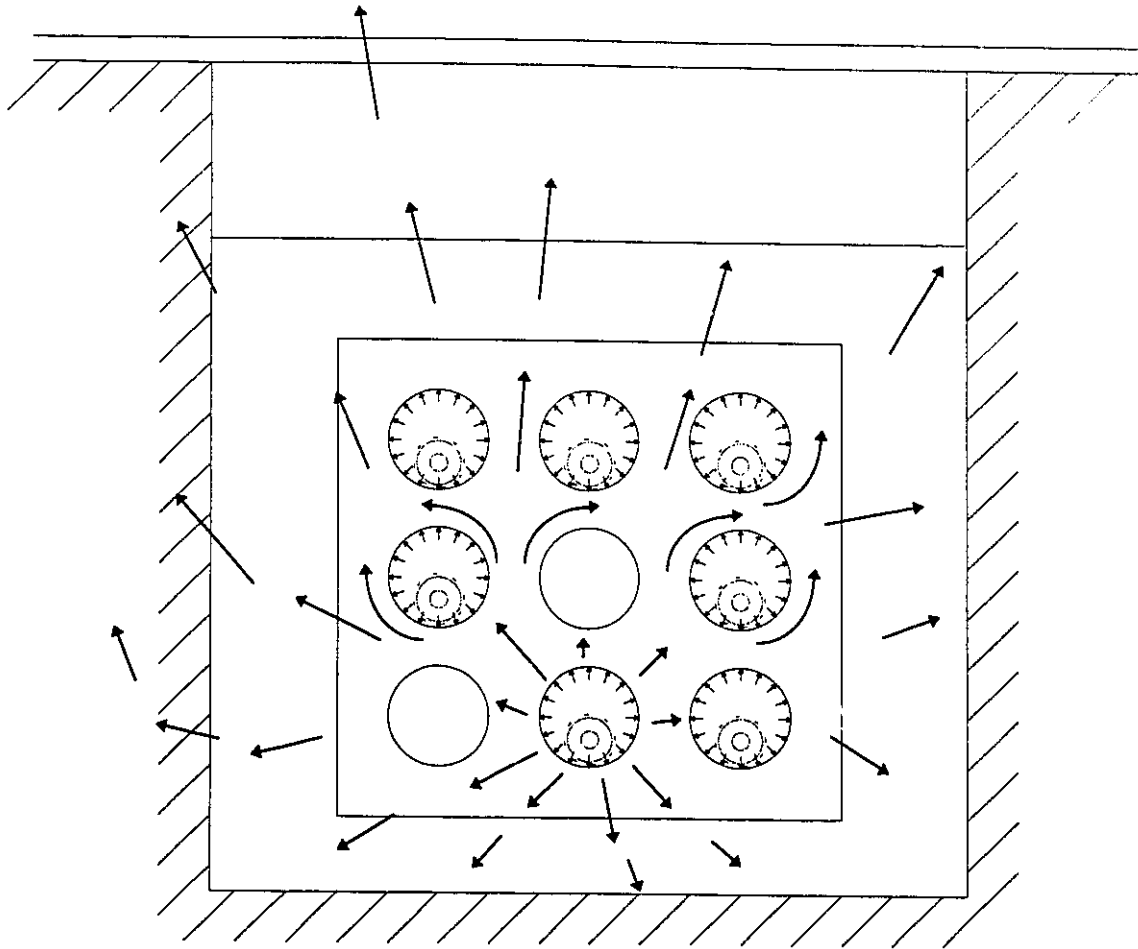


Figure 1.5 Heat flow path through an underground duct bank (Heat Flux Approach)

1.2.3 Handling the Air Gap Between Cable and Retaining Duct

In the case of a duct bank installation, the air gap between cable and duct plays an important role in the overall heat dissipation. Inside this region, conduction, free convection and radiation heat transfer take place simultaneously. In a steady-state analysis, the thermal resistance of the air gap is given by semi-empirical expressions, which will be discussed in the next chapter. The same expressions may also be used in transient analyses because the thermal capacity of the air gap is negligible.

A difficulty lies, however, in properly connecting, through the air gap, the finite element mesh outside the duct to the one inside the cable, while using the conduction equation only to solve for the temperature distribution inside the cables and elsewhere in the surroundings. The detailed numerical approach will be used to determine an equivalent thermal conductivity for the air gap, in such a way as to enable the formulation of the entire problem as one of radiation and conduction.

1.2.4 Accounting for Empty or Unloaded Ducts

The presence of empty ducts in underground duct bank installations significantly complicates the problem. The conventional Heat Flux Approach calls for the boundaries along the walls of these ducts to be considered as if they were non existent. This is equivalent, in a finite element technique, to implicitly specifying a zero heat flux along these boundaries. In other words, the medium inside the empty duct (air) is considered equivalent to a perfect thermal insulation material, certainly leading to conservative results because a relatively large portion of the domain is thus excluded from participating in the global heat dissipation.

In practice, there are many of these ducts present in underground cable installations which are intended for future expansion. A typical duct bank installation may also hold temporarily unloaded cables dedicated as emergency backup when failure occurs in some other neighboring cables. The heat losses inside these ducts are null, resulting in zero

heat fluxes along their boundaries. This means that, similarly to the case of empty ducts, the regions enclosed by the unloaded ducts are also considered as thermally insulating materials by the conventional Heat Flux Approach. The impact of an imprecise analysis of empty and unloaded ducts becomes more significant if the surrounding backfill has a high thermal resistivity.

1.3 The Proposed Approach

The main objective of this study is therefore to examine, experimentally and theoretically, the complex heat transfer phenomena inside the empty ducts and across the air gaps between cables and cable-retaining ducts, and to develop a general code that can accurately analyze complex underground installations.

A review of the literature was first performed and it was decided not to present these aspects in a separate chapter, but to introduce them in a more useful way in appropriate sections of the thesis.

In the second chapter of this study, we develop a numerical approach for the combined conduction, free convection and radiation heat transfer that take place inside empty ducts and across the air gaps between cables and ducts. We also examine simpler procedures to account for these mechanisms.

In the third chapter we propose a new approach to further reduce calculations time, based on the combination of the 2D Cartesian domain that surround the ducts, with the 1D axisymmetric domain inside cables.

The fourth chapter covers the analysis of some of the practical applications that can be adequately simulated by the proposed finite element code.

In chapter 5, we present an extensive comparison between numerical and experimental results in a variety of full-size underground installations and in a laboratory mockup.

The last chapter is dedicated to the conclusions of the present development work.

2. Combined Radiation, Natural Convection and Conduction Heat Transfer Through Cavities Embedded in a Solid Body

During the past two decades, there has been considerable research devoted to internal flow problems of enclosed natural convection. Gaseous-core nuclear reactors, double-glazed windows, solar collectors, etc., are examples of such typical applications. An overview of the numerical studies conducted in this field is well documented by de Vahl Davis and Jones [5].

Studies of natural convection in enclosures invariably include specified temperature and/or adiabatic wall boundary conditions. However, for a certain class of problems, particularly in cases where the heat source is located inside the cavity, or when empty cavities are scattered throughout a large solid conductive body (figure 2.1), it is impossible to specify these two types of boundary conditions. In reality, the boundary conditions for such cases might only be known on the external surface of the solid region, meaning that the temperature values at the fluid-solid interface in the cavity cannot be readily specified. In addition, the radiation heat transfer, coupled with conduction and convection, affects the unknown temperature boundary condition, which makes the problem even more complicated. These difficulties can be overcome by a detailed numerical approach that simultaneously accounts for conduction, free convection and radiation heat transfer inside the cavities, with the values of temperature at the air-solid interface iterated for. Only conduction heat transfer would be considered through the surrounding backfill regions.



Figure 2.1 Natural convection inside cavities embedded in a solid body

2.1 Modeling of the Problem

The governing differential equations for two-dimensional natural convection, in terms of the primitive variables, are [6]:

$$\frac{\partial U}{\partial X} + \frac{\partial V}{\partial Y} = 0 \quad (2.1)$$

$$\frac{\partial U}{\partial t} + U \frac{\partial U}{\partial X} + V \frac{\partial U}{\partial Y} = -\frac{1}{\rho} \frac{\partial P}{\partial X} + \nu \left[\frac{\partial^2 U}{\partial X^2} + \frac{\partial^2 U}{\partial Y^2} \right] \quad (2.2)$$

$$\frac{\partial V}{\partial t} + U \frac{\partial V}{\partial X} + V \frac{\partial V}{\partial Y} = -\frac{1}{\rho} \frac{\partial P}{\partial Y} + g\beta(T - T_0) + \nu \left[\frac{\partial^2 V}{\partial X^2} + \frac{\partial^2 V}{\partial Y^2} \right] \quad (2.3)$$

$$\frac{\partial T}{\partial t} + U \frac{\partial T}{\partial X} + V \frac{\partial T}{\partial Y} = \alpha \left[\frac{\partial^2 T}{\partial X^2} + \frac{\partial^2 T}{\partial Y^2} \right] \quad (2.4)$$

The governing differential equation for conduction in the solid regions is:

$$\frac{\partial T}{\partial t} = \alpha_s \left[\frac{\partial^2 T}{\partial X^2} + \frac{\partial^2 T}{\partial Y^2} \right] + \frac{S}{\rho c} \quad (2.5)$$

where

U, V are the velocities in X and Y directions

P is the pressure

T is the temperature

α, α_s is the fluid and solid thermal diffusivity, respectively

g is the gravitational constant

β is the volumetric expansion coefficient

ν is the kinematic viscosity

ρ is the density

c is the thermal capacity

S is the heat source.

The basic assumptions in the analysis are:

- the flow inside the cavity is incompressible and laminar;
- the cavity walls are gray diffuse emitters and reflectors of radiation;
- the fluid inside the cavity (air) is assumed to be radiatively non-participating;
- Fluid properties are constant except for density variation with temperature

(Boussinesq approximation)

2.2 Justification of the Discretization Method

The linearization and discretization of the governing equations can be carried out by either finite element or finite difference methods, leading to a set of algebraic equations that are repeatedly solved by direct or iterative techniques.

Although finite difference methods have been used extensively in the past to solve this type of problems, more researchers are switching to the finite element method, believing it to be better suited for the following reasons:

- more accurate representation of the geometry;
- easier application of the boundary conditions;
- flexibility in choosing the polynomial degree of approximation;
- more suitable for general purpose program development.

The 2D Navier-Stokes equations are usually solved using one of the two following formulations: the primitive variables (U, V, P, T) or the stream function-vorticity formulations (ψ, ω, T). The latter has the advantage of exactly satisfying the mass conservation and reducing the number of equations by one (from 4 to 3), by eliminating the pressure. The classical difficulty in using the stream function-vorticity formulation is that the no-penetration and the no-slip condition yield two boundary conditions on the stream function, while the vorticity has no explicit boundary condition. This difficulty has

traditionally been overcome with limited success by iteratively defining boundary vorticity from the normal gradient of the stream function, through a Taylor expansion [7]. The procedure fails at reasonably low Reynolds or Rayleigh numbers. Major breakthroughs in this formulation [8, 9, 10,11] have come first from the recognition that solving the stream function and vorticity transport equations, simultaneously, permits an easy non-iterative and more mathematically appropriate imposition of the two boundary conditions. Furthermore, by taking advantage of the natural boundary conditions of a finite element formulation, it has been shown that it is possible to impose the no-slip condition in an exact way, rather than through a Taylor expansion. Taken together, these two ideas can lead to formulations that, even at high Reynolds or Rayleigh numbers, do not require any artificial viscosity to stabilize. In fact, in [12] the method has been further extended to compressible and turbulent flows. The stream function-vorticity approach will therefore be adopted here due to its many innate advantages.

2.3 Finite Element Formulation of the Conduction-Convection Problem

In this development, the analysis of the free convection part is restricted to steady state only since the thermal capacity of the air gap between cable and duct and of the air inside an empty duct is negligible. However, the conduction part inside the cables and the surrounding backfills covers both steady state and transient regimes.

2.3.1 Formulation in the cavity

First, the momentum equations (2.2) and (2.3) are transformed to the stream function and vorticity form by a cross-differentiation in order to eliminate the pressure term. The resulting equations for steady-state flow are the energy equation, the vorticity transport equation and the definition of vorticity (in terms of stream function):

$$\frac{\partial \psi}{\partial Y} \frac{\partial T}{\partial X} - \frac{\partial \psi}{\partial X} \frac{\partial T}{\partial Y} = \alpha \left[\frac{\partial^2 T}{\partial X^2} + \frac{\partial^2 T}{\partial Y^2} \right] \quad (2.6)$$

$$\frac{\partial \psi}{\partial Y} \frac{\partial \omega}{\partial X} - \frac{\partial \psi}{\partial X} \frac{\partial \omega}{\partial Y} = g\beta \frac{\partial T}{\partial X} + \nu \left[\frac{\partial^2 \omega}{\partial X^2} + \frac{\partial^2 \omega}{\partial Y^2} \right] \quad (2.7)$$

$$\frac{\partial^2 \psi}{\partial X^2} + \frac{\partial^2 \psi}{\partial Y^2} = -\omega \quad (2.8)$$

where

- ω is the vorticity
- ψ is the stream function
- T is the temperature

- α is the fluid thermal diffusivity
 g is the gravitational constant
 β is the volumetric expansion coefficient
 ν is the kinematic viscosity

The boundary conditions along the solid-fluid interface are:

$$-K_s \left[\frac{\partial T}{\partial n} \right] = -K_a \frac{\partial T}{\partial n} + q_r \quad (2.9)$$

where q_r is the net heat flux due to multiple reflection and absorption of radiation heat transfer. K_a is the fluid (air) thermal conductivity and n is the normal direction at the solid-fluid interface.

The no-slip and the no-penetration conditions are expressed by, respectively :

$$\frac{\partial \psi}{\partial n} = 0 \quad (2.10)$$

$$\psi = 0 \quad (2.11)$$

A quadrilateral 8-noded element is used in the present development with a quadratic interpolation for all variables involved.

$$\langle T \psi \omega \rangle = \langle N_1 N_2 \dots N_8 \rangle \begin{bmatrix} T_1 & \psi_1 & \omega_1 \\ T_2 & \psi_2 & \omega_2 \\ \dots & \dots & \dots \\ T_8 & \psi_8 & \omega_8 \end{bmatrix} \quad (2.12)$$

Multiplying equations (2.6) to (2.8) by the interpolation function $\langle N \rangle$ and integrating by parts, following the standard finite element discretization:

$$-\alpha [K] \{T\} - \{a(\psi, T)\} + \alpha \{b(T_n)\} = 0 \quad (2.13)$$

$$-\nu [K] \{\omega\} - \{a(\psi, \omega)\} + \nu \{b(\omega_n)\} + g\beta [C] \{T\} = 0 \quad (2.14)$$

$$-[K] \{\psi\} + [M] \{\omega\} + \{b(\psi_n)\} = 0 \quad (2.15)$$

where:

$$[K]_{8 \times 8} = \iint \begin{bmatrix} \frac{\partial N_1}{\partial X} & \dots & \frac{\partial N_1}{\partial Y} \\ \dots & \dots & \dots \\ \frac{\partial N_8}{\partial X} & \dots & \frac{\partial N_8}{\partial Y} \end{bmatrix} \begin{bmatrix} \frac{\partial N_1}{\partial X} & \dots & \frac{\partial N_1}{\partial Y} \\ \dots & \dots & \dots \\ \frac{\partial N_8}{\partial X} & \dots & \frac{\partial N_8}{\partial Y} \end{bmatrix} dX dY \quad (2.16)$$

$$[C]_{8 \times 8} = \iint \begin{Bmatrix} N_1 \\ \dots \\ N_8 \end{Bmatrix} \left\langle \frac{\partial N_1}{\partial X} \quad \dots \quad \frac{\partial N_8}{\partial X} \right\rangle dX dY \quad (2.17)$$

$$[M]_{8 \times 8} = \iint \begin{Bmatrix} N_1 \\ \dots \\ N_8 \end{Bmatrix} \langle N_1 \quad \dots \quad N_8 \rangle dX dY \quad (2.18)$$

$$\begin{aligned}
\{a(\psi, T)\}_{8X1} &= \iint \left\{ \begin{matrix} N_1 \\ \dots \\ N_8 \end{matrix} \right\} \left\langle \frac{\partial N_1}{\partial Y} \dots \frac{\partial N_8}{\partial Y} \right\rangle \left\{ \begin{matrix} \psi_1 \\ \dots \\ \psi_8 \end{matrix} \right\} \left\langle \frac{\partial N_1}{\partial X} \dots \frac{\partial N_8}{\partial X} \right\rangle \left\{ \begin{matrix} T_1 \\ \dots \\ T_8 \end{matrix} \right\} dX dY - \\
&\iint \left\{ \begin{matrix} N_1 \\ \dots \\ N_8 \end{matrix} \right\} \left\langle \frac{\partial N_1}{\partial X} \dots \frac{\partial N_8}{\partial X} \right\rangle \left\{ \begin{matrix} \psi_1 \\ \dots \\ \psi_8 \end{matrix} \right\} \left\langle \frac{\partial N_1}{\partial Y} \dots \frac{\partial N_8}{\partial Y} \right\rangle \left\{ \begin{matrix} T_1 \\ \dots \\ T_8 \end{matrix} \right\} dX dY \quad (2.19)
\end{aligned}$$

$$\begin{aligned}
\{a(\psi, \omega)\}_{8X1} &= \iint \left\{ \begin{matrix} N_1 \\ \dots \\ N_8 \end{matrix} \right\} \left\langle \frac{\partial N_1}{\partial Y} \dots \frac{\partial N_8}{\partial Y} \right\rangle \left\{ \begin{matrix} \psi_1 \\ \dots \\ \psi_8 \end{matrix} \right\} \left\langle \frac{\partial N_1}{\partial X} \dots \frac{\partial N_8}{\partial X} \right\rangle \left\{ \begin{matrix} \omega_1 \\ \dots \\ \omega_8 \end{matrix} \right\} dX dY - \\
&\iint \left\{ \begin{matrix} N_1 \\ \dots \\ N_8 \end{matrix} \right\} \left\langle \frac{\partial N_1}{\partial X} \dots \frac{\partial N_8}{\partial X} \right\rangle \left\{ \begin{matrix} \psi_1 \\ \dots \\ \psi_8 \end{matrix} \right\} \left\langle \frac{\partial N_1}{\partial Y} \dots \frac{\partial N_8}{\partial Y} \right\rangle \left\{ \begin{matrix} \omega_1 \\ \dots \\ \omega_8 \end{matrix} \right\} dX dY \quad (2.20)
\end{aligned}$$

$$\{b(T_n)\}_{8X1} = \iint \left\{ \begin{matrix} N_1 \\ \dots \\ N_8 \end{matrix} \right\} \frac{\partial T}{\partial n} ds \quad (2.21)$$

where

$$\frac{\partial T}{\partial n} ds = \frac{\partial T}{\partial Y} dX + \frac{\partial T}{\partial X} dY \quad (2.22)$$

$$\{b(\omega_n)\}_{8X1} = \iint \left\{ \begin{matrix} N_1 \\ \dots \\ N_8 \end{matrix} \right\} \frac{\partial \omega}{\partial n} ds \quad (2.23)$$

$$\{b(\psi_n)\}_{8X1} = \iint \left\{ \begin{matrix} N_1 \\ \dots \\ N_8 \end{matrix} \right\} \frac{\partial \psi}{\partial n} ds \quad (2.24)$$

Initially, these equations were solved in a segregated way [13] for T , ψ and ω and using the right-hand-sides computed from the last previously determined values. This approach was found to work only for low Rayleigh numbers, and only with heavy under-relaxation coefficient (0.1, 0.2).

In order to eliminate this difficulty, we use a Newton algorithm to speed convergence.

For a given solution T , ψ and ω , assume:

$$T^{n+1} = T^n + \Delta T \quad (2.25)$$

$$\omega^{n+1} = \omega^n + \Delta \omega \quad (2.26)$$

$$\psi^{n+1} = \psi^n + \Delta \psi \quad (2.27)$$

After substituting into (2.13) to (2.15) and neglecting second order terms, we have:

$$[J]\{\Delta U\} = -\{R_U\} \quad (2.28)$$

where U represents the variables T , ω or ψ , and R is the corresponding residual vectors.

The Jacobian is: $J_{ij} = \frac{\partial R_i}{\partial U_j} \quad (2.29)$

Following the standard procedure, we obtain the following system of equations:

$$\begin{bmatrix} [J_T] \\ [J_\omega] \\ [J_\psi] \end{bmatrix} \begin{Bmatrix} \{\Delta T\} \\ \{\Delta \omega\} \\ \{\Delta \psi\} \end{Bmatrix} = - \begin{Bmatrix} \{R_T\} \\ \{R_\omega\} \\ \{R_\psi\} \end{Bmatrix} \quad (2.30)$$

where

$$[J_T]_{8 \times 24} = \begin{bmatrix} [\alpha K_{ij} + A_{ij}(\psi)] & [0] & [-A_{ij}(T)] \end{bmatrix} \quad (2.31)$$

$$[J_\omega]_{8 \times 24} = \begin{bmatrix} [-g\beta C_{ij}] & [vK_{ij} + A_{ij}(\psi)] & [-A_{ij}(\omega)] \end{bmatrix} \quad (2.32)$$

$$[J_\psi]_{8 \times 24} = \begin{bmatrix} [0] & [-M_{ij}] & [K_{ij}] \end{bmatrix} \quad (2.33)$$

$$A_{ij}(T) = \iint N_i \left(\left\langle \frac{\partial N_1}{\partial Y} \quad \dots \quad \frac{\partial N_8}{\partial Y} \right\rangle \begin{Bmatrix} T_1 \\ \dots \\ T_8 \end{Bmatrix} \frac{\partial N_j}{\partial X} - \left\langle \frac{\partial N_1}{\partial X} \quad \dots \quad \frac{\partial N_8}{\partial X} \right\rangle \begin{Bmatrix} T_1 \\ \dots \\ T_8 \end{Bmatrix} \frac{\partial N_j}{\partial Y} \right) dX dY \quad (2.34)$$

$$A_{ij}(\omega) = \iint N_i \left(\left\langle \frac{\partial N_1}{\partial Y} \quad \dots \quad \frac{\partial N_8}{\partial Y} \right\rangle \begin{Bmatrix} \omega_1 \\ \dots \\ \omega_8 \end{Bmatrix} \frac{\partial N_j}{\partial X} - \left\langle \frac{\partial N_1}{\partial X} \quad \dots \quad \frac{\partial N_8}{\partial X} \right\rangle \begin{Bmatrix} \omega_1 \\ \dots \\ \omega_8 \end{Bmatrix} \frac{\partial N_j}{\partial Y} \right) dX dY \quad (2.35)$$

$$A_{ij}(\psi) = \iint N_i \left(\left\langle \frac{\partial N_1}{\partial Y} \quad \dots \quad \frac{\partial N_8}{\partial Y} \right\rangle \begin{Bmatrix} \psi_1 \\ \dots \\ \psi_8 \end{Bmatrix} \frac{\partial N_j}{\partial X} - \left\langle \frac{\partial N_1}{\partial X} \quad \dots \quad \frac{\partial N_8}{\partial X} \right\rangle \begin{Bmatrix} \psi_1 \\ \dots \\ \psi_8 \end{Bmatrix} \frac{\partial N_j}{\partial Y} \right) dX dY \quad (2.36)$$

The terms K_{ij} , C_{ij} and M_{ij} are defined in equations (2.16) to (2.18).

Let us now illustrate the application of the no-slip and the no-penetration b.c.'s through an example (figure 2.2). Suppose that nodes 5, 6 and 7 of the 8-noded element fall on the solid boundary as shown in the sketch below. At these nodes we have 2 b.c.'s for ψ and none for ω .

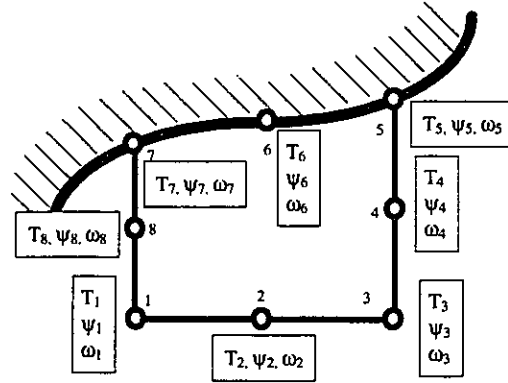


Figure 2.2 Application of the wall boundary conditions

Let us use the no-slip $\frac{\partial \psi}{\partial n} = 0$ to define the boundary condition for the stream function and the no-penetration boundary condition for vorticity, as follows:

For simplicity, let us illustrate the introduction of boundary condition at node #6 only. At this node, the residual vector for ω is not assembled and, instead, the no-penetration condition, $\psi = \psi_0 = \text{constant}$, is forced on node #6 by equating the corresponding diagonal term of ψ to 1 and the remaining terms in the same row to zero.

For the no-slip condition, the last term in equation (2.15), resulting from contour integral, is neglected, hence implicitly satisfying $\frac{\partial \psi}{\partial n} = 0$.

$$-R_\psi = [K]\{\psi\} - [M]\{\omega\} \quad (2.37)$$

The element influence matrix therefore becomes, after the application of the boundary condition at node #6:

$$\begin{bmatrix}
 \begin{bmatrix} \dots & \dots & \dots & \dots \\ \dots & \dots & \dots & \dots \\ \dots & \dots & \dots & \dots \\ \dots & \dots & \dots & \dots \end{bmatrix} &
 \begin{bmatrix} \dots & \dots & \dots & \dots \\ \dots & \dots & \dots & \dots \\ \dots & \dots & \dots & \dots \\ \dots & \dots & \dots & \dots \end{bmatrix} &
 \begin{bmatrix} \dots & \dots & \dots & \dots \\ \dots & \dots & \dots & \dots \\ \dots & \dots & \dots & \dots \\ \dots & \dots & \dots & \dots \end{bmatrix} \\
 \begin{bmatrix} \dots & \dots & \dots & \dots \\ \dots & \dots & \dots & \dots \\ 0 & 0 & 0 & 0 \\ \dots & \dots & \dots & \dots \end{bmatrix} &
 \begin{bmatrix} \dots & \dots & \dots & \dots \\ \dots & \dots & \dots & \dots \\ 0 & 0 & 0 & 0 \\ \dots & \dots & \dots & \dots \end{bmatrix} &
 \begin{bmatrix} \dots & \dots & \dots & \dots \\ \dots & \dots & \dots & \dots \\ 0 & 0 & 1 & 0 \\ \dots & \dots & \dots & \dots \end{bmatrix} \\
 \begin{bmatrix} \dots & \dots & \dots & \dots \\ \dots & \dots & \dots & \dots \\ 0 & 0 & 0 & 0 \\ \dots & \dots & \dots & \dots \end{bmatrix} &
 \begin{bmatrix} \dots & \dots & \dots & \dots \\ \dots & \dots & \dots & \dots \\ 0 & 0 & [M] & 0 \\ \dots & \dots & \dots & \dots \end{bmatrix} &
 \begin{bmatrix} \dots & \dots & \dots & \dots \\ \dots & \dots & \dots & \dots \\ 0 & 0 & [-K] & 0 \\ \dots & \dots & \dots & \dots \end{bmatrix}
 \end{bmatrix}
 \begin{Bmatrix}
 \begin{Bmatrix} \Delta T_1 \\ \dots \\ \dots \\ \dots \end{Bmatrix} \\
 \begin{Bmatrix} \Delta \omega_1 \\ \dots \\ \Delta \omega_6 \\ \dots \end{Bmatrix} \\
 \begin{Bmatrix} \dots \\ \dots \\ \Delta \psi_6 \\ \dots \end{Bmatrix}
 \end{Bmatrix}
 =
 \begin{Bmatrix}
 \begin{Bmatrix} -R_{T1} \\ \dots \\ \dots \\ \dots \end{Bmatrix} \\
 \begin{Bmatrix} -R_{\omega 1} \\ \dots \\ 0 \\ \dots \end{Bmatrix} \\
 \begin{Bmatrix} \dots \\ \dots \\ R_{\psi_6} \\ \dots \end{Bmatrix}
 \end{Bmatrix}
 \quad (2.38)$$

2.3.2 Formulation in the Solid Regions (Cables and Backfills)

The governing differential equation of the heat conduction inside an isotropic solid body is:

$$\frac{\partial T}{\partial t} = \alpha_s \left[\frac{\partial^2 T}{\partial X^2} + \frac{\partial^2 T}{\partial Y^2} \right] + \frac{S}{\rho c} \quad (2.39)$$

The boundary conditions are:

a) at the open boundaries:

$$-k_s \frac{\partial T}{\partial n} = h_c (T - T_{\infty c}) + h_r (T - T_{\infty r}) - Q \quad (2.40)$$

$$h_r = \sigma \epsilon (T + T_{\infty r}) (T^2 + T_{\infty r}^2) \quad (2.41)$$

where h_r is the linearized radiation heat transfer coefficient, h_c is the convection coefficient and Q is the heat flux, σ is the Stefan-Boltzmann constant ($\sigma = 5.6693 \times 10^{-8}$).

b) at the closed boundary of the cavity

$$-k_s \frac{\partial T}{\partial n} = -k_a \frac{\partial T}{\partial n} + q_r = -k_a \frac{\partial T}{\partial n} + (\sigma \epsilon T^4 - \gamma q_{r_i}) \quad (2.42)$$

where q_r is the net radiation, q_{ri} is the incident radiation, γ is the absorbtivity of the surface ($\gamma = \epsilon$, gray body assumption).

The heat flux resulting from the free convection inside the cavity $k_a \frac{\partial T}{\partial n}$ is dealt with in the previous section. This heat flux can also be combined iteratively to the open boundary fluxes if there are any. Therefore, for any boundary condition (open or closed) one can write:

$$-k_s \frac{\partial T}{\partial n} = h_c(T - T_{\infty c}) + h_r(T - T_{\infty r}) - q + (\sigma \epsilon T^4 - \gamma q_{ri}) \quad (2.43)$$

where (q) is a combination of the heat fluxes acting on the open boundary (Q) and the heat flux resulting from the free convection inside the cavity $(k_a \frac{\partial T}{\partial n})$.

Equation (2.43) is highly nonlinear. The term $\sigma \epsilon T^4$ is linearized by replacing T^4 by $T_m^3 T$, where T_m is the average temperature of the boundary segment and T is the absolute temperature in K.

The finite element discretization of equation (2.39) yields [14]:

$$[C]\{\dot{T}\} + [K]\{T\} = \{RHS\} \quad (2.44)$$

where

$$[K] = [K_c] + [K_{cv}] + [K_r] + [K_{rc}] \quad (2.45)$$

$$[RHS] = [RHS_s] + [RHS_q] + [RHS_{cv}] + [RHS_r] + [RHS_{rc}] - [RHS_{const}] \quad (2.46)$$

$$[C] = \iint \rho c \begin{Bmatrix} N_1 \\ \vdots \\ N_n \end{Bmatrix} \langle N_1 \quad \dots \quad N_n \rangle dX dY \quad (2.47)$$

is the capacity matrix

$$[K_c] = \iiint_{\epsilon} [B]^T [k] [B] dX dY \quad (2.48)$$

is the element conductivity submatrix

$$[K_{cv}] = \iint h_c \begin{Bmatrix} N_1 \\ \vdots \\ N_n \end{Bmatrix} \langle N_1 \quad \dots \quad N_n \rangle ds \quad (2.49)$$

is the convection submatrix

$$[K_r] = \iint h_r \begin{Bmatrix} N_1 \\ \vdots \\ N_n \end{Bmatrix} \langle N_1 \quad \dots \quad N_n \rangle ds \quad (2.50)$$

is the open boundary radiation submatrix

$$[K_{rc}] = \iint \sigma \epsilon T_m^3 \begin{Bmatrix} N_1 \\ \vdots \\ N_n \end{Bmatrix} \langle N_1 \quad \dots \quad N_n \rangle ds \quad (2.51)$$

is the closed boundary radiation submatrix,

The corresponding right hand side vectors are:

$$\{RHS_s\} = \iint S\{N\}dXdY \quad (2.52)$$

$$\{RHS_q\} = \int q\{N\}ds \quad (2.53)$$

$$\{RHS_{cv}\} = \int h_{cv}T_{\infty c}\{N\}ds \quad (2.54)$$

$$\{RHS_r\} = \int h_rT_{\infty r}\{N\}ds \quad (2.55)$$

$$\{RHS_{rc}\} = \int \alpha q_r\{N\}ds \quad (2.56)$$

$$\{RHS_{const}\} = \int \sigma \epsilon T_m^3\{N\}\langle N \rangle \begin{Bmatrix} 273 \\ .. \\ 273 \end{Bmatrix} ds \quad (2.57)$$

$$[B] = \begin{bmatrix} \frac{\partial N_1}{\partial X} & \cdots & \frac{\partial N_n}{\partial X} \\ \frac{\partial N_1}{\partial Y} & \cdots & \frac{\partial N_n}{\partial Y} \end{bmatrix} \quad (2.58)$$

The linearized radiation coefficient is given by:

$$h_r = \sigma \epsilon (T_m^2 + T_{\infty r}^2)(T_m + T_{\infty r}) \quad (2.59)$$

Using the forward Euler or fully implicit method to discretize the transient term in equation (2.44), we obtain:

$$\left[\frac{1}{\Delta t} [C] + [K] \right] \{T\}_{n+1} = \frac{1}{\Delta t} [C] \{T\}_n + \{RHS\}_{n+1} \quad (2.60)$$

where n is the iteration number.

The initial conditions for the transient analysis of an underground installation are specified as the temperature field that prevails inside and around the cables prior to this particular analysis (examples of an emergency test or the first time loading of an installation). This temperature distribution is normally calculated by conducting a steady state analysis with the prescribed load pattern. The spatial boundary conditions are a mixture of convection, radiation, heat flux and constant temperature boundaries. The locations of these boundaries depend mainly on the type of installation and are explained in details in chapter 4.

2.4 Finite Element Formulation of the Radiation Problem

The heat exchange by radiation inside a cavity consists in deriving a radiation heat balance equation for each individual segment of the wall and an overall heat balance within the enclosure.

The cavity wall is subdivided into (n) segments. Each segment interacts with all the others according to the view factors, to the surfaces emissivity and reflectivity and to the prevailing local temperature. The view factors of each surface element (example of cable and duct) are calculated using the crossed-string technique [15]. This method can precisely calculate these shape factors in an enclosure and cope with any number and shape of blockages encountered (figure 2.3). The radiation heat fluxes striking each element, resulting from multi-reflection and absorption, are calculated as follows:

The incident radiation q_{ri} on segment (i) is equal to the sum of the fraction of energy emitted and reflected by surfaces (j) which fall on surface (i).

$$q_{ri} = \sum_{j=1}^n \frac{F_{ij} A_j}{A_i} B_j \quad (2.61)$$

where B_j is the radiosity, i.e. the rate of the heat flow per unit area leaving surface (j) which is the total of the emitted and reflected energy.

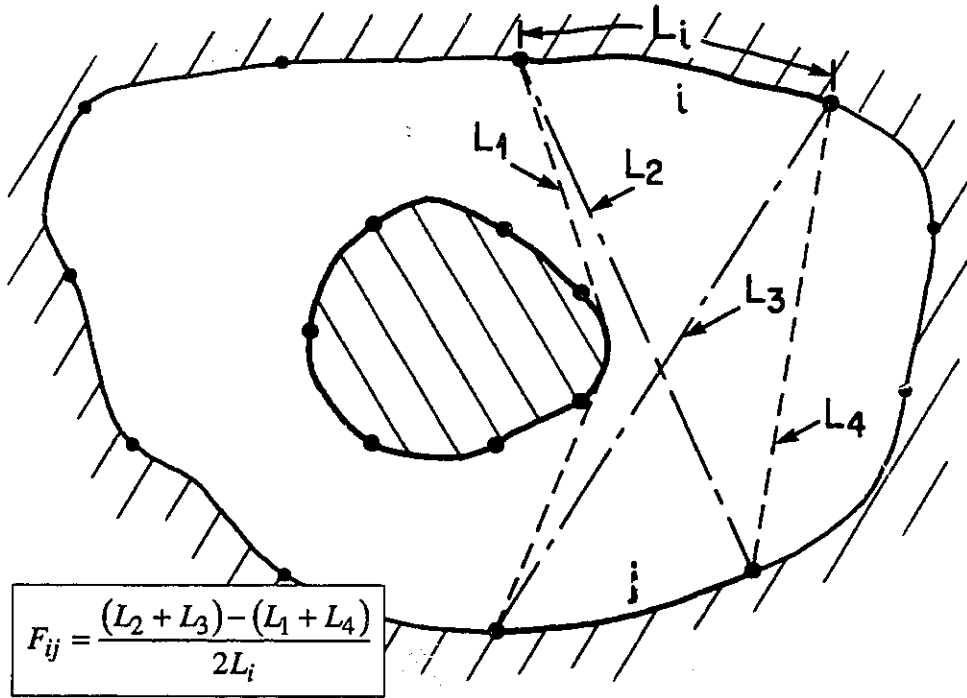


Figure 2.3 Crossed-string technique

$$B_j = \epsilon_j \sigma T_j^4 + \rho_j q_{rj} \quad (2.62)$$

We know that $F_{ij} A_i = F_{ji} A_j$ (2.63)

Substituting into equation (2.61) yields:

$$q_{ri} = F_{i1} B_1 + F_{i2} B_2 + \dots + F_{in} B_n \quad (2.64)$$

Substituting B_j by its value and rearranging:

$$q_{ri} = F_{i2} (\epsilon \sigma T_2^4 + \rho q_{r2}) + F_{i3} (\epsilon \sigma T_3^4 + \rho q_{r3}) + \dots + F_{in} (\epsilon \sigma T_n^4 + \rho q_{rn}) \quad (2.65)$$

In matrix form:

$$\begin{bmatrix} (1-F_{11}\rho_1) & (-F_{12}\rho_2) & \dots & (-F_{1j}\rho_j) \\ (-F_{21}\rho_1) & (1-F_{22}\rho_2) & \dots & (-F_{2j}\rho_j) \\ \ddots & \ddots & \ddots & \ddots \\ (-F_{i1}\rho_1) & (-F_{i2}\rho_2) & \dots & (1-F_{ij}\rho_j) \end{bmatrix} \begin{bmatrix} q_{r1} \\ q_{r2} \\ \ddots \\ q_{ri} \end{bmatrix} = \begin{bmatrix} F_{11}\epsilon_1\sigma T_1^4 + \dots + F_{1j}\epsilon_j\sigma T_j^4 \\ F_{21}\epsilon_1\sigma T_1^4 + \dots + F_{2j}\epsilon_j\sigma T_j^4 \\ \ddots \\ F_{i1}\epsilon_1\sigma T_1^4 + \dots + F_{ij}\epsilon_j\sigma T_j^4 \end{bmatrix} \quad (2.66)$$

The solution to this system of equations provides the distribution of the incident radiation that can be imposed as a constant heat flux boundary condition along the cavity wall.

Another alternative has been proved to have a faster convergence rate consists of calculating a fictitious ambient temperature T_∞ for each segment in the cavity in terms of the incident radiation as follows:

$$\sigma\epsilon_i(T_i^4 - T_{\infty i}^4) = \sigma\epsilon_i T_i^4 - \gamma_i q_{ri} \quad (2.67)$$

i.e.

$$T_{\infty i} = \left(\frac{q_{ri}}{\sigma} \right)^{0.25} \quad (2.68)$$

Hence, the closed boundary radiation can be treated as an open boundary radiation with the bulk temperature defined by equation (2.68).

2.5 Applications to Empty Cavities

2.5.1 Simple Cavity Problems

The finite element code that solves equations (2.6) to (2.11) was first put to test in the classical square-cavity problem, where the vertical walls are maintained at a non-dimensional constant temperature of 0 and 1, while the horizontal walls are perfectly insulated (adiabatic). The cavity was divided into 18x18 non-uniform divisions. A quadrilateral eight-noded element was used with a quadratic interpolation for all variables involved. The results, in terms of the maximum, minimum and center values of stream function, vorticity and temperature, agree well with published results [5] as outlined in table 2.1. The analysis was pursued to a Rayleigh number as high as 7.7×10^7 . The resulting isotherms and streamlines distributions in this case are shown in figures 2.4 and 2.5, respectively.

Pr = 0.71	Ra = 10^4	Ra = 10^5	Ra = 10^6	Ra = 10^7	Ra = $7.7 \cdot 10^7$
present results (str. - vort.)	$\Psi_{\max} = 5.092$ $\Psi_{\min} = 0.000$ $\Psi_c = 5.092$	$\Psi_{\max} = 9.611$ $\Psi_{\min} = 0.000$ $\Psi_c = 9.137$	$\Psi_{\max} = 16.838$ $\Psi_{\min} = 0.000$ $\Psi_c = 16.452$	$\Psi_{\max} = 30.469$ $\Psi_{\min} = -0.020$ $\Psi_c = 29.535$	$\Psi_{\max} = 51.476$ $\Psi_{\min} = -3.356$ $\Psi_c = 49.797$
Stevens (str. - vort.)	$\Psi_{\max} = \text{-----}$ $\Psi_c = 3.090$	$\Psi_{\max} = 9.640$ $\Psi_c = 9.100$	$\Psi_{\max} = 16.900$ $\Psi_c = 16.400$	$\Psi_{\max} = 30.300$ $\Psi_c = 29.300$	
Gartling (prim. - var.)	$\Psi_{\max} = \text{-----}$ $\Psi_c = 5.074$	$\Psi_{\max} = 9.603$ $\Psi_c = \text{-----}$	$\Psi_{\max} = 16.851$ $\Psi_c = \text{-----}$		
Winter (prim. - var.)	$\Psi_{\max} = \text{-----}$ $\Psi_c = 5.075$	$\Psi_{\max} = 9.638$ $\Psi_c = 9.117$	$\Psi_{\max} = 16.800$ $\Psi_c = 16.430$		

Table 2.1 Classical square cavity problem (comparison with other authors)

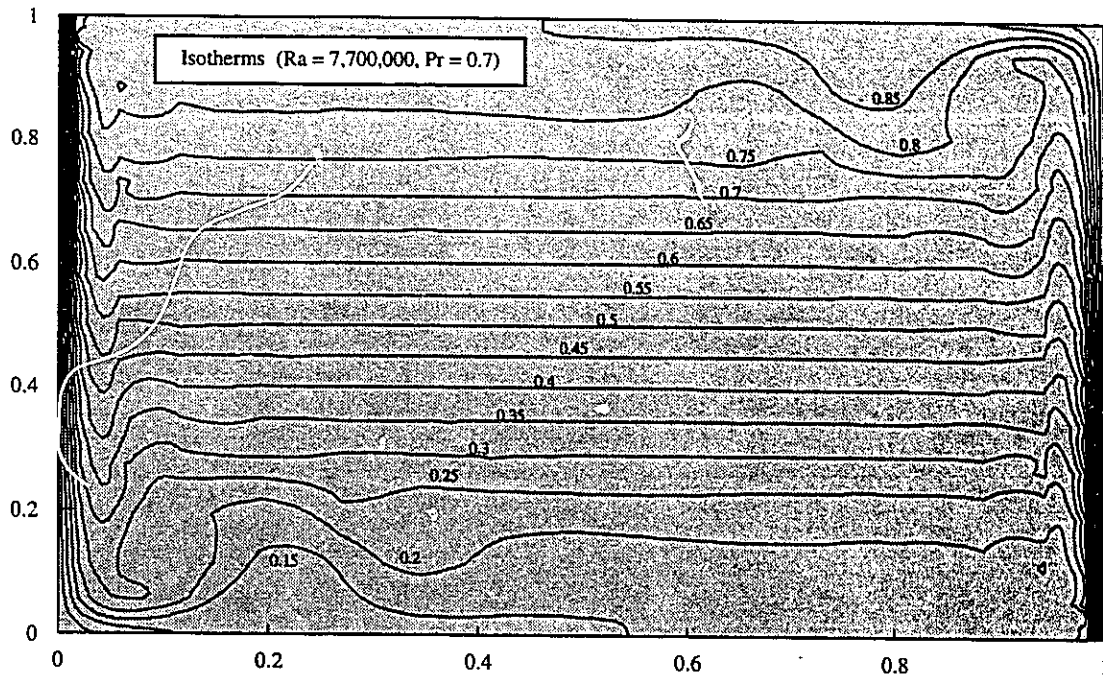


Figure 2.4 Classical square-cavity problem (isotherms distribution)

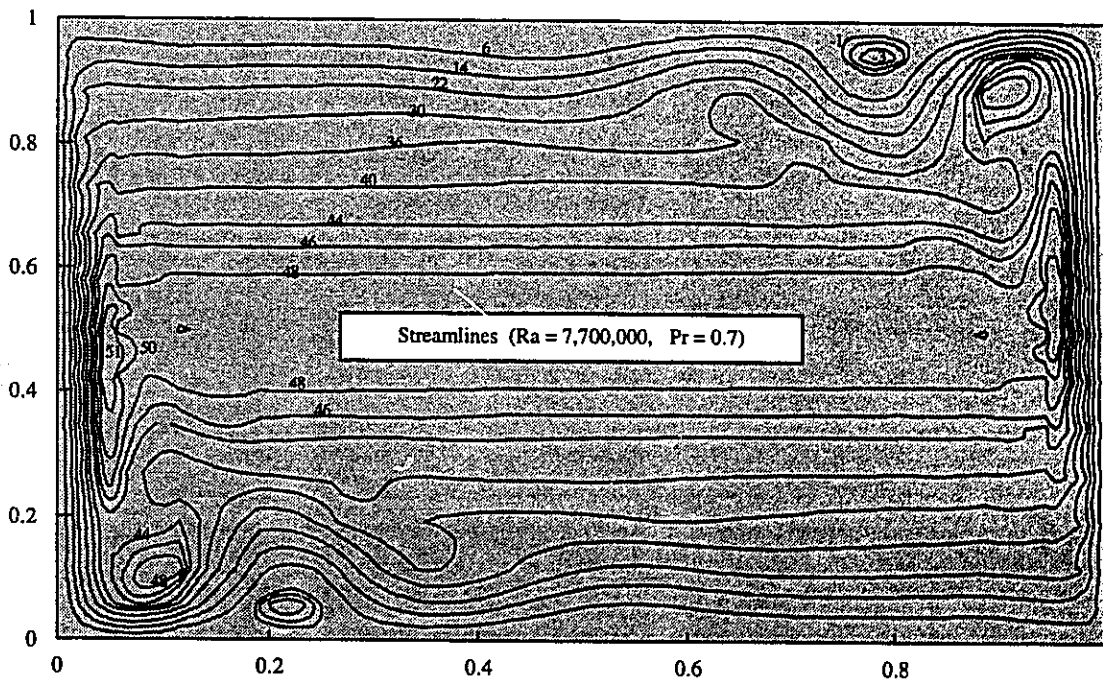


Figure 2.5 Classical square-cavity problem (streamlines distribution)

2.5.2 Cavities Embedded in a Square Domain; a Segregated FEM Strategy

Since one of the main objectives of this study is to analyze the effect of empty cavities on the overall heat transfer rate across solid bodies, two solid square domains (20x20 cm each) were considered: one with a square cavity and the second with a cylindrical one. Both were subjected to the same type of boundary conditions: constant heat flux on the right side and convection on the left side. Figure 2.6 summarizes the conditions and the parameters used in this study.

In the solid body, outside the cavity, pure conduction occurs, whereas, inside the cavity, combined conduction, free convection and radiation take place. A simultaneous solution of the heat transfer inside and outside the cavity has been shown to require reasonably large computer memory. We propose here a segregated approach in which the solid body is treated separately from the embedded cavity. At the first iteration, the solid part of the domain is solved (equation 2.39) by imposing a vacuum inside the cavity, hence yielding the Neumann condition: $-K_s \frac{\partial T}{\partial n} = q_r$. This means that only radiation is considered between the segments facing each other along the cavity wall. The resulting temperature distribution at the air-solid interface is then used as a Dirichlet boundary condition in the cavity problem.

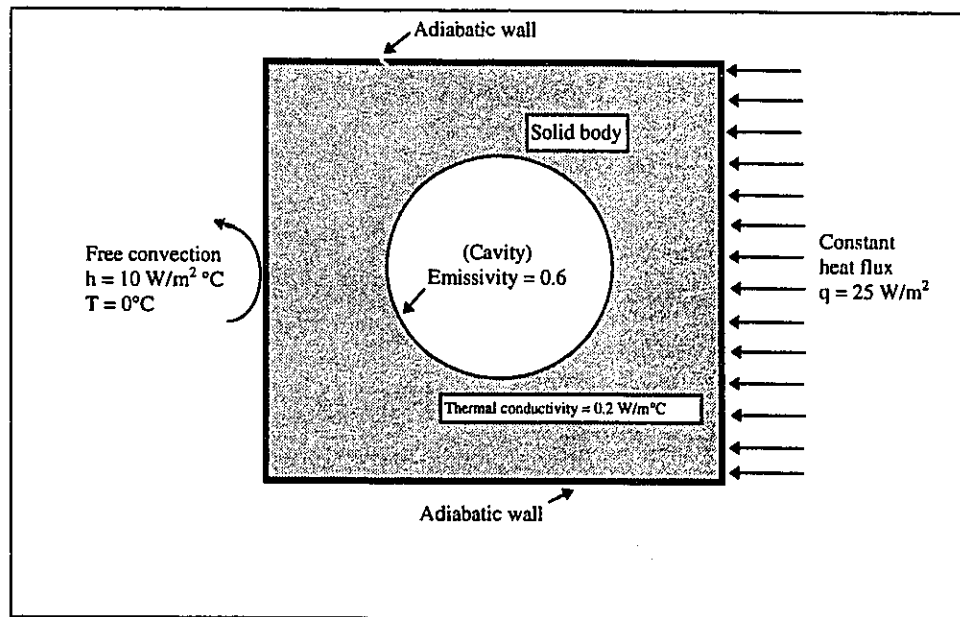
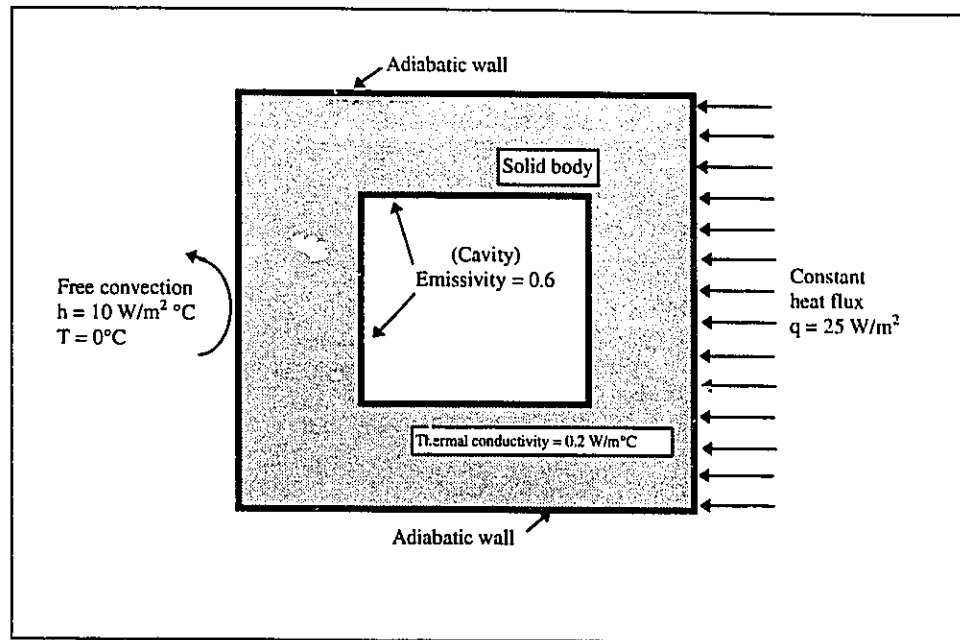


Figure 2.6 Cases studied: square and cylindrical empty cavities inside a square solid domain

At the next step, equations (2.6) to (2.8) are solved simultaneously and the interface heat flux resulting from conduction and free convection inside the cavity is calculated. The latter is added to the heat flux resulting from radiation and imposed as a Neumann boundary along the cavity wall, for the next conduction calculation. This Neumann-Dirichlet iterative procedure is repeated to convergence, which usually occurs after 6 to 8 iterations. A flowchart of the procedure is shown in table 2.2.

To assess the individual effects of radiation and natural convection, three cases are considered: First, the cavity wall was considered as insulated (adiabatic), i.e., with no heat exchange by conduction, free convection or radiation. The calculated maximum temperatures under the test conditions outlined in figure 2.6 were 48.4°C and 45.8°C for the square and the cylindrical cavity, respectively. Figure 2.7 shows the isotherms inside the solid regions surrounding both cavities.

Second, if vacuum is established inside the cavity and insulation removed from the walls, i.e. heat is exchanged by radiation only, the maximum temperatures drop to 27.0°C and 27.2°C, respectively.

Finally, if the cavities are assumed to be filled with air, simultaneous conduction, free convection and radiation further improve the overall heat exchange and the maximum reference temperatures drop to 24.2°C and 24.4°C, respectively. Figure 2.8 shows the isotherms inside the cavities and their surroundings.

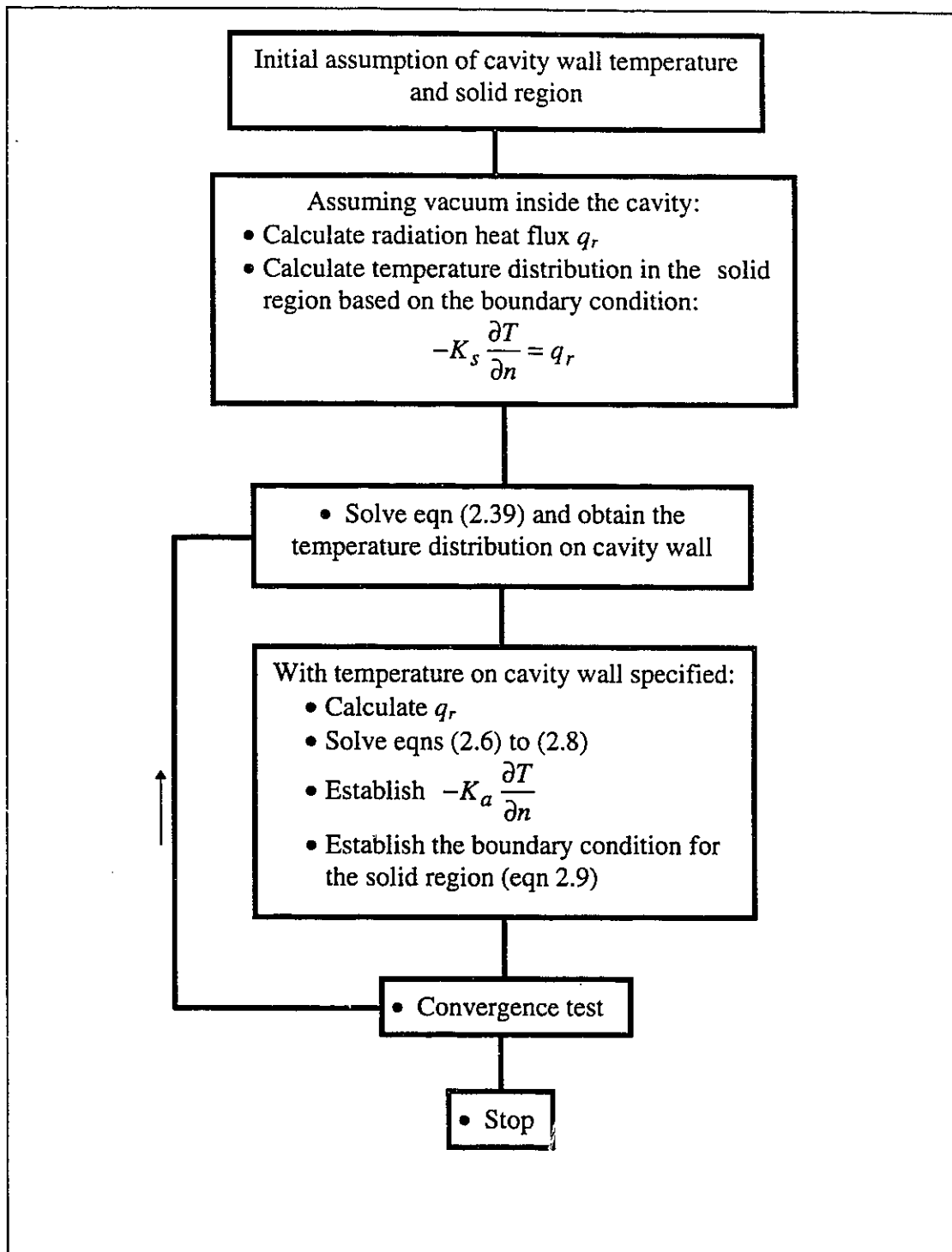


Table 2.2 Calculation procedure in a cavity problem

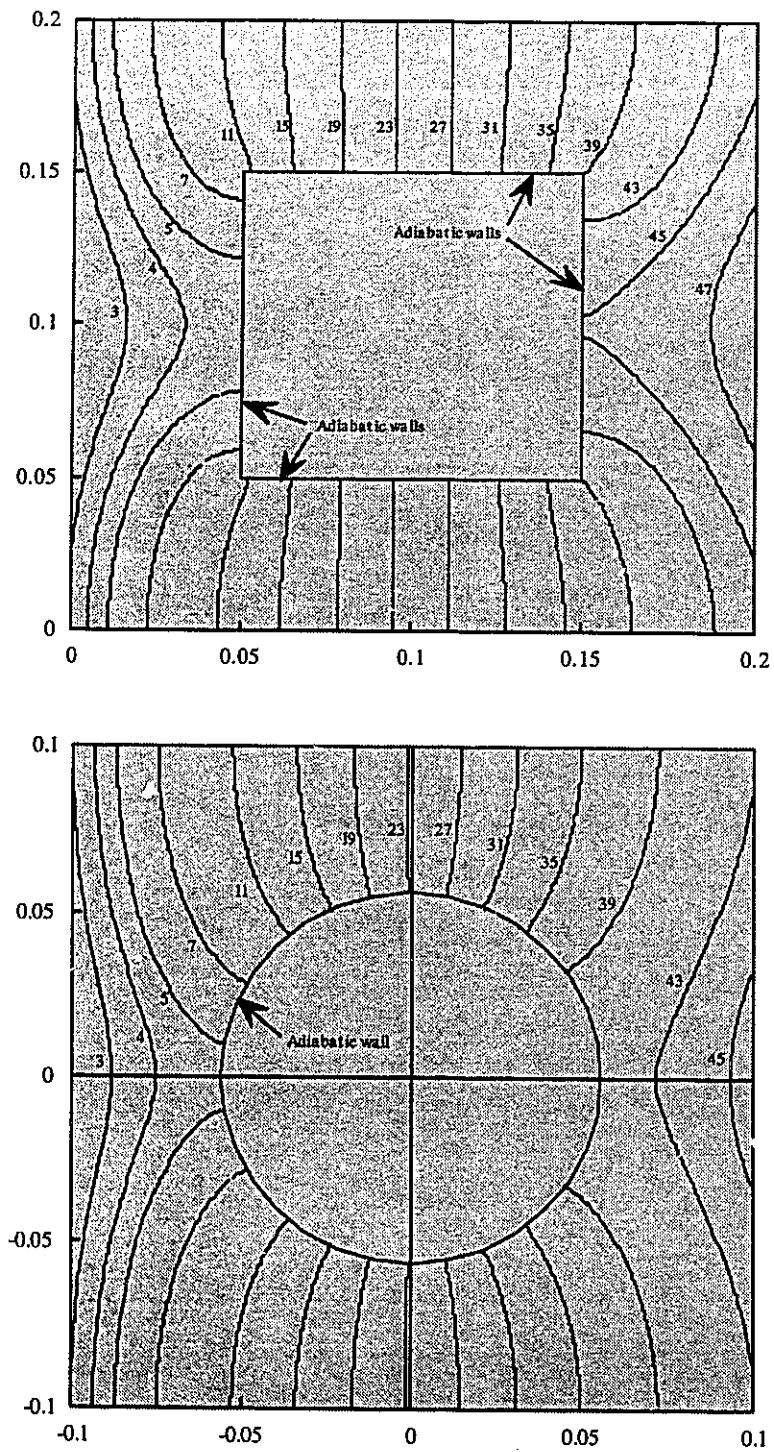


Figure 2.7 Isotherms (°C) inside the solid domain (adiabatic cavity wall)

The heat flux at the the wall, derived from the temperature field inside the cylindrical cavity is shown in figure 2.9; negative heat flux meaning heat is entering the cavity. This flux is used to calculate an equivalent fictitious free convection coefficient h_i using the following standard formulation:

$$k_a \frac{\partial T}{\partial X} = h_i (T_i - T_\infty) \quad (2.69)$$

where subscript i represents the segment number along the cavity wall and k_a is the thermal conductivity of the air and the bulk temperature is taken to be the average wall temperature T_∞ of the cavity. Figure 2.10 shows the distribution of this coefficient along the duct wall. The two singularities shown in this figure occur at the particular wall segments where the temperature value approaches the arbitrarily selected bulk temperature. Although it is physically impossible to have a free convection coefficient reaching infinity, the duct area along which these singularities apply is however infinitesimally small. Therefore, they can be neglected.

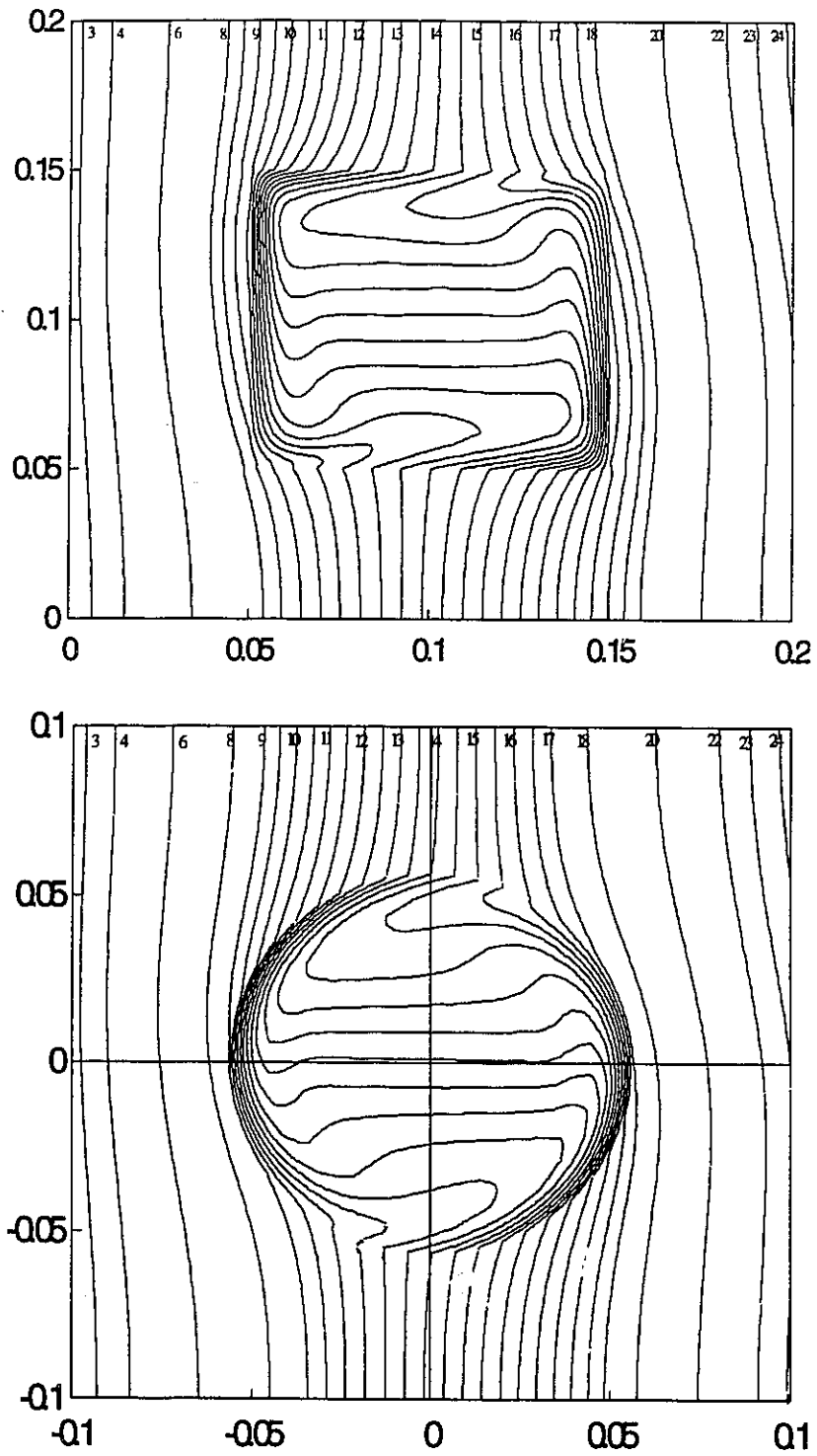


Figure 2.8 Isotherms ($^{\circ}\text{C}$) for the whole domain, including the cavities

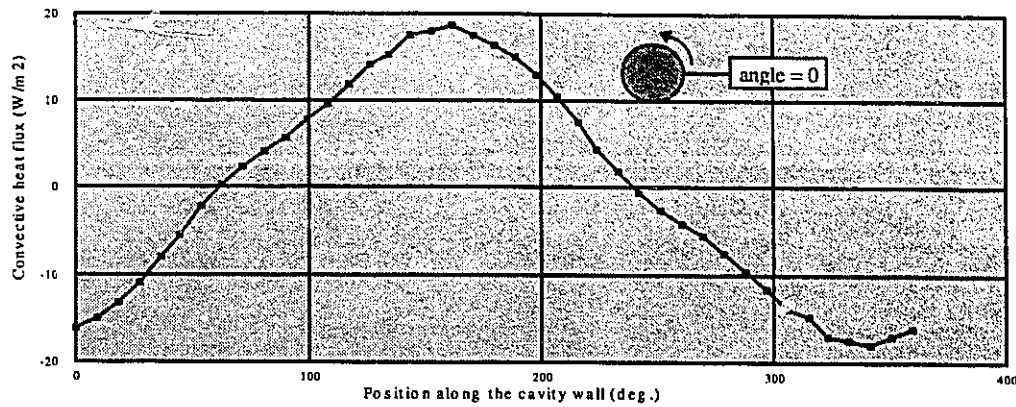


Figure 2.9 Free convection heat flux distribution along the cylindrical cavity wall

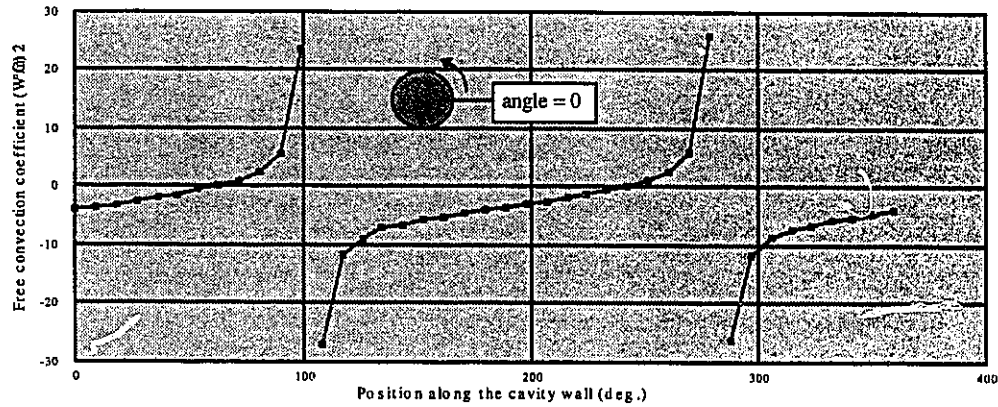


Figure 2.10 Equivalent free convection coefficient along the cylindrical cavity wall

Subsequently, if this derived free convection coefficient is imposed as a boundary condition along the wall of the cavity, then the whole domain (cavity and solid body) can be analyzed in one step, as a conduction problem, by only solving the Fourier partial differential equation (2.39). In this case, the cavity is considered as an open boundary exposed to radiation and free convection with a specified heat transfer coefficient and unspecified bulk temperature. In the finite element conduction code, this previously unknown temperature is calculated at each iteration by averaging the wall temperature of the cavity.

The temperature distribution inside the solid body obtained by the above-described simplified analysis agrees well with the results of the earlier detailed analyses that solve the whole set of convection-conduction equations (2.6) to (2.8) and (2.39). Thus, this demonstrates that a complex setup, consisting of scattered cavities embedded in a solid domain, could be analyzed more simply by considering the cavity as an open boundary and solving only for heat conduction in the solid domain. Obviously, this procedure requires the use of an appropriate convection coefficient that can only be exactly found by carrying the detailed analyses described previously.

In order to capitalize on the above approach, however, we have investigated the effect of the heat transfer coefficient value. We have repeated the analysis of the solid square domain with the cylindrical cavity, using an average value of $3.0 \text{ W/m}^2\text{°C}$ for the free convection coefficient calculated from the local values shown in figure 2.10. The comparison between the temperature distributions calculated with the detailed analysis and the one using the average free convection coefficient is shown in figures 2.11a and 2.11b. It can be seen that both give practically the same maximum and minimum temperatures inside the solid domain and the same average temperatures of the duct, with slight discrepancies elsewhere.

The calculated average free convection coefficient of $3 \text{ W/m}^2\text{°C}$ lies in the range of the heat transfer coefficient commonly encountered in natural convection (horizontal or vertical plates, cylinders etc.) at low Rayleigh numbers ($Ra = 1,000 - 20,000$). This is the

range encountered in underground cable installations in general. For practical purposes, one can use this coefficient as an approximation, with some confidence that no significant error is likely to be introduced in the calculation. In fact, a large variation in this coefficient has little effect on the outcome of the analysis, since the largest part of the heat is exchanged by radiation, which is accounted for quite accurately. As an example, an increase of the average free convection coefficient from 3 to 5 W/m²°C introduces a decrease in the maximum temperature of less than 1°C as can be seen in figure 2.11c.

Therefore, as a preliminary conclusion, an empty duct could be treated as an open boundary, with a bulk temperature equal to the average wall temperature and with a free convection coefficient of the order of 3 W/m²°C. At the same time, the radiation heat exchange can be exactly accounted for by calculating the individual shape factors of the various segments that constitute the cavity wall and solving for the net radiation heat flux at each iteration.

Despite these simplifications, the calculation procedure is still tedious and long, especially when dealing with large duct banks containing several empty ducts.

A further simplification to this problem consists in treating an empty duct as a duct populated by a fictitious unloaded cable and will be discussed in detail later in this chapter.

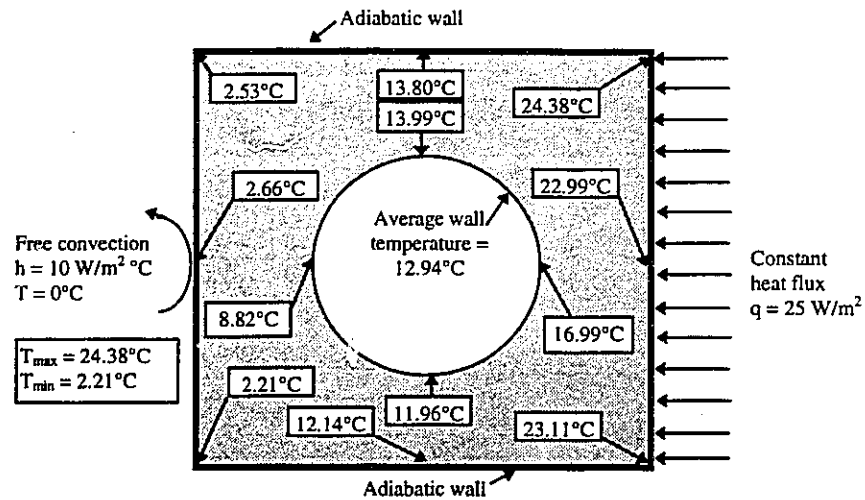
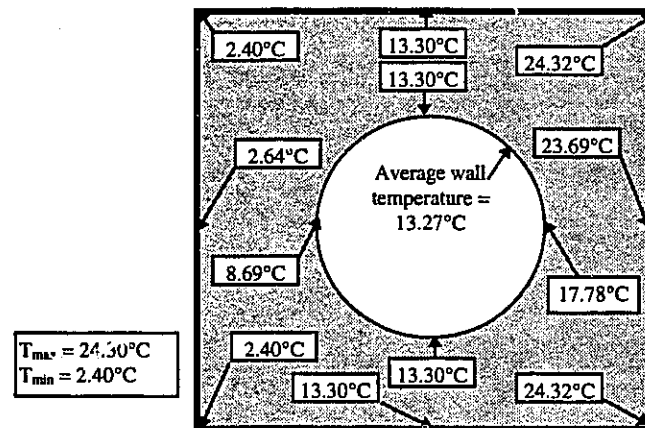
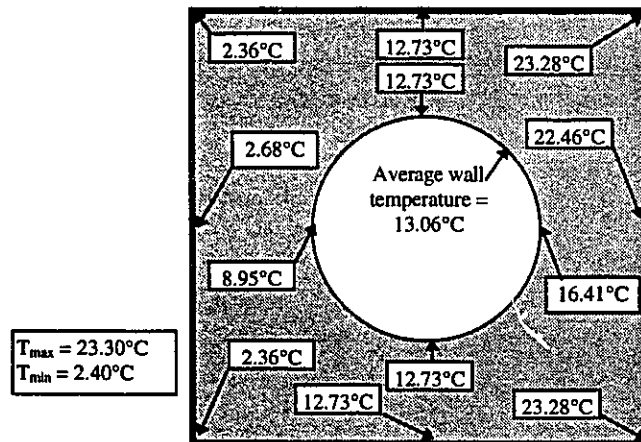


Figure 2-11a: Temperature distribution with detailed calculation

Figure 2-11b: Temperature distribution with simplified calculation:
($h = 3 \text{ W/m}^2\text{°C}$)Figure 2-11c: Temperature distribution with simplified calculation:
($h = 5 \text{ W/m}^2\text{°C}$)

2.6 Cavities With Internal Heat Source: Applications to the Heat Transfer Between Cable and Duct

The study of this type of cavities is motivated by the need to evaluate, with improved accuracy compared to analytical methods, the heat transfer between cable and cable-retaining duct. In fact, the thermal resistance of the air gap between cable and duct represents an important portion of the overall thermal resistance in a duct bank installation. A drop of approximately 20% occurs in the current-carrying capacity (ampacity) of an underground installation if the cables are installed inside ducts instead of being directly buried. Therefore, an accurate calculation of this parameter is necessary to obtain a precise ampacity evaluation of the installation.

The common practice in electrical utilities, as mentioned in the introduction, is to calculate the thermal resistance between cable and duct based on a simple set of equations derived by Neher and Buller [16] 45 years ago. The basic principles, assumptions and simplifications of this method are the following:

- In practice, along a duct bank, a cable may occupy various positions inside the duct ranging from concentric to eccentric and the cable may even touch the bottom of the duct along its route. The first assumption of the analytical approach, however, considers the cable-duct configuration as a concentric one. This means that the problem is viewed as concentric annuli in which the cable represents the inner

annulus and the duct is the outer one. In the case of a three-phase duct bank installation, where three cables may be bonded and twisted together inside each duct, the calculation procedure consists in replacing these cables by a single fictitious one, having an outside diameter equal to the diameter of the circumscribing circle (figure 2.12). Similar procedures are applied to other cases.

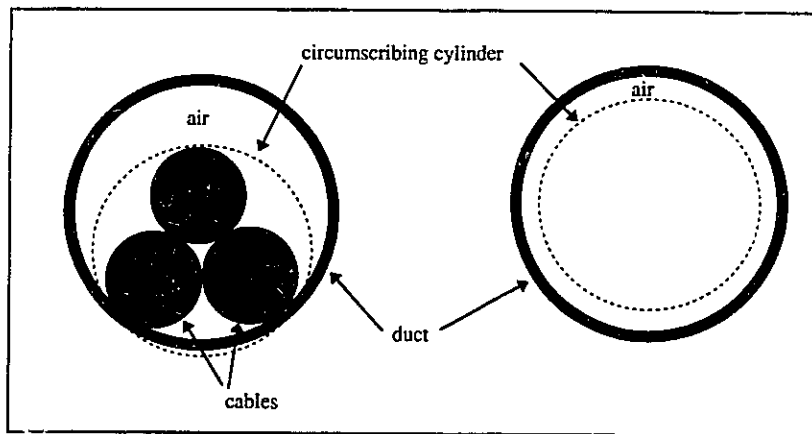


Figure 2.12 Simulation of three-phase circuit in duct by one phase

- The surface of the cable and the inner surface of the duct are considered isotherms. This is a valid assumption with respect to the cable due to its inherent construction, but is not always the case of the duct whose temperature is calculated by averaging the wall temperature along its inner surface.
- The heat exchange between cable and duct is a combination of three distinct heat transfer modes acting in parallel. The first is free-convection, the second is conduction and the last is radiation. The Neher-Buller approach [16] evaluates the free-convection resistance as a temperature drop being concentrated in two films, one

at the surface of the cable and the other at the inner surface of the enclosing duct. It uses the following semi-empirical formula derived by McAdams [17] to calculate the heat dissipation across a convective boundary layer

$$Q_{cv} = 0.092 \cdot D_f^{0.75} \Delta T_f^{1.25} \quad (2.70)$$

where Q_{cv} in W/ft is the heat exchanged by convection, D_f is the film diameter in inches and ΔT_f is the temperature drop across the film in °C.

Applying equation (2.70) to both films, and combining the individual resistances in parallel, Neher and Buller [16] came out, after some simplifications, with the following formula for the free convection component:

$$\frac{Q_{cv}}{\Delta T} = \frac{0.092 \cdot D_{ce}^{0.75} \cdot (T_{cs} - T_{di})^{0.25}}{1.39 + \frac{D_{ce}}{D_{di}}} \quad (2.71)$$

The conduction component of the overall thermal resistance is calculated by the following equation:

$$\frac{Q_{cd}}{\Delta T} = \frac{0.0213}{\log_{10} \left(\frac{D_{di}}{D_{ce}} \right)} \quad (2.72)$$

The calculation of the radiation component assumes that the cable surface and the duct's internal surface have the same emissivity. The view factor of the cable with respect to the duct is equal to 1 (the cable does not see part of itself and its completely surrounded by the duct). The heat exchange by radiation is given by the following equation [16]:

$$\frac{Q_{rd}}{\Delta T} = 0.102 \cdot D_{ce} \cdot \epsilon \left[1 + 0.0167 \left(\frac{T_{cs} + T_{di}}{2} \right) \right] \quad (2.73)$$

All units in equations (2.70) to (2.73) are kept as they appear in the references. Q_{cv} , Q_{cd} and Q_{rd} are the heats (W/ft) exchanged by convection, conduction and radiation respectively, D_{ce} (in) the cable diameter, D_{di} (in) the duct inside diameter, T_{cs} and T_{di} the temperatures of cable and duct in °C and ϵ the surface emissivity.

Equations (2.71) to (2.73) are the formulae commonly used to calculate the overall thermal resistance between cable and duct. They apply under the normal operating conditions of underground cables, namely between 20°C and 100°C.

The validity of these equations were extensively investigated in the present work. A multitude of experimental tests were conducted in which cables were placed inside a duct in both concentric or eccentric positions. The tests were carried out in two different setups. In the first one, the cable and duct assembly was exposed to air, while in the second the duct was buried inside a 30x30 cm sandbox (figure 2.13). In these setups, each of the real cables was replaced by two concentric metallic tubes of similar dimensions, filled with heating element in the center. The dielectric layer which occupy the space inside the annuli, was replaced by dry sand. The experimental results show a negligible effect of the cable eccentricity on cable temperature in the buried configuration

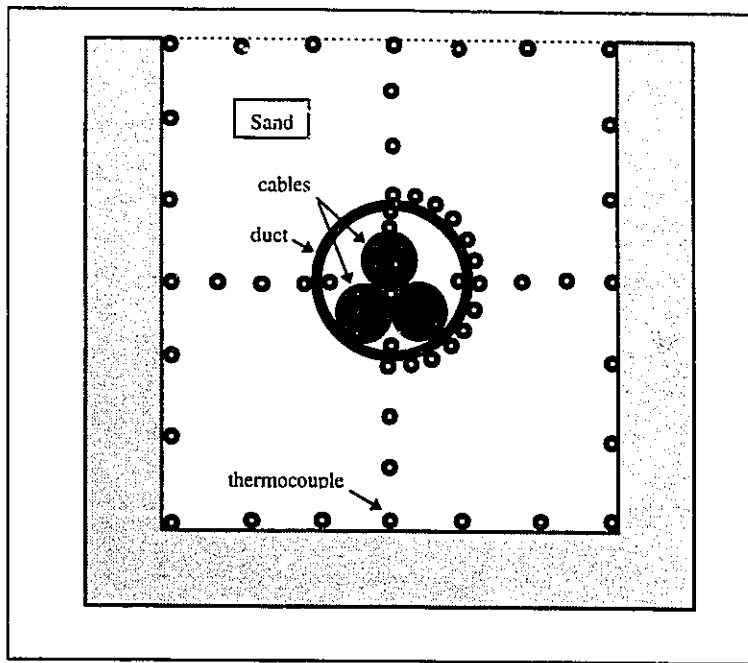


Figure 2.13 Experimental sand box

(table 2.3), while a slight influence was detected in the configuration exposed to air (table 2.4). In the latter case, the concentric position yielded the highest cable temperature. Therefore, the assumption of treating the cable and duct as concentric annuli is shown to be valid. In any case, this situation represents the worst conditions encountered in real life along the cable route.

The second conclusion of the experimental study is that good agreement between the measurements and the empirical equations (2.71) to (2.73) was obtained only in the case when the cable and duct surface emissivities were considered equal to a value smaller than their actual values (0.7 instead of 0.98-0.99). A plausible explanation of this discrepancy is the following: equation (2.71) of the simplistic approach does in fact





Duct/Cable configuration	Test #	Heat loss (W/m)	T-conduct. (°C)	T-cab. surf. (°C)	T-duct surf. average
	83-1	35.2	88.8	77.8	62.1
	85-1	44.1	103.4	90.3	73.4
	83-2	35.2	88.2	77.3	62.9
	83-5	44.8	103.9	90.2	73.1
	83-7	34.7	80.6	77.8	61.2
	83-6	44.8	95.5	91.4	73.7
	83-8	35.4	80.7	77.5	62.7

Table 2.3 Experimental data: buried cable/duct installation

include the combined effect of both conductive and convective thermal resistances and not only the convective one as outlined previously. It is suspected that the author of reference [16] has misinterpreted the theory advanced by McAdams [17]. Therefore, the thermal resistance due to conduction has to be discarded from the global resistance calculation. In other words, only equations (2.71) and (2.73) are to be considered when calculating the thermal resistance of the air gap.

Table 2.5 shows the comparison between experimental and theoretical results using the actual emissivity value of 0.98. The comparison is done using the combination of equations (2.71) to (2.73), by first including and then excluding equation (2.72) which




Duct/Cable Configuration	Test #	Heat loss (W/m)	T-amb. (°C)	T-conduct. (°C)	T-surf. (°C)	T-duct (°C)
$L/D_i = 25$ 	35-1	10.3	23.9	34.8	31.3	26.6
	35-2	19.5	24.6	44.5	38.1	29.5
	31-2	31.6	25.3	57.0	46.9	33.8
	35-3	46.6	24.9	70.6	55.8	37.5
$L/D_i = 25$ 	36-1	10.3	25.0	36.9	33.4	27.7
	36-2	19.5	24.0	46.0	39.6	29.3
	26-1	31.6	24.5	58.4	48.3	32.9
	36-3	46.6	25.1	72.9	58.0	37.2
$L/D_i = 33$ 	46-1	19.5	23.9	46.5	40.3	30.5
	46-2	31.6	23.8	58.2	48.1	33.2
	46-3	46.6	24.4	72.9	58.5	38.0

Table 2.4 Experimental data: cable/duct installation exposed to air

TEST #	MEASURED VALUES		CALCULATED VALUES (eqns 2.71, 2.72 and 2.73) ($\epsilon = 0.98$)		CALCULATED VALUES (eqns 2.71 and 2.73 only) ($\epsilon = 0.98$)	
	T-cond. (°C)	T-duct (°C)	T-cond. (°C)	T-duct (°C)	T-cond. (°C)	T-duct (°C)
36-1	36.9	27.7	36.1	28.1	36.9	28.1
36-2	46.0	29.3	44.2	29.5	45.6	29.5
26-1	58.4	32.9	56.1	33.0	57.9	33.0
36-3	72.9	36.3	70.0	37.0	72.3	37.0

Table 2.5 Comparison between measured and analytically calculated temperatures

accounts for the conduction component. It can be seen that by only combining equations (2.71) and (2.73) gives a better agreement with the measured values.

To better understand the heat dissipation inside the air gap between cable and duct, a detailed simulation of this process was conducted by solving the stream function, vorticity

and energy equations (2.6) to (2.8) and (2.39). Similarly to the analysis of empty duct discussed previously, the radiation heat exchange was decoupled and solved separately at each iteration. The view factors were calculated according to Hottel's cross-link method, taking into account the blockage caused by the presence of the cable inside the duct.

The heat transfer inside an annulus has been studied quite extensively in the literature. Several authors [18, 19, 20] have published data in the form of equivalent conductivity, which is the ratio of combined convection and conduction heat exchange to conduction alone. The equivalent conductivity was found to be a function of the Rayleigh number, Prandtl number and the ratio of the air gap to the inner cylinder diameter (L/D_i). A large data bank is available in the literature for $L/D_i = 0.8$. In underground installations, the dominant L/D_i ratio lies between 0.1 and 0.35 which to our knowledge, has not been fully considered in previous investigations.

As a first step, a case study with an L/D_i ratio of 0.8 and with a Rayleigh number ranging from 1,000 to 50,000 was carried out. The Prandtl number was kept equal to 0.7 during this study. Figure 2.14 shows the isotherms and the streamlines distribution inside an annuli at $Ra=50,000$. The corresponding equivalent conductivity distribution is shown in figure 2.15. The results agree well with the available data in the literature [18].

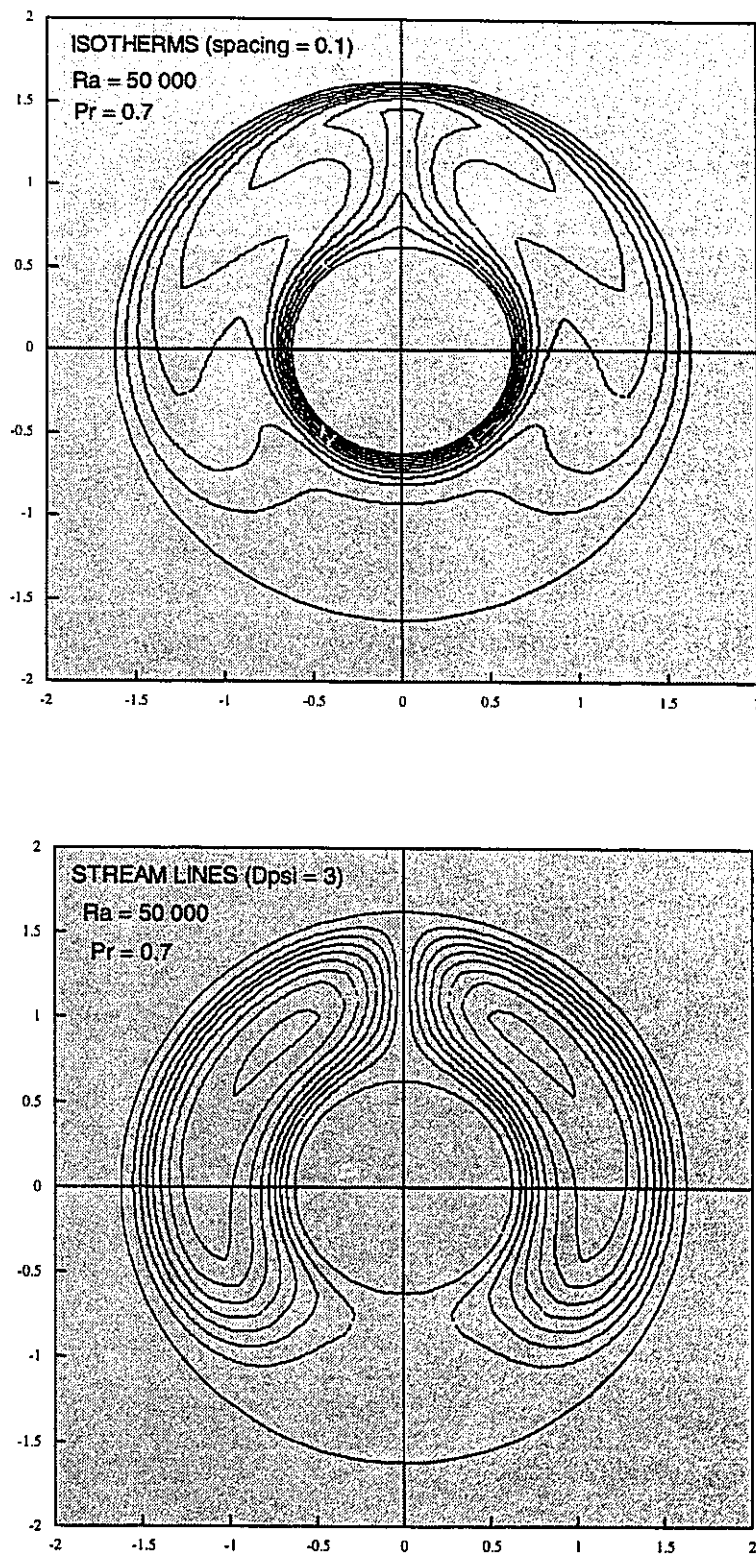


Figure 2.14 Isotherms and streamlines distribution in annuli
($Ra = 50,000$; $Pr = 0.7$; $L/D_i = 0.8$)

The second step consisted in analyzing an L/D_i ratio of 0.25 at various Rayleigh numbers. This ratio corresponds to the experimental setup used in this study, which closely matches real life configurations (cable diameter = 76 mm, duct inner diameter = 114 mm). The range of interest for Rayleigh number lies between 0 and 20,000. This interval covers the extreme temperatures encountered in service.

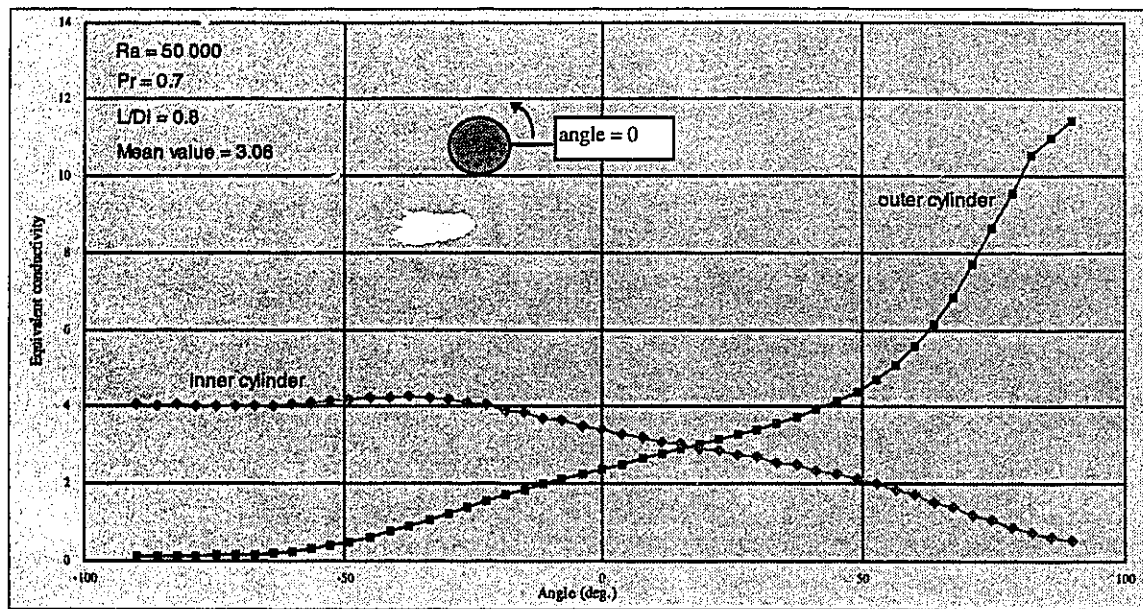


Figure 2.15 Local equivalent conductivity distribution
($Ra = 50,000$; $Pr = 0.7$; $L/D_i = 0.8$)

Figure 2.16 shows the equivalent conductivity distribution as a function of the location along the duct wall at various Rayleigh numbers ($Ra = 4,000, 8,000, 12,000, 16,000$ and $20,000$). The average values of the equivalent conductivity in terms of Rayleigh number are shown in figure 2.17.

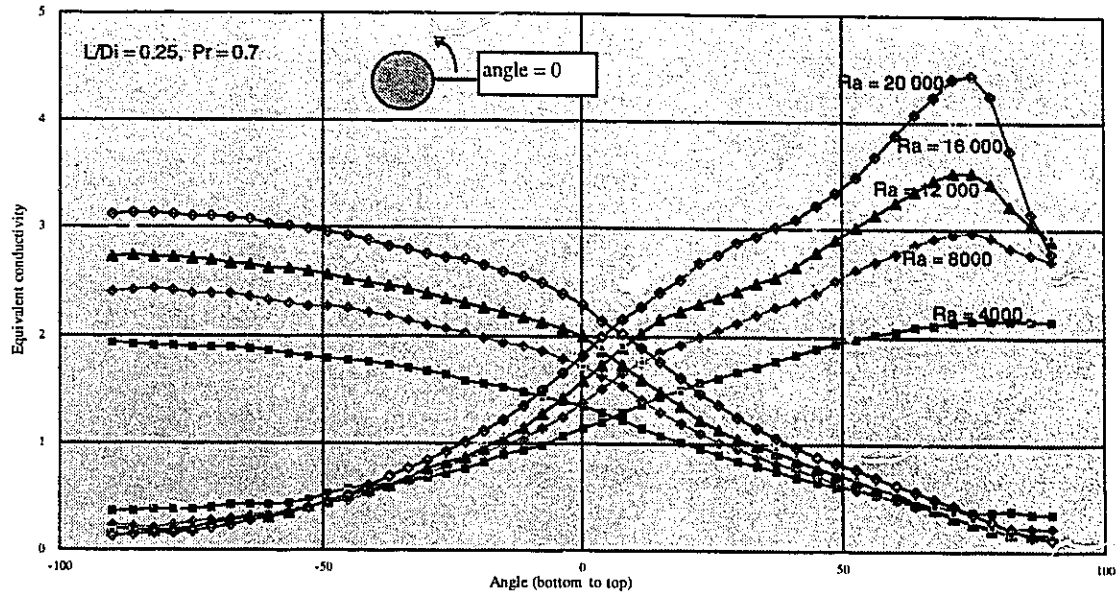


Figure 2.16 Local equivalent conductivity distribution at various Rayleigh numbers
($Pr = 0.7$; $L/D_i = 0.25$)

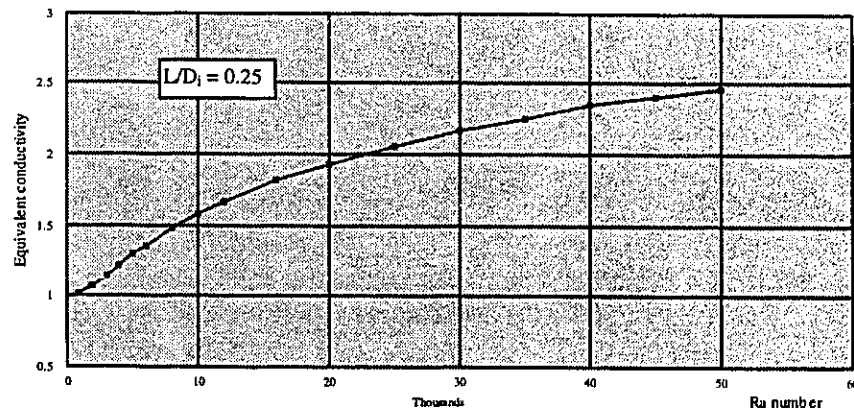


Figure 2.17 Average equivalent conductivity distribution at various Rayleigh numbers
($Pr = 0.7$; $L/D_i = 0.25$)

The equation that better fits the equivalent conductivity distribution shown in figure 2.17 is the following:

$$K_{eq} = -1.67394 \frac{-Ra}{e^{0.0002205}} + 2.621875 \quad (2.74)$$

Based on the above results, the analysis of tests 36-1, 36-2, 36-3 and 26-1 shown in table 2.4 was repeated using the equivalent conductivity formulation of equation (2.74). This approach is fully justified in the case of cable/duct in concentric position exposed to air, since the cable surface is isothermal and that of the duct varies little from top to bottom as can be seen in figure 2.18. This figure shows the measured temperature values of test 26-1. The results summarized in table 2.6 fit better the experimental values than the standard analytical calculation shown previously in table 2.5.

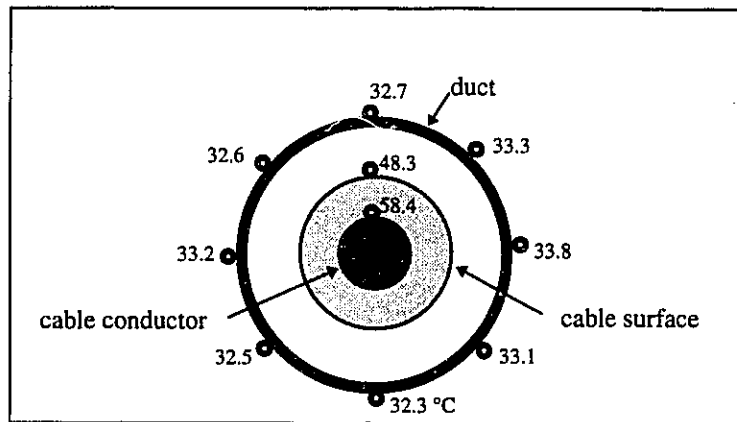


Figure 2.18 Measured temperatures in cable/duct installation exposed to air (test 26-1)

Measured values			Calculated values ($\epsilon = 0.98$)					
Test #	Heat loss (W/m)	T-cond. (°C)	Ra	Kequiv.	Q (W/m) (conv. & cond.)	Q (rad.) (W/m)	T-cond. (°C)	Deviat. (°C)
36-1	10.3	36.9	3204	1.174	2.5	7.8	37.0	0.1
36-2	19.5	46.0	5364	1.309	5.1	14.5	45.8	-0.2
26-1	31.6	58.4	7332	1.421	8.5	23.2	58.3	-0.1
36-3	46.6	72.9	8995	1.509	12.6	34.0	72.9	0.0

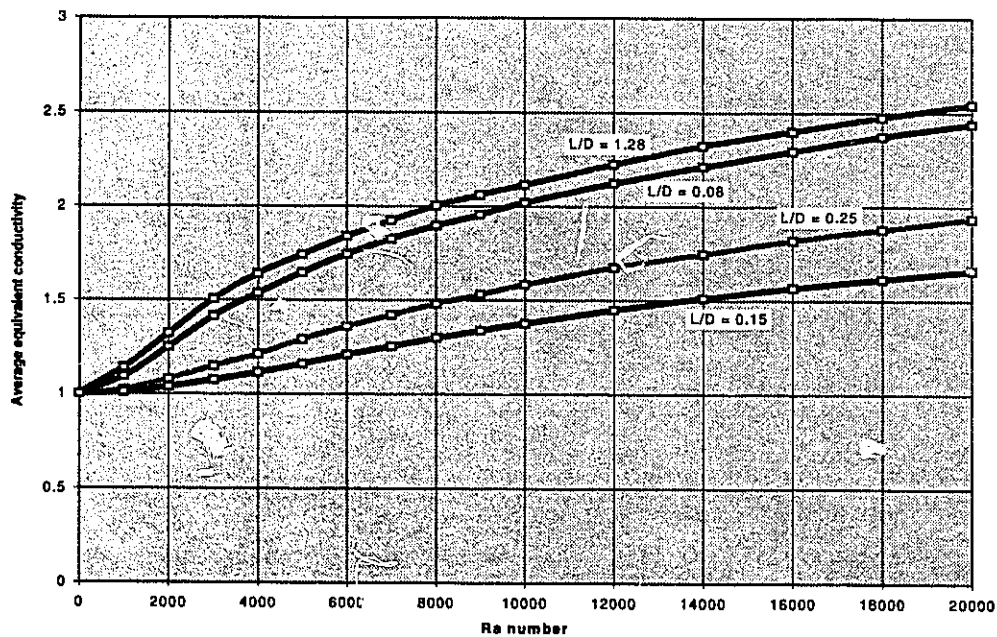
Table 2.6 Comparison between measured and numerically calculated values

The results of table 2.6 shows the important role of the radiation heat exchange across the air gap between cable and duct. In fact, approximately 3 times more heat is exchanged by radiation than by combined free convection and conduction. This suggests that care should be taken to insure a high surface emissivity of both cable and duct to improve the current-carrying capacity of the installation. One complementary test with shiny cable surface had in fact shown an 18.2°C increase in conductor temperature, compared to the same cable with blackened surface under the same conditions of test 36-3.

As was mentioned before, the dominant L/D_i ratio in underground installations lies between 0.1 and 0.35 which covers most three-phase circuit configurations in either 4.5" ducts or 5" ducts. The cables normally used in these installations are the standard 350 MCM, 500 MCM, 750 MCM and 1000 MCM (1 MCM = 0.5067 mm²). Occasionally, in a distribution network, we may find single phase circuits (one cable inside the duct) that produce an L/D_i ratio greater than 0.35. Table 2.7 shows the various configurations that may be encountered in underground installations and the corresponding L/D_i ratios. The average equivalent conductivity distribution associated with the L/D_i range of interest is shown in figure 2.19.

		Cable size (MCM)	Diameter D_i (m)	Air gap L (m)	L/D_i
Three-phase circuit	4.5" duct	3 x 350	0.077	0.019	0.25
		3 x 500	0.089	0.013	0.15
		3 x 750	0.100	0.007	0.07
	5.0" duct	3 x 350	0.077	0.025	0.32
		3 x 500	0.089	0.019	0.21
		3 x 750	0.100	0.013	0.13
		3 x 1000	0.111	0.008	0.07
One-phase circuit	4.5" duct	1 x 350	0.036	0.039	1.08
		1 x 500	0.041	0.036	0.88
		1 x 750	0.047	0.034	0.72
		1 x 1000	0.052	0.031	0.60
	5.0" duct	1 x 350	0.036	0.046	1.28
		1 x 500	0.041	0.043	1.05
		1 x 750	0.047	0.040	0.85
		1 x 1000	0.052	0.038	0.73

Table 2.7 Configurations encountered in underground cable installations

Figure 2.19 Average equivalent conductivity distribution at various L/D_i ratios

2.7 Effect of a Non-Isothermal Duct Surface on the Overall Heat Exchange

To examine the effect of a non-isothermal duct surface on the overall heat exchange between cable and retaining duct, we have analyzed in detail the thermal behavior of the sand box assembly shown in figure 2.13 under the following conditions (test 85-1 of table 2.3):

- Concentric cable/duct configuration with an L/D_i ratio of 0.25;
- Current inside the cable (heating road) of 7.294 Amp producing a heat generation rate of 44.1 W/m;
- Constant ambient temperature of 22.3 °C;
- Sand thermal conductivity of 0.323 W/m°C;
- Insulation thermal conductivity of 0.033 W/m°C.

As in the case of empty duct analysis, the solution to this problem was obtained iteratively by decoupling the radiation from the natural convection as shown in the flowchart of table 2.8.

The resulting isotherms inside the cable, the air gap and the sand box for this particular test are shown in figure 2.20. The comparison between measured and computed temperature distributions is shown in figure 2.21. The largest discrepancy occurs at the bottom of the duct and is equal to 1.6°C.

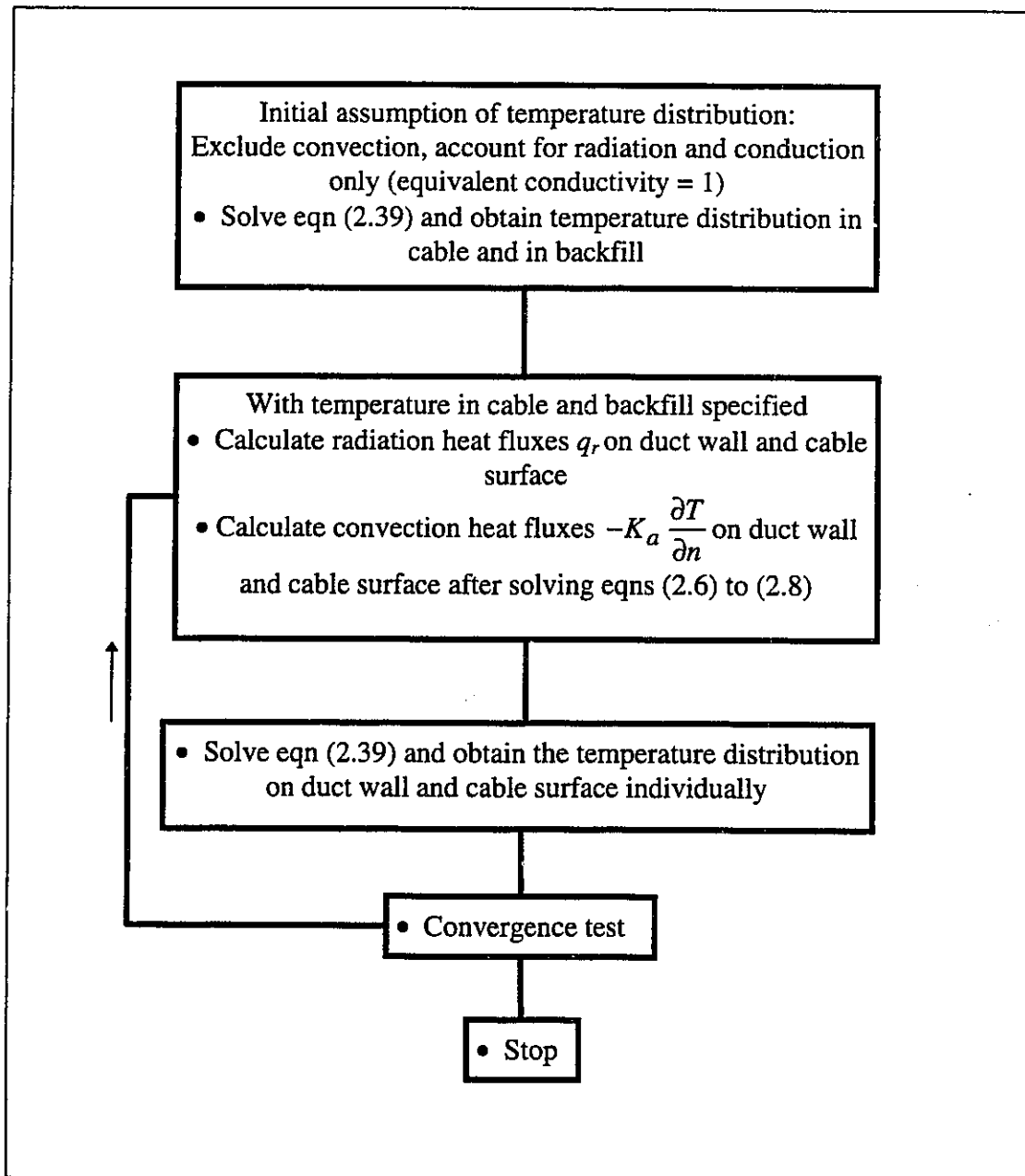


Table 2.8 Iterative calculation procedure in cable/duct/backfill configuration

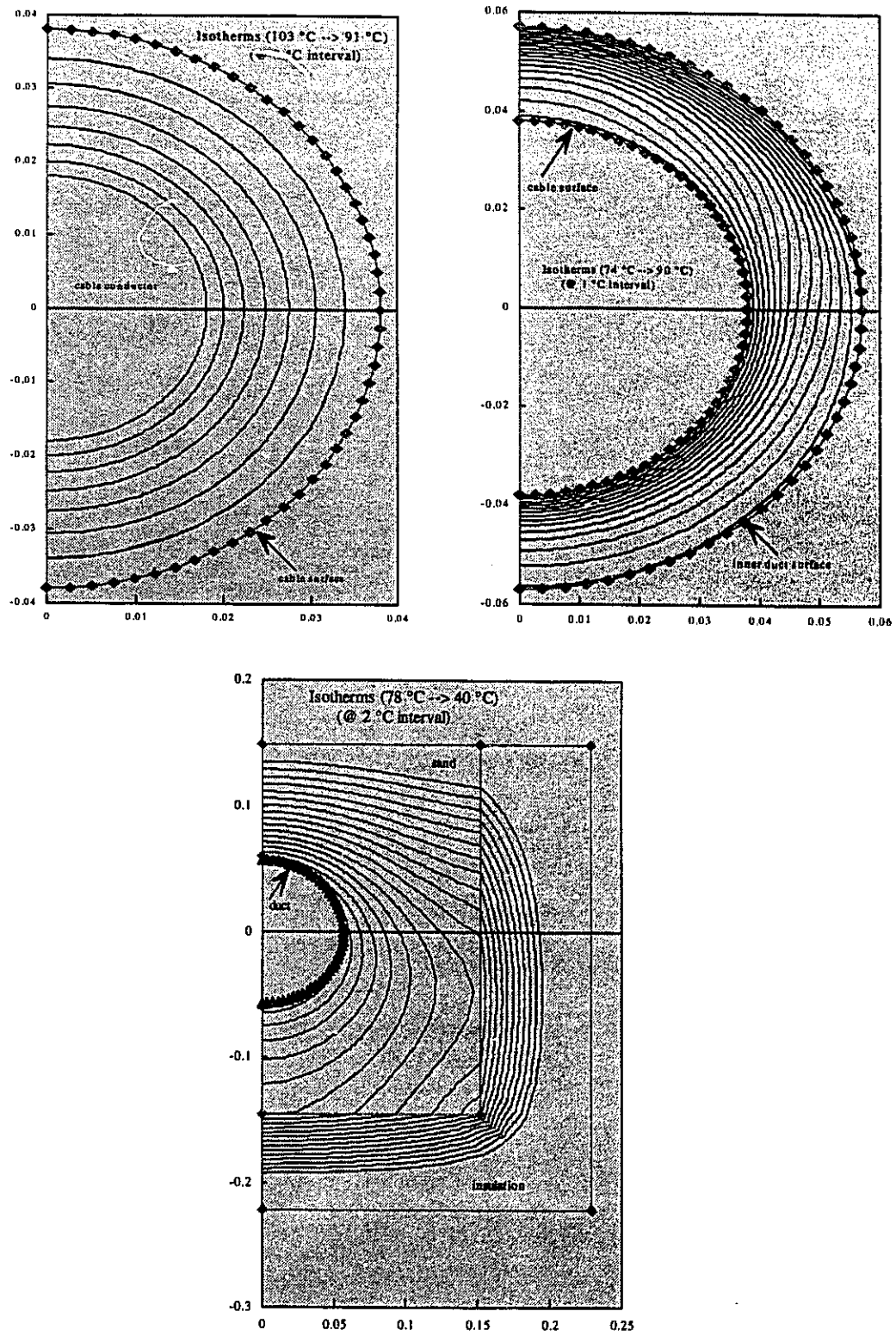


Figure 2.20 Isotherms (°C) inside the cable, the air gap and the sand box

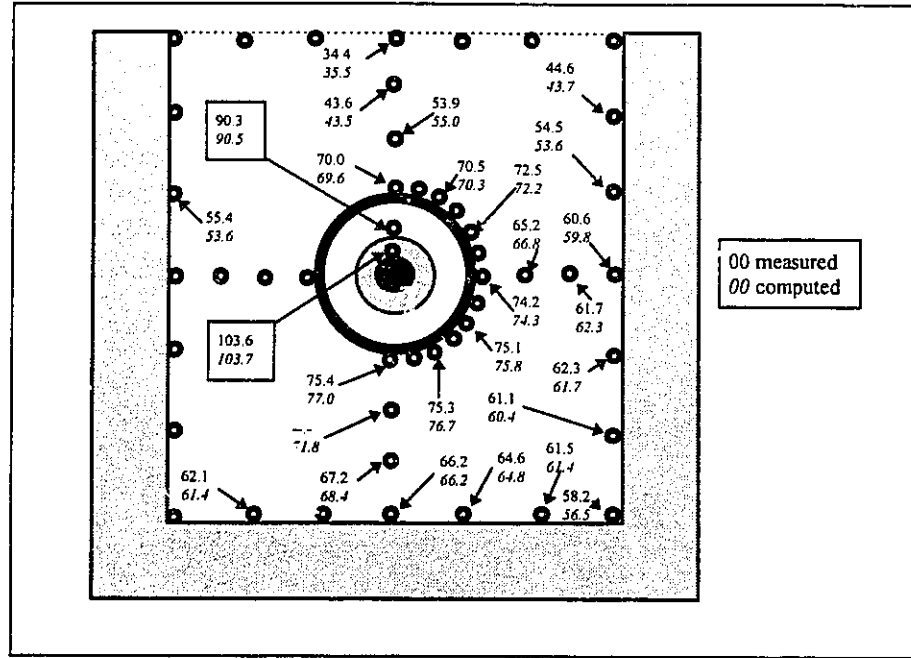


Figure 2.21 Comparison between measured and computed temperature distributions
(detailed analysis)

The calculated net radiation heat flux (absorbed - emitted) striking the inside surface of the duct as well as the combined convective conductive heat flux distribution is shown in figure 2.22. It can be seen that the convective-conductive heat flux increases several folds from the bottom of the duct to the top, whereas the radiation is almost uniform. Consequently, a large error is unlikely to occur if one calculates the radiation heat flux between cable and duct by assuming both surfaces as isotherms, with a view factor equal to 1, using the following standard formula [15]:

$$Q_{rad} = 5.6697 \cdot 10^{-8} \cdot A_{cs} (T_{cs}^4 - T_{di}^4) / \left(\frac{1}{\epsilon_{cs}} + \frac{A_{cs}}{A_{di}} \cdot \left(\frac{1}{\epsilon_{di}} - 1 \right) \right) \quad (2.75)$$

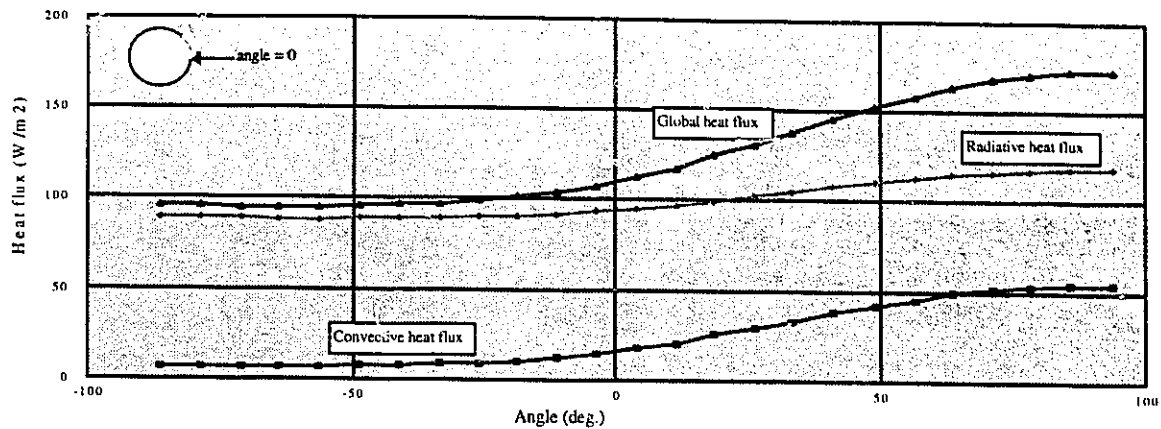


Figure 2.22 Convective and radiative heat flux distribution along the duct wall

Where A is the surface, T is the surface temperature in K , ϵ is the emissivity. Subscripts cs and di designate the cable and the duct surface, respectively. It should be stated that in practice, cables are usually surrounded by concrete or other thermal backfills that have higher thermal conductivity (lower thermal resistivity) than the dry sand used in the test assembly. This would suggest that temperature variation along the duct is less pronounced than the present measurements shown in figure 2.21. This means that the radiation heat exchange calculated by the previous equation (2.75) would generate an even smaller error than in the present test conditions.

Another assumption that further simplifies the analysis without introducing a meaningful error consists in using the average equivalent conductivity instead of using the local one that varies along the duct wall. By looking at figure 2.22, we could be under the impression that the error would be rather great due to the significant variation of the conductive convective heat flux from the bottom to top. However, the portion of the global heat flux striking the inside surface of the duct resulting from free convection and

conduction is quite small compared with the radiation component which is more or less uniform. Consequently, the global heat flux can also be considered more or less uniform, especially in the case of a more conductive backfill encountered in practice.

To better evaluate the impact of the simplifications proposed above, we have repeated the analysis of the sand box assembly shown in figure 2.13 under the same conditions of test 85-1. Figure 2.23 shows the comparison between the measured and the calculated values. We can conclude that both the detailed analysis (figure 2.21) and the simplified one (figure 2.23) calculate the cable temperature with reasonable accuracy. As for the temperature distributions inside the sand, the detailed analysis shows a better agreement with the measurements than the simplified one. The discrepancy is however negligible and has no meaningful effect on the cable capacity calculation as will be discussed later in chapter 5.

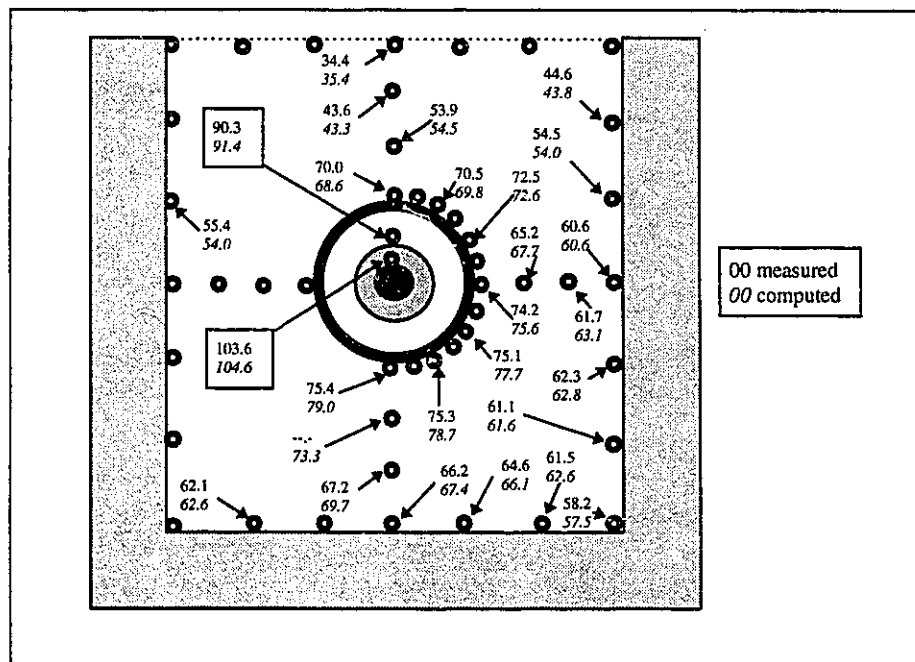


Figure 2.23 Comparison between measured and computed temperature distributions (simplified analysis)

2.8 Empty Duct Analysis, Revisited

As reported earlier, the detailed analysis of an empty duct is quite complex and cumbersome. It is therefore unwise to integrate this procedure into a finite element code for cable ampacity calculation which is meant to be simple and fast. We have discussed in the preceding section several simplifications to account for the free convection, conduction and radiation inside the air space between cable and retaining duct. The same simplifications can also be applied in the case of empty cavities by simply considering them as cavities populated with fictitious small unloaded cables that do not generate any heat. This allows us to use the equivalent conductivity concept (equation 2.74) and the standard simple equation for radiation heat exchange (equation 2.75). Consequently, greatly simplifying the analysis. The reasoning behind this approach is that an empty duct is in fact equivalent to a populated duct with an L/D_i ratio equal to infinity. This condition can be achieved approximately by using either a large air gap or a small size cable. The analysis of the solid square domain containing the cylindrical cavity (figure 2.6) based on the latest simplification with an L/D_i ratio of 0.25 yields a maximum and minimum temperature of 24.4 °C and 2.4 °C respectively (see figure 2.24). Additional experimental validation of this approach will be outlined in greater detail in chapter 5.

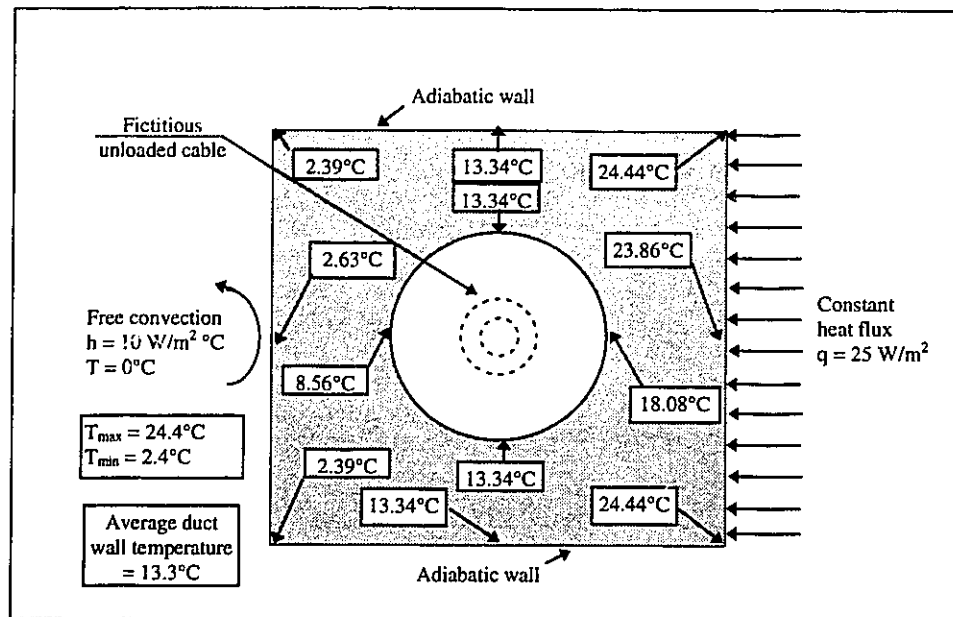


Figure 2.24 Temperature distributions in the cylindrical empty cavity (fictitious cable approach)

3. A Special Finite Element for Ampacity Calculation

As was mentioned in chapter 1, the transient analysis of an underground cable installation implies the meshing of all cable's layers in order to take into account the influence of their thermal capacity on the temperature variation. This meshing, called here the Full-Mesh Approach, adds hundreds of nodes (algebraic equations) to the regular mesh of the domain surrounding the cables. Therefore, compared to the conventional steady-state analysis which may not require the meshing of the cables, the resulting system of equations is substantially larger and requires more computer memory and longer execution time. Our objective to conduct cable ampacity calculations on personal computers implies necessarily a severe restriction on the size of the problem. Therefore, it is highly desirable to reduce the size of the finite element mesh without compromising on accuracy. This chapter outlines a new technique in the field of cable ampacity calculation dubbed here as EFECAC [21, 22] (Economic Finite Element for Cable Ampacity Calculation) that leads to great saving in time and effort while improving the accuracy in comparison with the conventional Full-Mesh Approach.

3.1 Basic Principles of the Approach

A typical high voltage power cable is composed of a hollow or plain conductor that carries the current (figures 1.2 and 3.1). The inside of the hollow conductor is filled with synthetic oil. A layer of dielectric material surrounds the conductor to insulate the cable surface from the high voltage. This layer is covered by metallic sheath made commonly

from lead or aluminum. The external anti-corrosion layer is made from polyethylene or PVC. Its role is to protect the cable from external mechanical or chemical damages. In the case of DC (Direct Current) installation, the heat source is located in the conductor only. In the case of AC (Alternating Current), two additional heat sources are present: the first one is in the dielectric layer due to the high voltage, and the second one is in the metallic sheath due to the induced current. In either AC or DC cases, the finite element mesh inside these layers should be dense enough to capture accurately the large temperature gradient that prevails in these regions, particularly across the dielectric layer.

In the conventional Full-Mesh Approach where the cables and their surrounding are treated as a single Cartesian domain, the number of circumferential subdivisions inside the cable should be equal to the one along the cable-surrounding interface to ensure mesh continuity and better accuracy. The density of the radial subdivisions depends on the desired precision. For large size oil-filled cables, it is practical to use, as shown in figure 3.1, three radial subdivisions in the anti-corrosion layer, three in the metallic sheath, seven in the dielectric, five in the conductor and three in the oil channel. For example, with such a radial mesh density, coupled with 12 subdivisions along the circumference, the resulting number of nodes and elements in one cable would be equal to 252 each. The heat dissipation in this case is fully described by the following diffusion partial differential equation:

$$k\left(\frac{\partial^2 T}{\partial X^2} + \frac{\partial^2 T}{\partial Y^2} + \frac{\partial^2 T}{\partial Z^2}\right) + Q = \rho C \frac{\partial T}{\partial t} \quad (3.1)$$

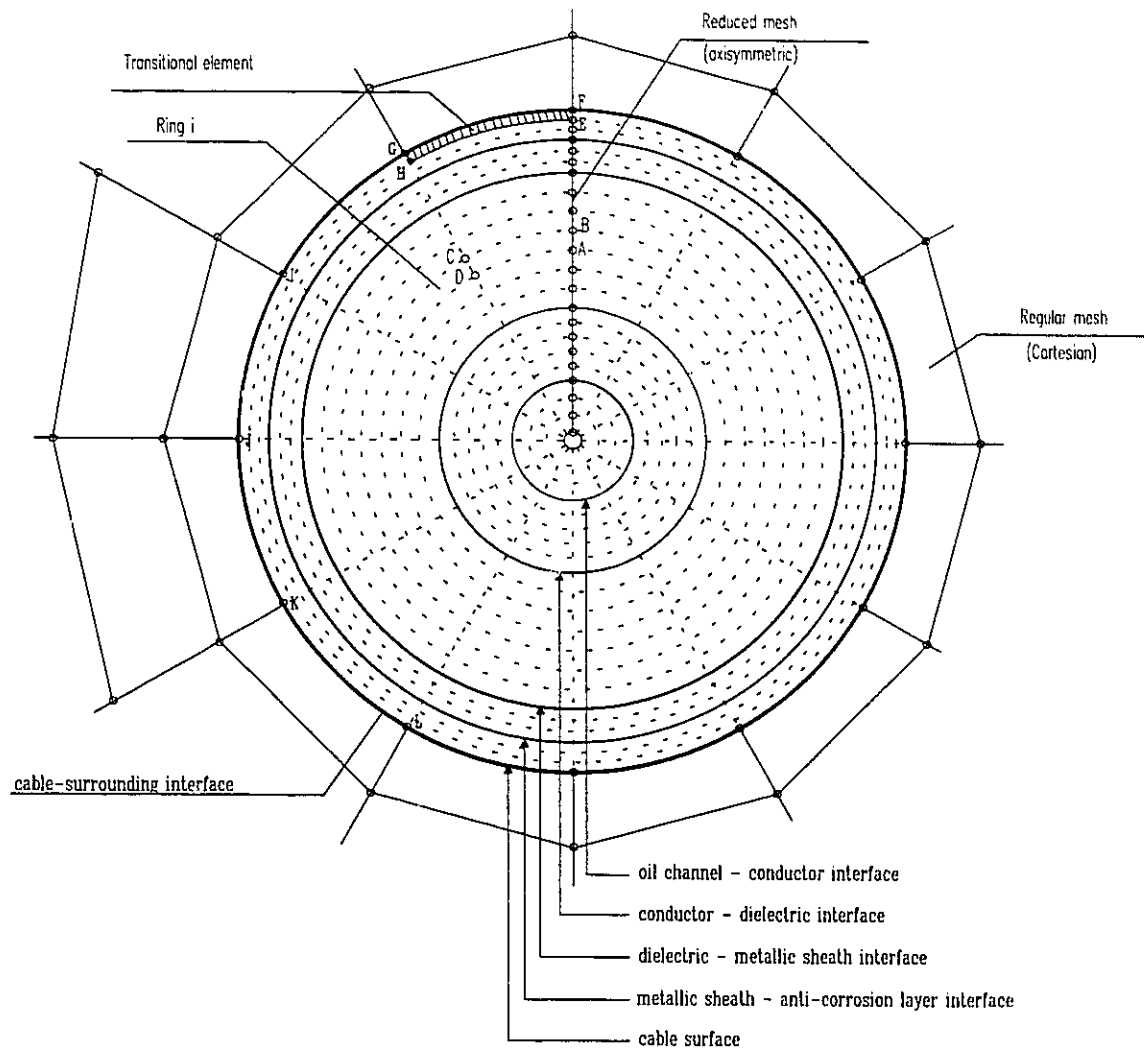


Figure 3.1 Link between Cartesian and polar finite element meshes

where T is the temperature, t is the time, Q is the heat source, ρ is the density, C is the thermal capacity and k is the thermal conductivity

The EFECAC approach considers the temperature inside the cable as uniform along a given radius due to the inherent shape and construction of the cable. The heat dissipation at that location can therefore be described by one of the following partial differential

equations:

- in a 1-D axisymmetric case:

$$k \left(\frac{1}{R} \frac{\partial T}{\partial R} + \frac{\partial^2 T}{\partial R^2} \right) + Q = \rho C \frac{\partial T}{\partial t} \quad (3.2)$$

- in a 2-D axisymmetric case:

$$k \left(\frac{1}{R} \frac{\partial T}{\partial R} + \frac{\partial^2 T}{\partial R^2} + \frac{\partial^2 T}{\partial Z^2} \right) + Q = \rho C \frac{\partial T}{\partial t} \quad (3.3)$$

where R and Z are the radial and axial coordinates, respectively.

Equations (3.2) or (3.3) apply at the nodes belonging to the "reduced" mesh located inside the cable (figure 3.1), whereas equation (3.1) applies at all other nodes in the regular mesh. The link between the regular mesh outside the cable and the reduced mesh inside the cable is ensured by the so-called "transitional" elements. It is sufficient to consider one such element per cable (element EFGH in figure 3.1) since the other elements on the interface ring have the same "element conductivity matrix" (providing that the circumferential subdivision is uniform). This element is formed by three real nodes (nodes E, F and G) and by one fictitious node (node H). This last node must occupy the same position as the one normally generated by the conventional Full-Mesh Approach. The element conductivity matrix is assembled as many times as the number of circumferential divisions along the cable-domain interface; each time with another pair of nodes located on the cable surface, namely: nodes G, I then I, J, etc.

An alternative to this approach permits the analysis to be carried out completely in the Cartesian coordinates by solving equation (3.1) only [21]. This is done by generating other fictitious nodes along the various layers of the cable similar to the one generated for the transitional element. As an example, let us consider the element (ABCD) located inside the dielectric layer of the cable, as shown in figure 3.1. The conductivity matrix of this element is similar to the neighboring ones on the same ring because they have the same material and the same geometry. Also, the temperature of the nodes along this ring is uniform. Therefore, all 24 nodes of the 12 elements of the ring #i can be replaced by two real nodes and a single element. This element is named "reduced element". It is formed by two real nodes (A and B) and 2 fictitious ones (C and D). The location of the fictitious nodes can occupy the same position as the nodes normally generated by the conventional approach. Their role is to give the element the necessary shape to calculate the conductivity matrix. Once this element matrix is evaluated, it is assembled into the global one as many time as the number of elements normally generated by the conventional approach (12 times in the example on figure 3.1).

The accuracy of this alternative approach can be further enhanced by using a finer grid in θ direction. In other words, bringing the fictitious nodes closer to each other as well as the real nodes of all the "reduced elements". By doing so, the resulting elements which are formed by four straight sided segments will smooth better the curved surface of the ring. For example, if the distance along the ring between the fictitious nodes C, D and the real nodes A, B is cut down by half, the resulting error in element area of meshing the

curved surfaces by straight segments will decrease from 4.5% to 1.1%. Obviously, in this case, the element conductivity matrix has to be assembled twice instead. The more we get the fictitious nodes closer to the real nodes, the more we approach the ideal case of axisymmetric analysis inside the cable, described earlier. In the conventional Full-Mesh Approach, one has to introduce a correction factor to the internal heat source and thermal capacity to compensate for the area lost due to the meshing of the curved layers of the cable by straight sided elements. The EFECAC technique does not require such a correction. Therefore it can give a better accuracy compared to the conventional method with much faster execution time. In other words, the EFECAC technique ensures an optimum linkage between the planar domain of the surrounding medium and the axisymmetric domain inside the cables.

The mesh generation procedure in the EFECAC approach is accomplished in three steps. First the regular mesh is constructed where the discretization procedure stops at the cable surface or at the duct surface, if any. Second, the "transitional" elements are defined. Finally, the axisymmetric elements ("reduced elements") and attached nodes are generated. In our example, the 252 nodes and the 252 elements which are necessary to mesh one cable in the conventional Full-Mesh Approach, will be reduced to only 21 nodes and 21 elements in the proposed EFECAC method.

3.2 A Practical Example

The advantages of this new technique can be better appreciated through the example of a practical cable installation where a three-phase circuit of a 735 kV AC cables is buried inside a concrete slab. The characteristics of the cable, operating and boundary conditions are shown in figure 3.2.

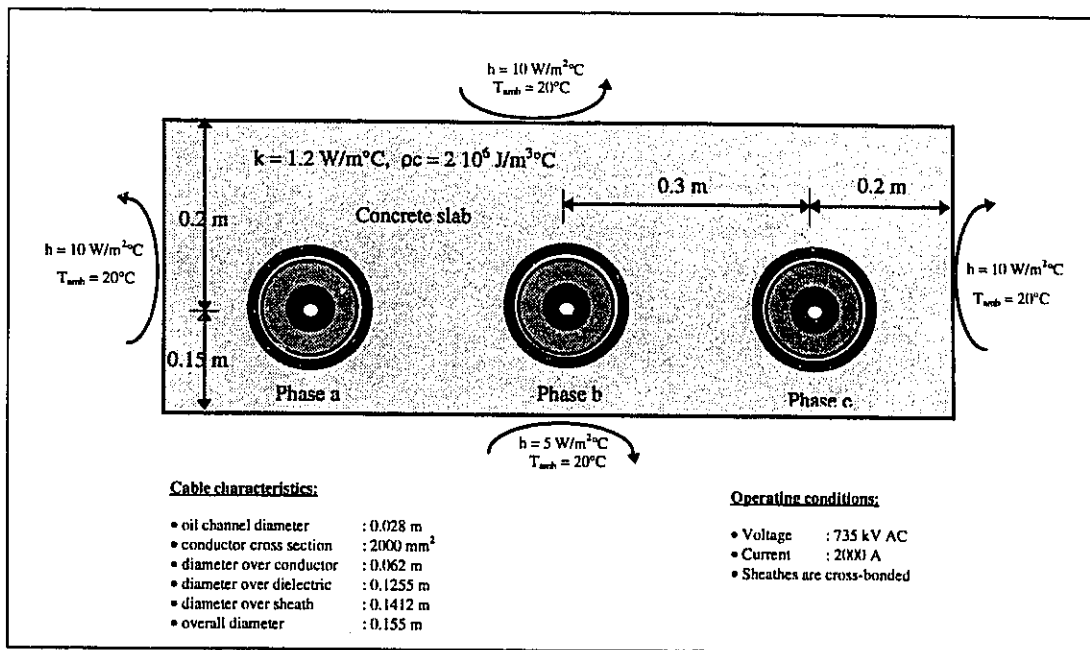


Figure 3.2 Example of a three-phase circuit buried in concrete slab

Figure 3.3 shows the required finite element mesh when the conventional Full-Mesh Approach is adopted. In the new method, the regular mesh stops at the cable-concrete interface as shown in figure 3.4. The comparison between the results obtained by using both approaches is shown in table 3.1 and figure 3.5. It can be seen that the proposed method gives essentially the same results as the conventional one, but with much less execution time and computer memory.

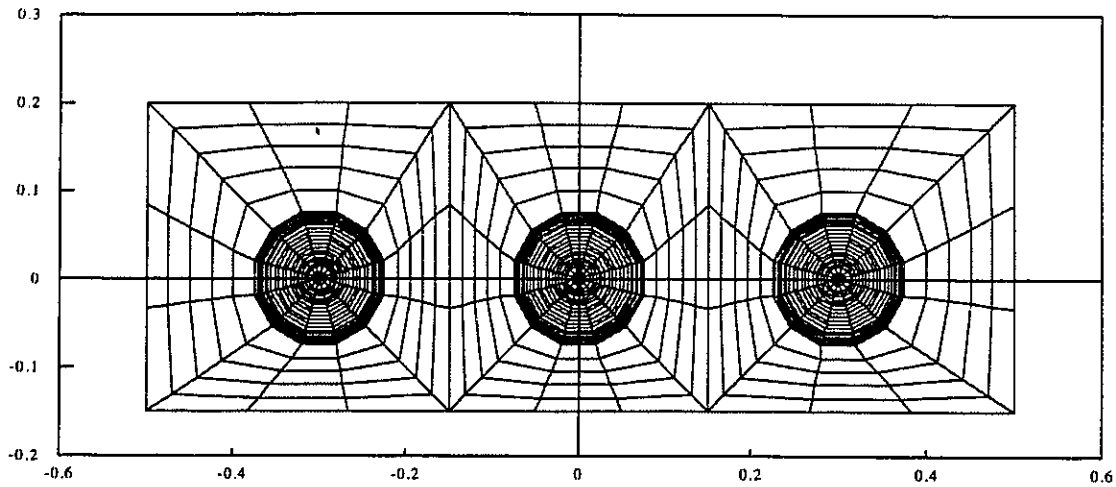


Figure 3.3 Finite element mesh: conventional Full-Mesh Approach

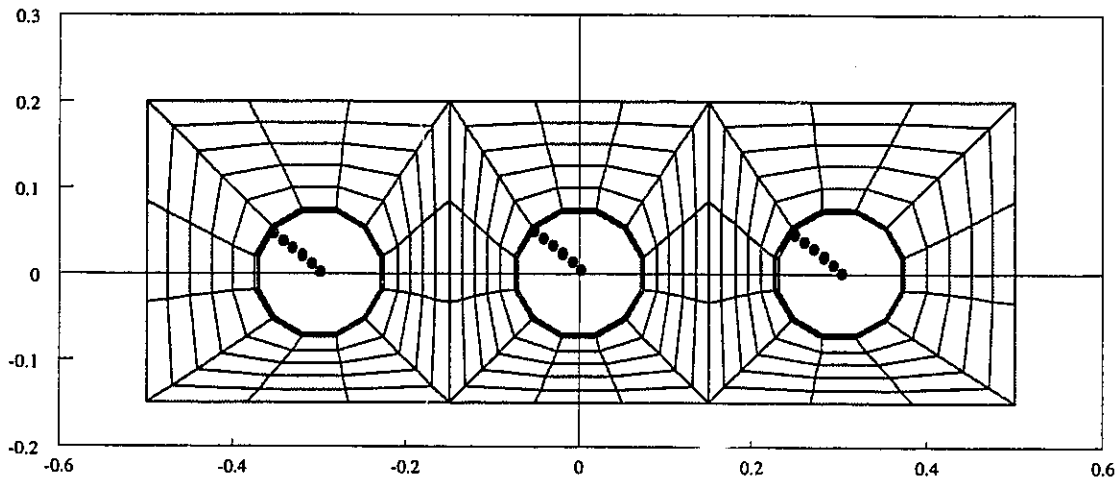


Figure 3.4 Finite element mesh: EFECAC approach

The same technique can be extended to cover the coupling between fully 3D and quasi 3D, i.e., 2D axisymmetric domains. This technique can be used to analyze the thermal behavior of buried cable splices (joining two cable lengths) which have similar construction as the cables, but with a larger outside diameter. This leads to an axial heat exchange between the splice and the adjacent portion of the cable, in addition to the regular radial heat exchange. Inside the splice, the heat dissipation is quasi 3D whereas outside, in the ground, the heat flow is fully 3D.

		EFEAC method	Conventional method
number of nodes (algebraic equations)		271	928
number of elements		276	900
effective matrix bandwidth		15	37
execution time for the transient analysis on fig. 3-5, Compaq 486/33L		70 sec.	432 sec.
Steady-state results			
phase a	conductor temp. (°C)	74.2	74.2
	sheath temp. (°C)	47.0	47.1
	cable surf. temp. (°C)	43.4	43.6
phase b	conductor temp. (°C)	86.0	86.3
	sheath temp. (°C)	57.4	58.2
	cable surf. temp. (°C)	52.2	53.1
phase c	conductor temp. (°C)	75.3	74.9
	sheath temp. (°C)	47.5	47.7
	cable surf. temp. (°C)	43.8	44.1

Table 3.1 Comparison between the conventional Full-Mesh Approach and the EFEAC technique

Another practical application is the case where a high voltage DC cable is partly buried and partly exposed to cold ambient air. At the interface between the buried and the exposed sections of the cable, a strong variation in the radial temperature gradient across the dielectric layer is likely to occur. This increase needs to be calculated and monitored accurately due to its large effect on the electric field distribution, that can ultimately damage the cable. In fact, one of the most important specifications of high voltage DC cables is the maximum allowable temperature gradient across the dielectric layer. The analysis of such an interface has to include the 3D domain where the cable is buried and the 2D axisymmetric domain, being the cable itself. The link between the two domains,

accomplished by using the present approach, is illustrated in figure 3.6. Obviously, in this case, one is dealing with a three-dimensional transitional element, namely: the EFGHE'F'G'H' element.

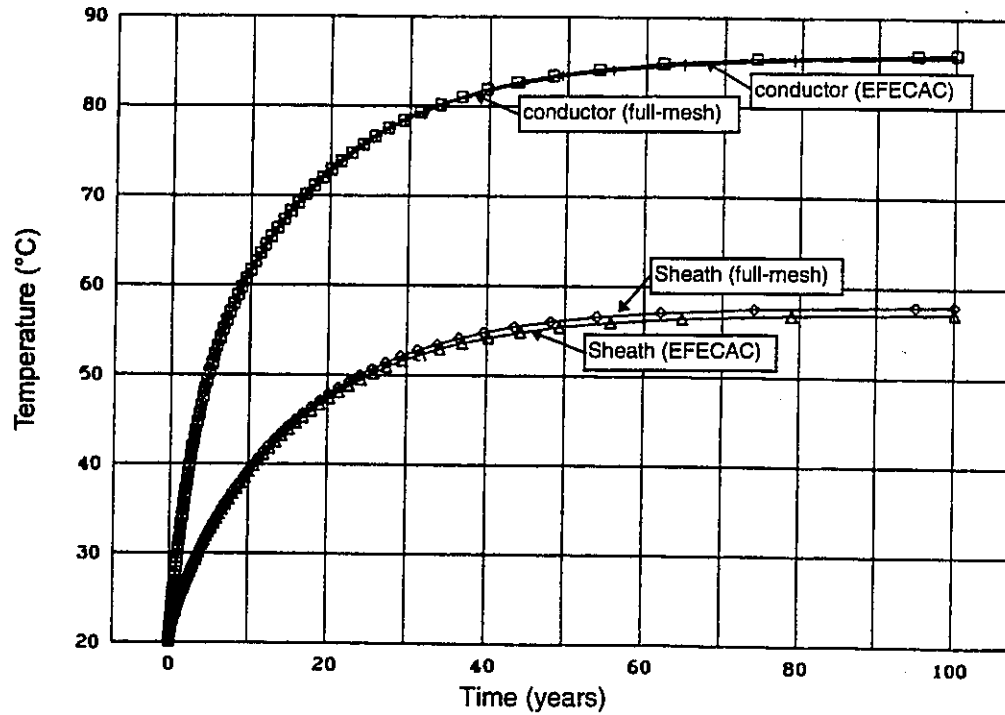


Figure 3.5 Comparison between the Full-Mesh Approach and the EFECAC approach (transient analysis, middle cable)

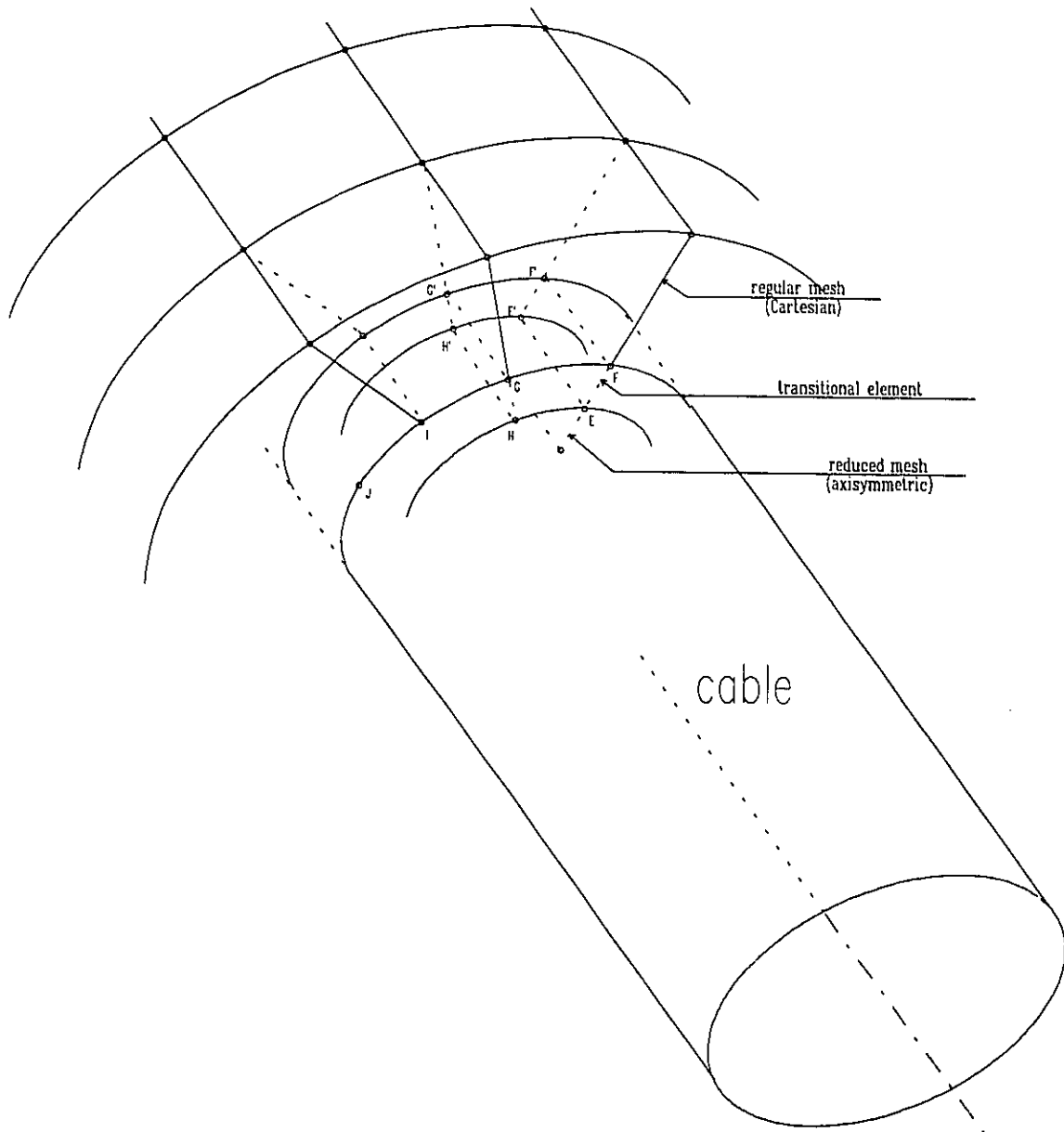


Figure 2.6 EFECAC approach applied to 3D finite element mesh

4. Industrial Applications

Based on the theoretical developments presented in the previous chapters, we have developed a series of finite element codes to analyze conventional and non conventional cable installations on personal computers [23, 24, 25]. Graphical interface techniques were adopted to facilitate the work of the user.

The main features of the computer package can be summarized as follows:

- capability of handling permanent, cyclic and transient load analyses in AC or DC;
- capability of handling empty ducts;
- natural or forced water cooling;
- automatic mesh generation.

All these options are accomplished in a user-friendly manner.

The main program offers a menu to choose between the following options:

- cables in trough under the floor of a deeply buried tunnel; with or without forced water cooling, one or two lateral water pipes for each cable;
- cables installed on tray inside a tunnel;
- cables directly buried close to the ground surface, with the option of single or double lateral water cooling;
- cables exposed to ambient air and sun, naked or inside a duct;
- cables in multiple rows duct bank with empty ducts.

4.1 Cables in Troughs and in a Tunnel

This series of codes deals specifically with high voltage and large size cables used generally in transmitting large quantities of power. It can analyze underground installations with cables directly buried under the floor of a deep tunnel or cables in concrete troughs buried a few meters below the ground surface. The mesh generation of both types of installations is accomplished by the program **MESHEC14**. This program discretizes the Cartesian 2D domain outside the cables, together with the 1D axisymmetric domain inside the cables according to the procedure described in the previous chapter.

The transient thermal analysis is performed by the program **TRATRA02**. In contrast to steady-state analysis, especially in the case of a deeply buried tunnel, the transient analysis of such installations requires a considerable number of time steps to obtain meaningful results. In fact, the user has to carry out the analysis for a very long period of time in order to reach the steady-state condition which is, usually, one month in the case of shallow installations and up to 40 years in deeply buried tunnel. This is mainly due to the large thermal mass of the surrounding rock and soil.

The boundaries below and at both sides of a deep tunnel installation are considered at a constant temperature, equal to the undisturbed soil temperature. This value is identical to the well water temperature which is a characteristic of the geographic site itself ($= 9^{\circ}\text{C}$ in the Montréal region). These boundaries are imposed at a sufficient distance (D_{trans}) far away from the installation (up to 200 m) in order to prevent any effect on the evolution of

cable temperature or to avoid creating any temperature gradient along the boundaries by the heat wave emanating from the cables during the long term finite element analysis. The program **MESHEC14** specifies the position of these boundaries in terms of the desired time duration of the analysis and the thermal diffusivity of the surrounding solid medium, using the following empirical equations:

$$D_{trans} = D_{perm} \left[3.835 - 0.00706 \cdot \alpha^* \right] + 0.1374 \cdot \alpha^* - 8.968 \quad (4.1)$$

where:

$$D_{perm} = \left[3.84659 + (7492.77\sqrt{\alpha} - 0.32408) \cdot t \right] \cdot \frac{\sqrt{\pi}}{2} \quad (4.2)$$

$$\alpha^* = \frac{36 \cdot \alpha}{12.51 \cdot 10^{-7}} \quad (4.3)$$

α is the thermal diffusivity (m^2/s), t is time duration of the analysis (year).

These empirical equations were established by carrying out hundreds of analyses with various types of rock and soil and at different time duration. In each analysis, the location of the constant temperature boundary (D_{trans}) condition was moved gradually outward far from the cable installation until no effect was detected on the cable's temperature and no gradient was established along these boundaries. This meant that any further increase in the distance separating the cables from the boundaries beyond the location calculated by equation (4.1) will have no effect on the outcome of the analysis. Obviously, the further

the boundary locations, the larger the mesh size, and consequently, the longer is the analysis time.

To speed up the analysis of such cable installations, we have developed a steady-state version. Our goal was to get a fast but more or less accurate figure of the expected cable behavior after years of operation without going through the more complicated transient analysis. In this approximate approach, the locations of the constant temperature boundary condition cannot be well defined physically, because, in practice, the steady-state may never be reached during the expected lifetime of the installation. A fictitious boundary can however be imposed at a precise distance (D_{perm}) (figure 4.1) from the cable in such a way that the steady-state analysis and the corresponding transient analysis would both give the same temperature distribution in the cables. This distance is calculated in terms of the surrounding soil thermal diffusivity and the desired time of the analysis as described in the previous empirical equation (4.2).

Several steady-state programs have been developed during this research program. Each one deals with some specific applications, namely:

TUNFLO01: This program calculates the cable's temperature and the air temperature inside the tunnel in the case where no artificial means are used to control the inside air temperature. This means that the air temperature increases steadily as the cables' temperature increases in time during the months and years of operation. The evolution of

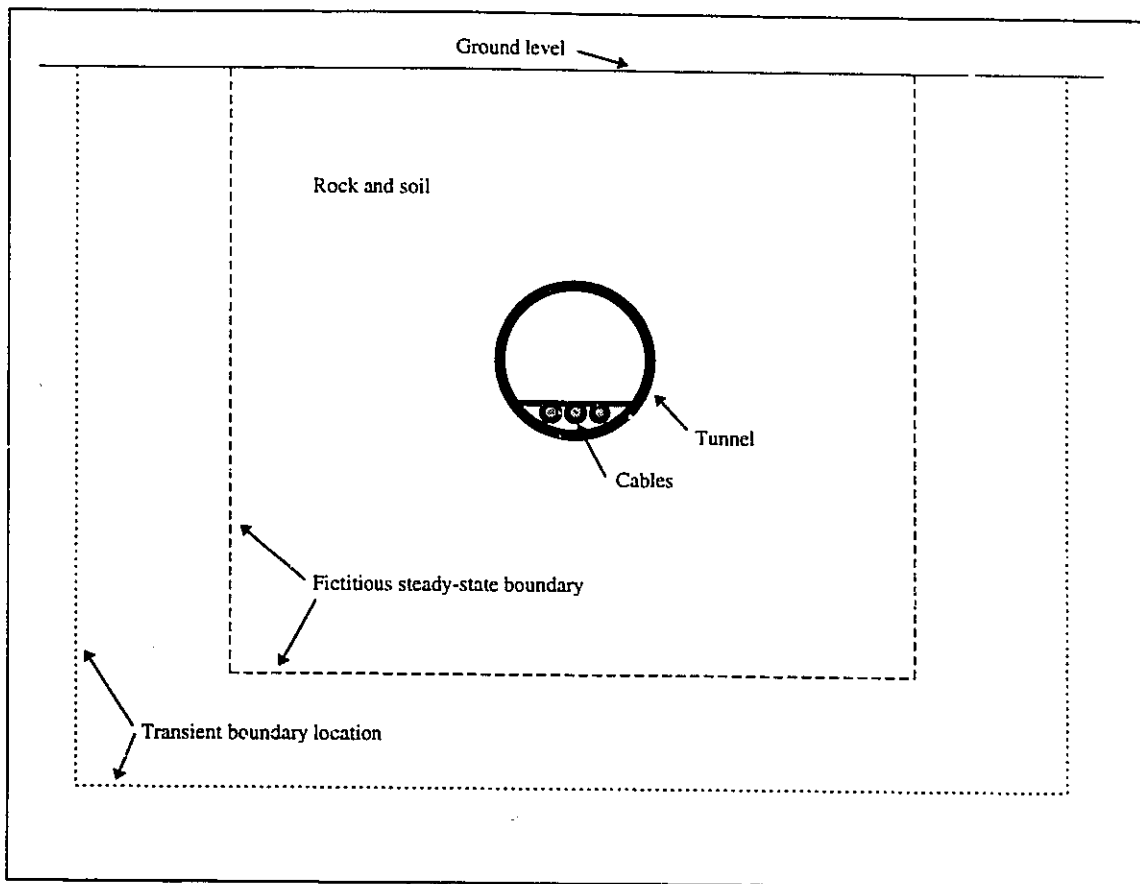


Figure 4.1 Constant temperature boundary locations in deep tunnel installation

air temperature inside the tunnel is crucial because, in many cases, this temperature is likely to be the factor that limits the capacity of such underground installations even though the cable temperature is far from reaching its maximum permissible value. In fact, in many countries, the electrical utilities are required not to exceed certain temperature limits (30 to 40°C) in work space for personal comfort and safety reasons.

TUNIMP01: This program deals with similar installations as those analyzed with the TUNFLO01, except that the air temperature inside the tunnel is controlled by forced air

or water cooling. This is usually the case of crowded overloaded installations where the air temperature under natural heat dissipation conditions would reach unacceptable levels and would otherwise limit their power transmission capacity.

ENFOUI01: This program is dedicated to analyze directly buried cable installations at low depths ranging between 1 and 2 m. At this depth, the time required to reach a quasi-steady-state is approximately one month. In this type of installations, the varying seasons of the year greatly affects the outcome of the analysis. The constant temperature boundary conditions below and at both sides of a such installation play a less critical role than in the case of deep tunnels. This is mainly due to the fact that the heat in shallow installations is mostly evacuated by convection and radiation through the ground surface, whereas in deep installations, the heat is completely absorbed by the large thermal mass of surrounding rock and soil.

The locations of the constant temperature boundaries in shallow installations were established based on experience. They are set at 6 m for steady-state analyses and at 10 m for transient analyses. The soil temperature distribution along these boundaries is a function of the season and the geographic location of the site. For example, in the metropolitan area of Montreal, the following empirical equation is used to express the soil temperature (T_s) as a function of the month of the year (M) and the depth (h):

$$T_s = 9 + 11.5 \cdot \exp^{-0.37h} \sin[30(M + 4) - 15.72 - 21.3 \cdot h] \quad (4.4)$$

This equation is based on statistical observations with time and can be applied to any region in Quebec by simply replacing the number 9 by the prevailing well water temperature at the geographic location. Values for this temperature are found in standard handbooks.

The introduced package of programs was applied successfully to predict the thermal behavior of the world's first 500 kV DC cable designed for the St. Lawrence river crossing at Grondines between Québec city and Montréal (figure 4.2). In the land section of the crossing (1.1 km long), the cables are installed in a precast concrete trough 0.7 m deep below the ground level (figure 4.3). In the tunnel section, the cables are laid down under the floor and covered by weak-mix concrete (see figure 1.3). The tunnel is 4.1 km long, 40 m deep and has an internal diameter of 3.4 m.

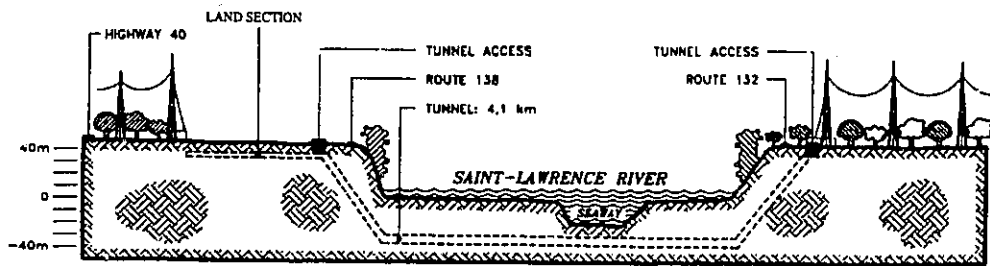


Figure 4.2 Longitudinal profile of the St. Lawrence river crossing

The thermal studies [26], conducted at the planning stage of the project, played a major role in the cable design and installation. According to Hydro Québec's specifications, the air temperature inside the tunnel must not exceed 40°C after 40 years' continuous operation, without artificial cooling or forced ventilation. To satisfy these requirements, a preliminary thermal analysis of the tunnel and the land sections was conducted with

various cable designs. Figure 4.4 shows part of the finite element mesh of the 500 kV DC cable installation under the floor of the tunnel. The mesh extends to approximately 100 m below and on both sides of the tunnel to accommodate the long-term transient analysis. A constant temperature was imposed at these boundaries equal to the local well temperature. This temperature is equal to 9°C along the St. Lawrence river.

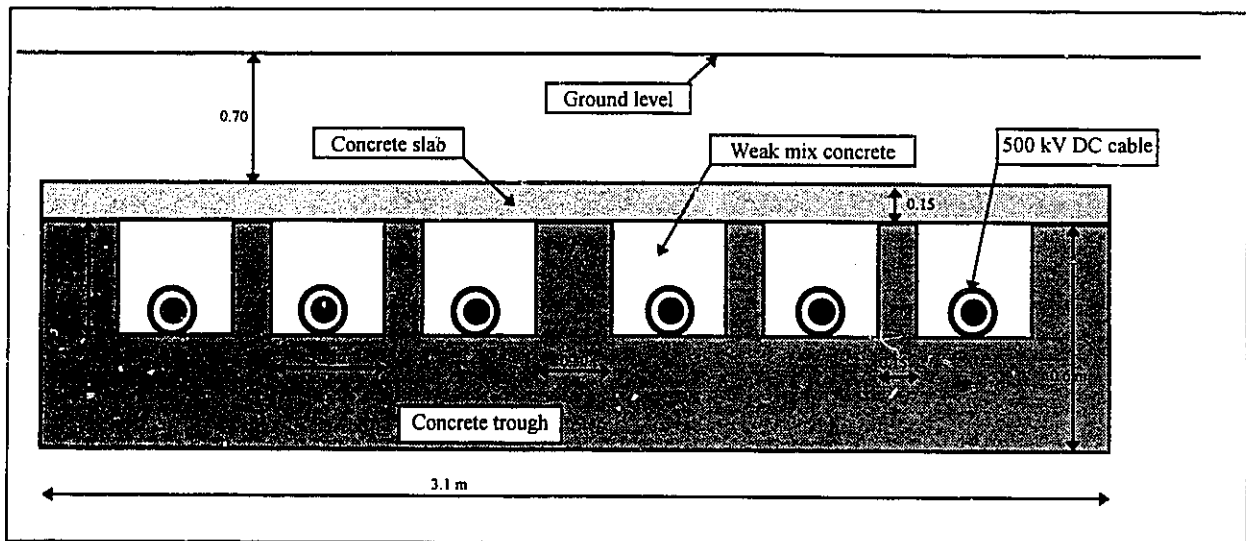


Figure 4.3 Typical cross-section of the land part of the St. Lawrence crossing

Figure 4.5 shows the calculated transient temperature variation of the cable and the air inside the tunnel when four of the cables are energized at 1450 Amp per cable between November and February and 1125 Amp per cable for the remaining months of the year.

Figure 4.6 shows a part of the finite element mesh of the land section in the installation. The cables in this section are subjected to the same load pattern as in the tunnel.

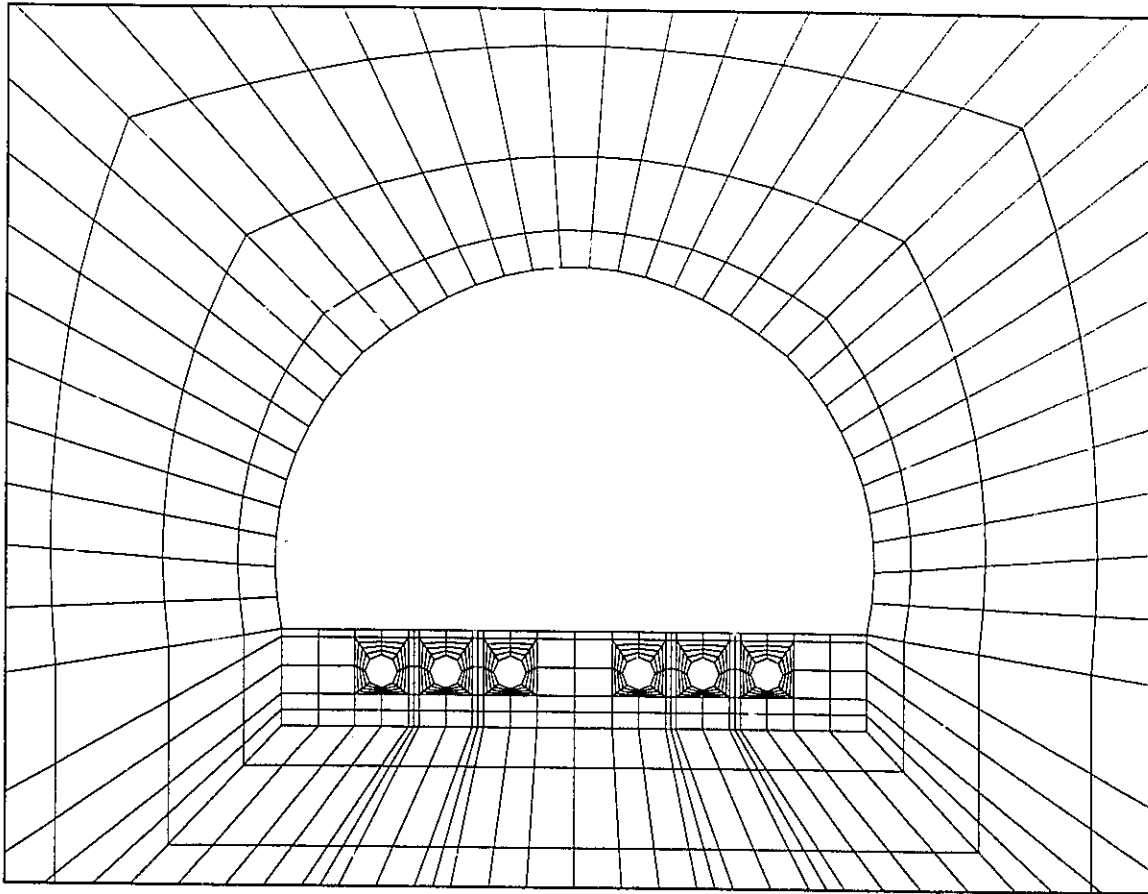


Figure 4.4 Finite element mesh of the St. Lawrence river crossing (tunnel section)

Figure 4.7 shows the load and the predicted temperature variation of the hottest cable in the land section. It can be seen that the cable temperature in both configurations remains well below the maximum specified value of 85°C specified by the manufacturer. The critical parameter that led to the choice of a larger cable size (1400 mm²) than needed was the tunnel air temperature that increases steadily over the years, approaching the maximum imposed limit of 40°C.

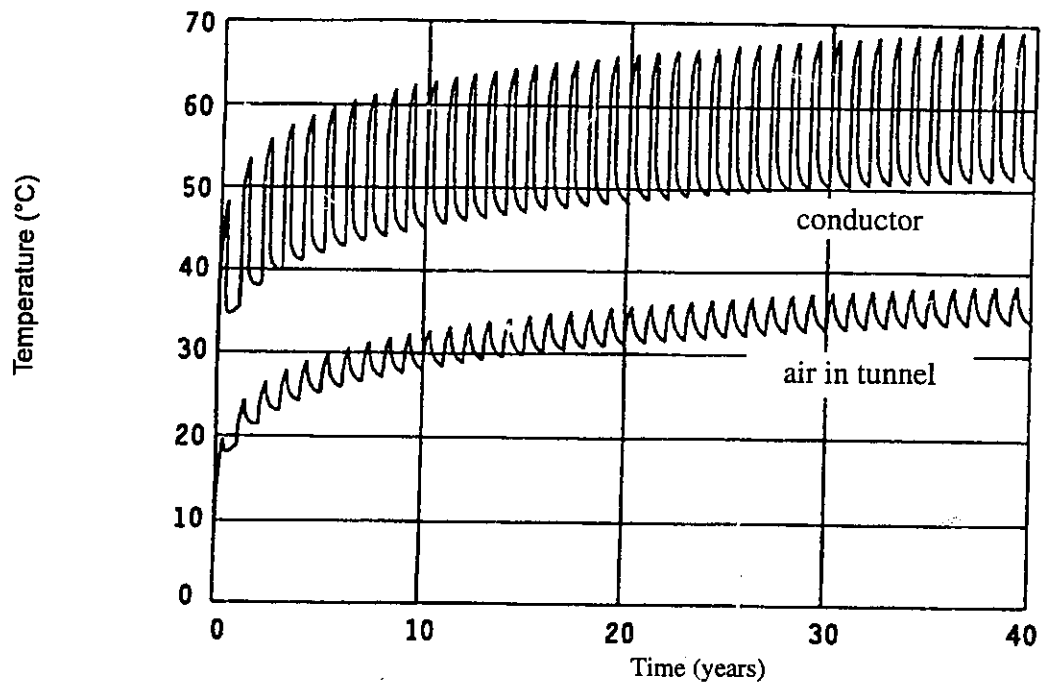


Figure 4.5 Expected air and hottest cable temperature variations inside the tunnel

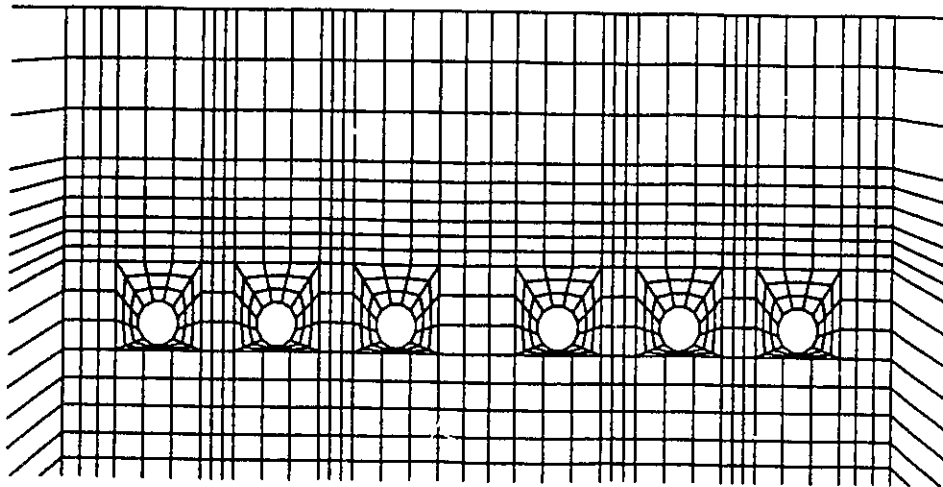


Figure 4.6 Finite element mesh of the St. Lawrence river crossing (land part)

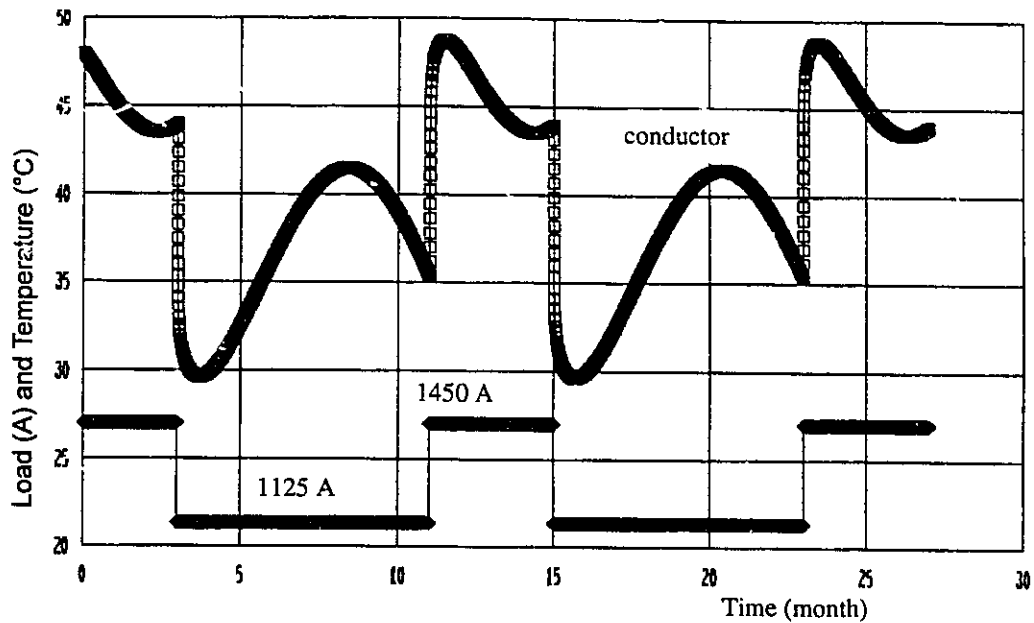


Figure 4.7 Expected hottest cable temperature variation in the land part of the crossing

In the above analysis, the empty space inside the tunnel is considered as a large cavity where part of the heat generated in the cables is dissipated by combined free convection, radiation and conduction. The analysis is simplified according to the conclusions of chapter 2. It was carried out as follows: At each time step, an average ambient temperature in the tunnel space is considered. This temperature is calculated by averaging the wall surface temperature of the tunnel. An equivalent heat transfer coefficient at the wall-air interfaces is used according to ASHRAE recommendations for dwelling heat loss calculations [27]. This value ranges between 6 and 10 W/m²°C depending on the wall inclination and the heat exchange direction. A sensitivity analysis conducted to examine the effect of these two extremes had shown little effect on cable temperature or on air temperature inside the tunnel.

In the case of similar river crossings, planned by Hydro Québec in the future, with four 735 kV AC cables, to carry out a load of 1500 A each (1 cable is on standby), the artificial cooling is likely to be necessary due to the high dielectric and sheath losses generated inside this type of cables. Our finite element program allows the user to analyze such installations with ease. The mesh of some of the proposed configurations inside a tunnel with one and two lateral water cooling is shown in figures 4.8 and 4.9.

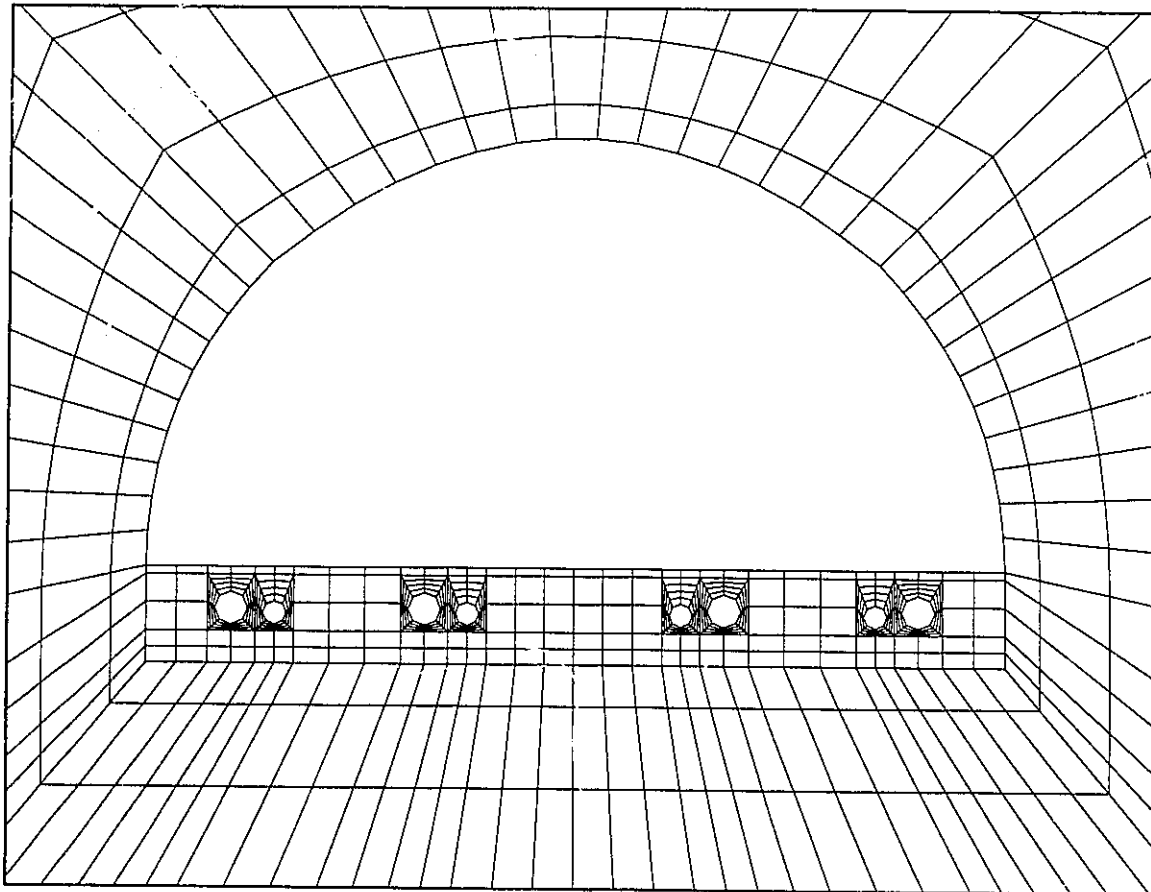


Figure 4.8 Finite element mesh of a tunnel installation with one lateral water pipe cooling

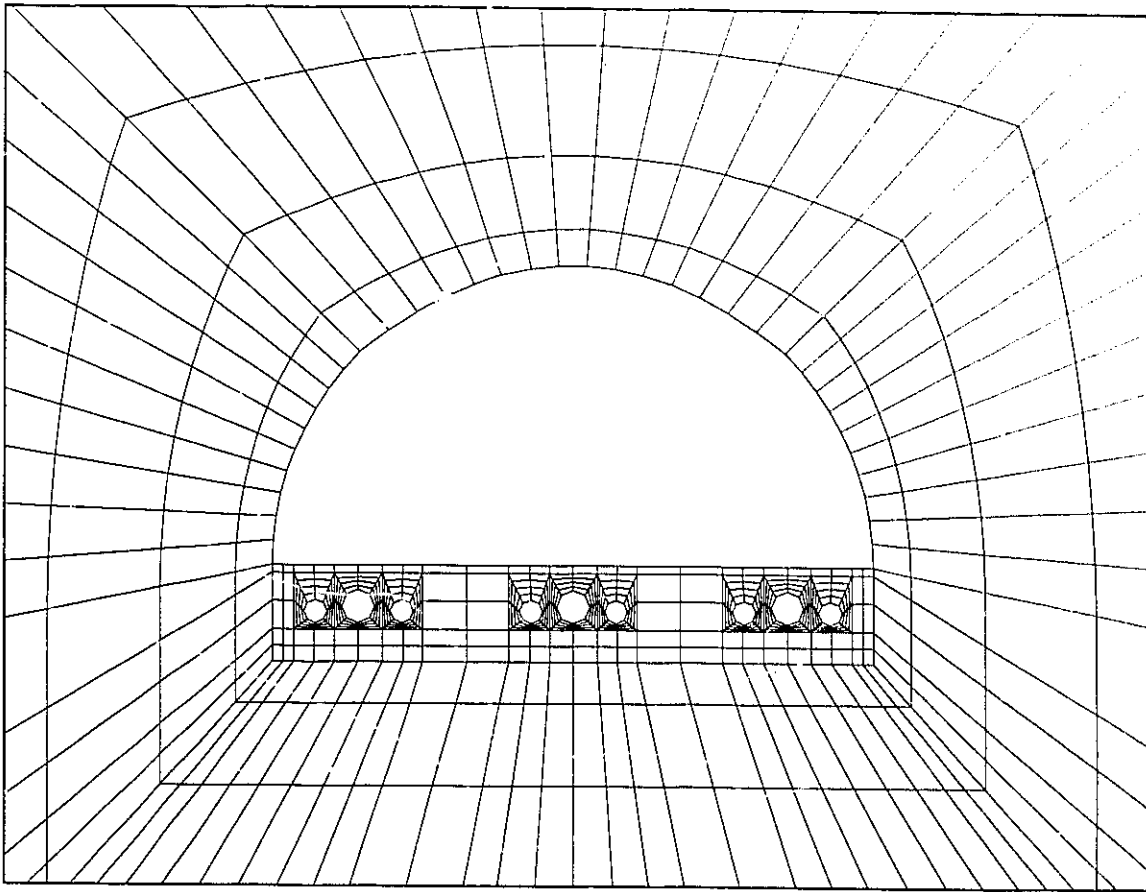


Figure 4.9 Finite element mesh of a tunnel installation with two lateral water pipes cooling

Figures 4.10 and 4.11 show the prediction of the temperature rise of the hottest cable and the air inside the tunnel after 2 years of operation, with and without forced cooling. It can be seen that, without forced cooling, the air temperature could reach an unacceptable high level after a few months of continuous operation. In the case of one-pipe forced cooling (water at 20°C), all cables and air temperatures inside the tunnel remain well below the maximum specified limits of 85°C and 30°C, respectively.

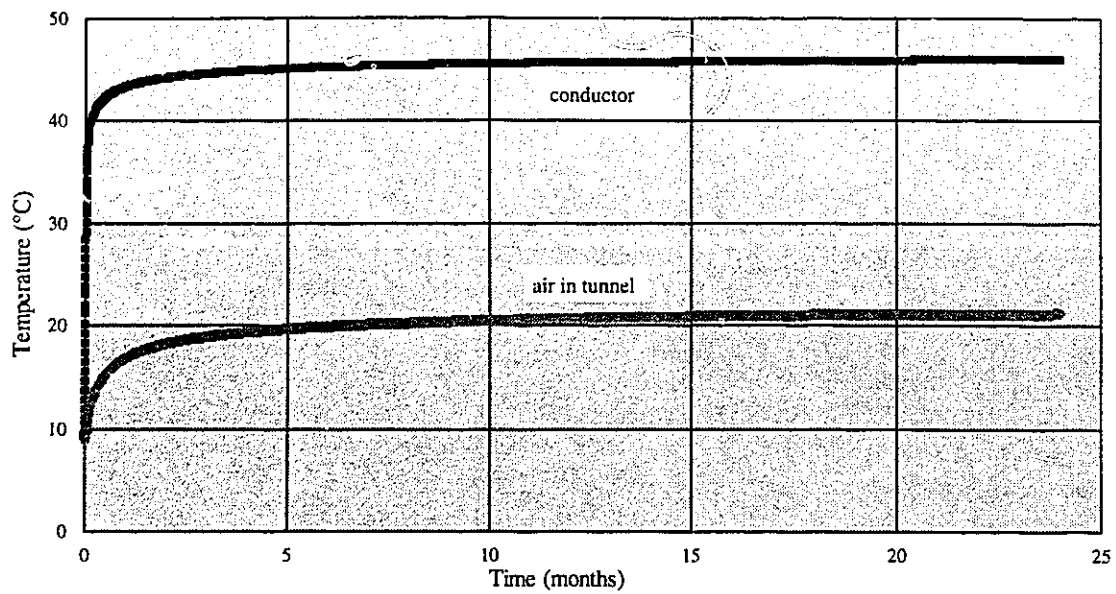


Figure 4.10 Expected cable and air temperatures variation inside the tunnel:
forced cooling

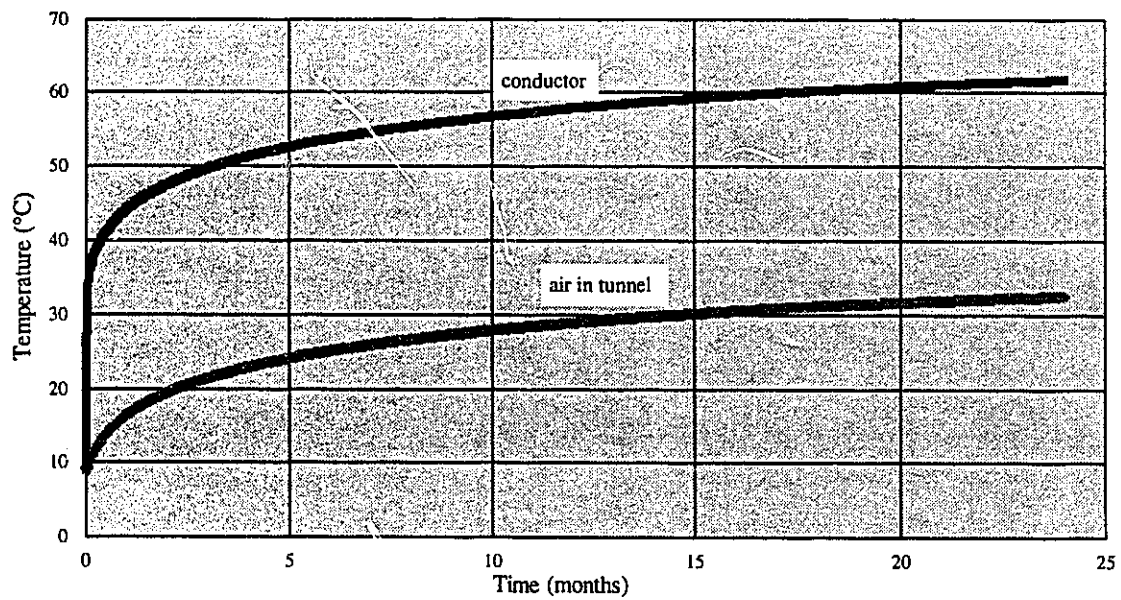


Figure 4.11 Expected cable and air temperatures variation inside the tunnel:
natural cooling

4.2 Cables Inside the Air Space of a Tunnel

This package of programs performs the thermal analysis of cables located on racks, solidly anchored to a tunnel wall. This is a widely used configuration by the utilities because it is cheap and simple to install; however, it does not provide any protection to the maintenance personnel in case of a short circuit.

Due to the relatively large size of the tunnel compared to the size of the inside cables, this type of installation may be considered equivalent to the case of cables installed in an infinite medium. One part of the heat is exchanged between the cables and the tunnel wall by radiation. The other part is dissipated by natural convection via the air medium as illustrated in figure 4.12.

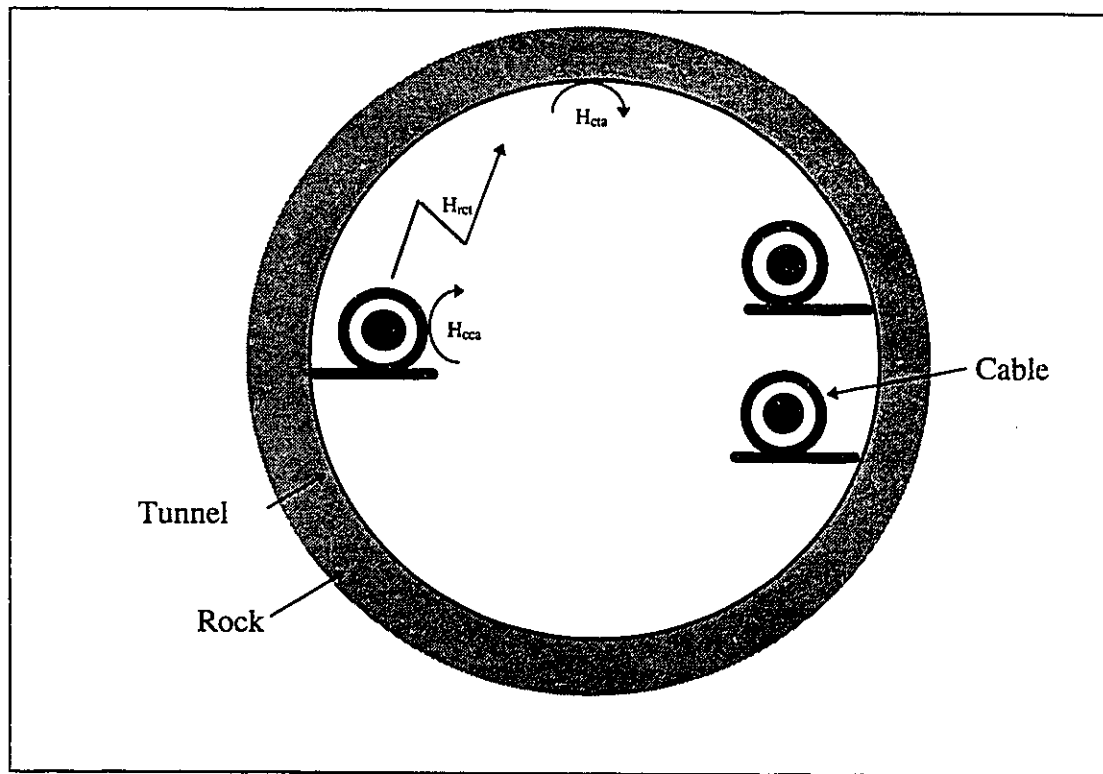


Figure 4.12 Typical cable installation inside the air space of a tunnel

The linearized radiation heat transfer coefficient (H_{rct}) and the convection heat transfer coefficient (H_{cca}) are calculated by the following standard equations [15]:

$$H_{rct} = 5.6693 \cdot 10^{-8} \cdot \varepsilon \cdot [(T_{kc}^2 + T_{kt}^2) * (T_{kc} + T_{kt})] \quad (4.5)$$

$$H_{cca} = \left[0.53 \cdot Ra^{0.25} \right] \frac{k_a}{D_c} \quad \text{for } 10^4 < Ra_D < 10^9 \quad (4.6)$$

$$H_{cca} = \left[0.13 \cdot Ra^{0.333} \right] \frac{k_a}{D_c} \quad \text{for } 10^9 < Ra_D < 10^{12} \quad (4.7)$$

where D_c is the cable diameter (m), k_a is the air thermal conductivity (W/m°C) and Ra is the Rayleigh number, ε is the surface emissivity, T_{kc} and T_{kt} are the cable and tunnel temperatures (°K), respectively.

The equivalent thermal resistance (R_{eq}) between the cables and the tunnel wall is calculated by assuming that the radiation and convection heat exchanges are acting in parallel. This resistance is calculated as follow:

$$\frac{1}{R_{eq}} = \frac{1}{\left(\frac{1}{\pi D_c H_{cca}} + \frac{1}{\pi D_t H_{cta}} \right)} + \frac{1}{\left(\frac{1}{\pi D_c H_{rct}} \right)} \quad (4.8)$$

where D_t is the tunnel diameter (m) and H_{cta} is the convection heat transfer coefficient between the air and the tunnel wall (W/m°C).

The automatic mesh generation in this package is accomplished by the program **MESHTUN**. The transient analysis is done using **FEMTTUN1** and the steady-state results are obtained by the program **FEMPTUN**. The locations of the constant temperature boundaries are determined in the same way as the other types of tunnel installations discussed in section 4.1.

4.3 Aboveground Cables Exposed to the Elements

This is the most simple cable installation encountered in transmission and distribution networks. In any underground cable installation, a part of the circuit along the cable route is normally exposed to ambient air and to the sun. The absence of solid medium around the cables in this case makes the mesh generation quite simple. This procedure is accomplished within the main programs **FEMPAIR1** and **FEMTAIR1** that analyze the thermal behavior in steady-state and in the transient regime, respectively.

The heat transfer coefficient at the cable surface is calculated using equations (4.5) to (4.7) by replacing the tunnel temperature by the ambient temperature.

The sun effect is accounted for by considering the worst case in which the configuration cable/sun produces the maximum heat gain during the day. This is the condition when the sun radiation strikes directly the cable surface at zero angle of incidence.

The maximum solar radiation intensity outside the atmosphere is equal to 1353 W/m^2 . At sea level, in the industrialized countries, this value decreases to about 900 W/m^2 . The drop is caused mainly by atmospheric pollution and by water vapor.

One part of the solar radiation striking the cable surface is reflected, and the remaining part is absorbed in the form of heat. The latter component depends on the absorbtivity of the cable surface materiel, which normally varies between 0.9 and 0.99. Due to the cylindrical shape of the cable, the effective component of the striking solar radiation varies between zero and its maximum level along the half surface of the cable (figure 4.13). The net heat gain is calculated as follows:

$$Q_s = \gamma \int_{-\frac{\pi}{2}}^{\frac{\pi}{2}} q_n \cdot \cos \beta \cdot r \cdot d\beta = 2r \cdot \gamma \cdot q_n \quad (4.9)$$

Despite the fact that only half of the cable is exposed to the sun, we have considered, for the sake of simplification, the solar heat gain by the cable (q_s) as uniformly distributed along its entire surface. This value can be calculated by the following equation:

$$q_s = \frac{Q_s}{2\pi r} = \gamma \frac{q_n}{\pi} \quad (4.10)$$

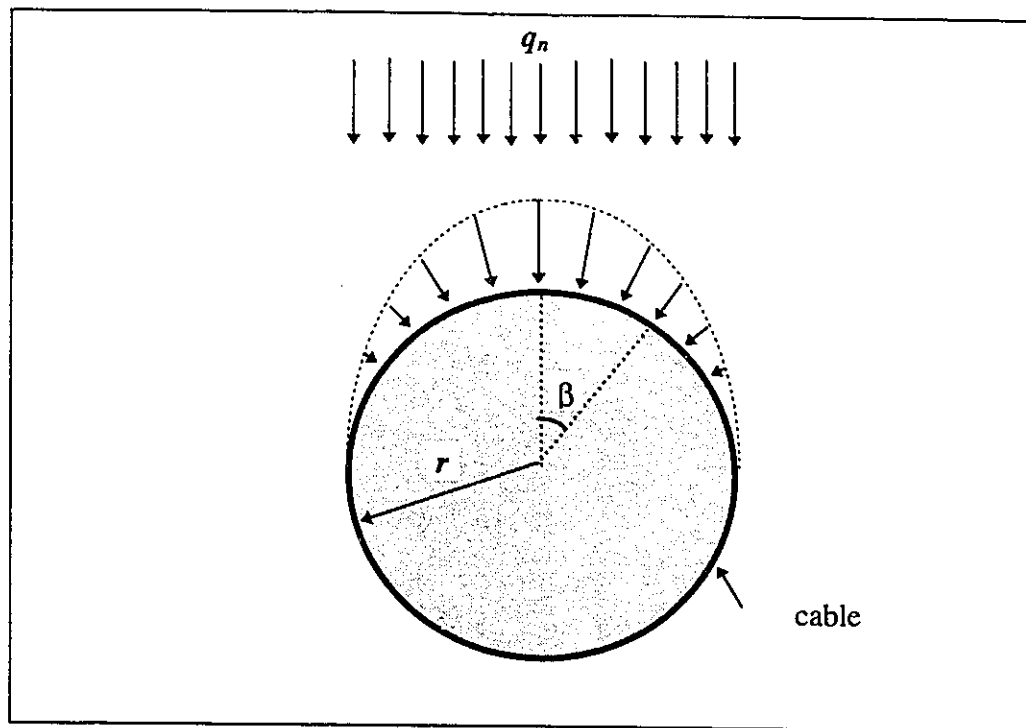


Figure 4.13 Effective solar heat flux striking the cable surface

4.4 Cables in Duct Banks

This type of installations in multiple rows and columns (figure 1.1) is the most commonly found in underground networks. It is usually dedicated to low and medium voltage (120 V to 33 kV) distribution cables, and occasionally to high voltage large size cables. In these installations, the cables are usually located inside the ducts which are embedded in concrete, and occasionally, in directly buried configurations.

The high voltage package includes the mesh generation program **MASMESH2**, and **MASPERM3** and **MASTRAN1** programs dedicated to steady-state and transient analyses, respectively. This package is also restricted to the one cable per duct case.

The second package is dedicated to the analysis of distribution duct banks. The cables used are usually smaller in size and rated at lower voltage compared to the previous applications. These are the type of cables running under city streets that distribute the electricity to individual houses and businesses. In these installations, the cables are usually installed in PVC ducts arranged in multiple rows and columns. In the majority of cases, there is an equal number of ducts in each row and column. Sometimes, few ducts are added to an existing installation creating a non-symmetric duct bank. The mesh generation of a such complex installation is performed automatically without difficulties. In fact, the program allows the addition of several so called "missing ducts" ducts that have the available space but do not exist. An example of the finite element mesh of a non-symmetric duct bank is shown in figure 1.4. With the help of the present finite element developments, the data preparation, the mesh generation and the complete thermal analysis of such installations can be done within a few minutes. This package is identified by the name **MASSIF**. This is the most frequently used set of programs at Hydro-Québec for the cable ampacity analysis. We have started the development of these programs in early 1983 [28] and we kept improving them since then [25, 29]. This tool permits to design and load, at an optimum level, the future and existing underground installations. It permits also the analysis of any configuration encountered in distribution networks, namely: single phase medium voltage (4-33 kV), three-phase medium voltage,

low voltage cables at 347/600 V and 120/240 V. It can handle up to 4 different cables in one single duct. The induced current in such an installation is calculated by matrix manipulation of complex numbers. The resulting current is added vectorially to any other current in the neutral that is resulting from an unbalanced phase loading.

The most important feature of the finite element package MASSIF is its capability of analyzing the thermal behavior of complex duct banks in emergency overload situations. This represents, in reality, the most critical case in which one or several cables may reach or even exceed the maximum permissible temperature, leading eventually to failure and power blackout. The following example illustrates a standard overload analysis conducted on one configuration widely used at Hydro-Québec. It consists of a three by three symmetric duct bank with an empty middle duct (figure 4.14). The remaining ducts are populated with 3, 750 MCM (380 mm^2) cables each. The current level circulating in each cable varies throughout the day according to the load cycle shown in figure 4.15.

The nominal maximum current distribution that occurs around 6 o'clock in the afternoon is shown in table 4.1.

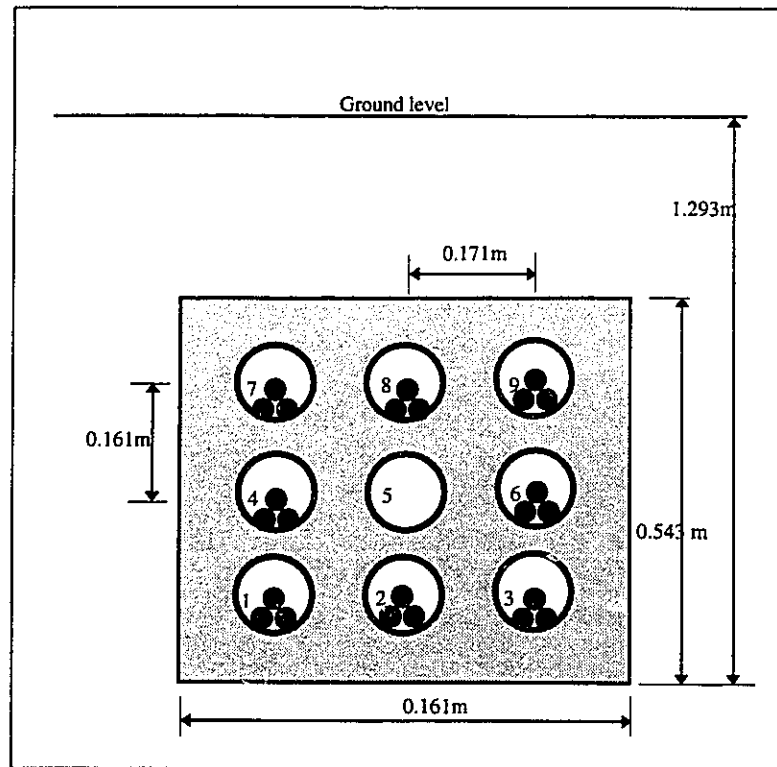


Figure 4.14 Typical symmetric distribution duct bank

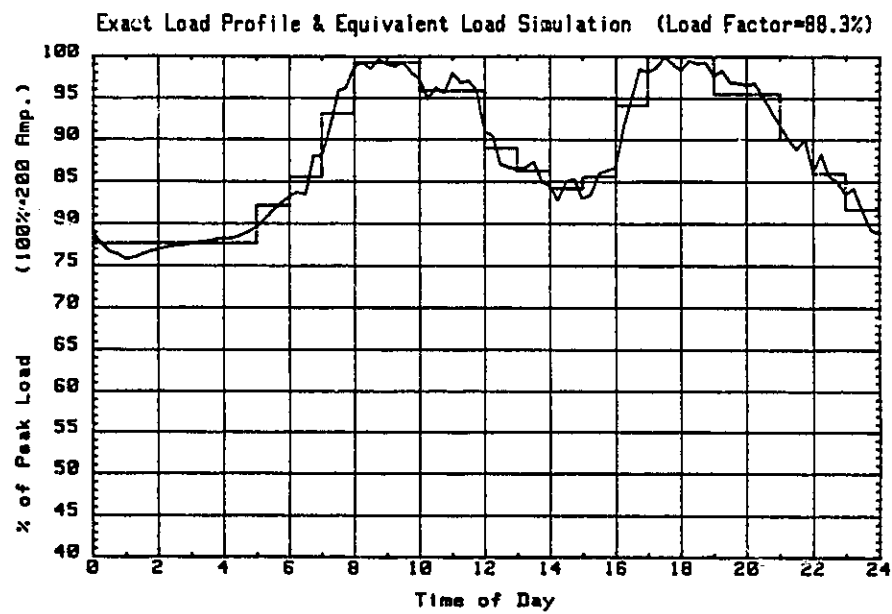


Figure 4.15 Typical residential daily load cycle at Hydro-Québec

DUCT #	PHASE A (Amp)	PHASE B (Amp)	PHASE C (Amp)	T-conductor (°C)
1	232	258	284	56.5
2	264	293	322	63.9
3	264	293	322	61.7
4	198	220	242	53.6
5	-----	-----	-----	-----
6	232	258	284	59.5
7	198	220	242	48.5
8	198	220	242	52.3
9	264	293	322	57.0

Table 4.1 Maximum nominal current distribution prior to emergency

The same table shows the maximum cable's temperature as calculated by the steady-state version of the finite element program. This analysis was carried out in December, which corresponds usually with the peak electric energy consumption in the province of Québec.

The emergency overload simulates a failure in circuit #9 at 2:00 P.M. The load which was carried by this circuit, is transferred equally to circuits #1, #2 and #3, three hours later. The analysis of such a case, including data preparation and mesh generation can be done in a few minutes, therefore allowing the operator to take a quick decision and appropriate measures concerning the optimum load redistribution during emergency situations since the analysis provides a reliable picture on cable's temperature rise in real time. Therefore, a dangerous temperature level can be avoided. Figure 4.16 shows the temperature variation of the hottest cable in each circuit involved in this emergency simulation.

The finite element analysis of duct bank installations similar to the one studied earlier, requires the finite element meshing of the air gaps between cables and ducts together with the remainder of the domain. Although heat is dissipated by combined convection, radiation and conduction through these regions, only conduction heat transfer is considered by using an equivalent heat conduction coefficient as was described in chapter 2. The empty duct is accounted for by considering a fictitious unloaded cable inside.

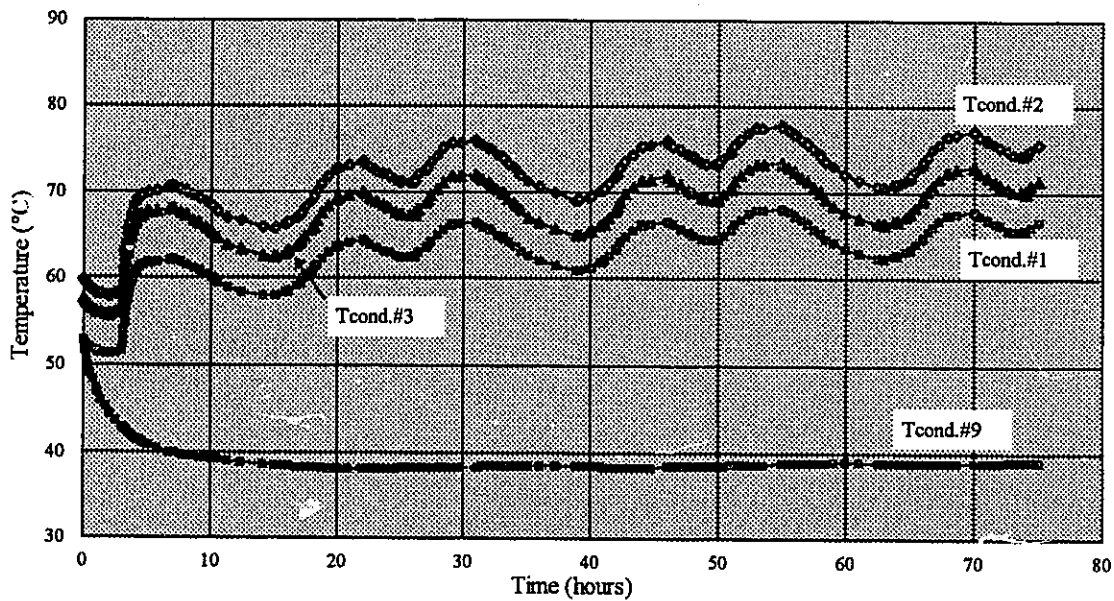


Figure 4.16 Temperature variation following an emergency overload

5. Experimental Verifications

The finite element package described in the previous chapter was verified experimentally in full-size installations and in laboratory environment. In the full-size field installations, the verification was restricted to transient regime only because steady-state conditions could not be reached due to the randomly changing weather conditions. Verification inside the laboratory covers both steady-state and transient regimes.

5.1 Verification in Full-Size Installations

During the past 10 years, we have conducted at IREQ several tests on large scale cable installations like the ones dedicated to power transmission. We have also examined experimentally the current carrying capacity of medium power installations at distribution level. These tests were requested by Hydro-Québec and by the Canadian Electrical Association and financed in part by IREQ's internal research activities in order to verify the present finite element developments related to cable ampacity calculations.

5.1.1 St. Lawrence River Crossing Project with 500 kV DC Cables

Within the framework of the world's first 500 kV DC project, IREQ has conducted a series of severe thermo-electro-mechanical tests on a small cable length in order to insure a long lasting safe operation of the installation. The first test (prototype test) was conducted inside a High Voltage Laboratory in which the cable was exposed to air. The

second (demonstration test) was done outside, where a large section of the cable was buried underground.

5.1.1.1 Prototype Test

The prototype-test protocol is presented in detail in references [26] and [30]. Briefly, a 20 m cable length was subjected to thermal cycling, which consists of heating the conductor of the cable up to 90°C in 5 hours and then maintaining this temperature during 3 hours before letting the cable cool down for the rest of the day (16 hours). Before the end of the heating period, the protocol requires that the temperature gradient across the dielectric layer of the cable (see figure 1.2) reaches its maximum permissible value in order to stress the cable up to its limit. A total of 50 thermal cycles were conducted in controlled environment, inside the IREQ's High Voltage laboratory.

A preliminary thermal analysis of the test loop (figure 5.1) had shown that internal heating, merely by circulating current through the conductor, is not sufficient to satisfy the test requirements. Consequently, auxiliary heating was applied on the outside surface of the cable. A thin copper tape was wound around the cable before installing the heating wire and the whole assembly was covered with a layer of thermal insulation. To simplify the control, the heating period was divided into 4 sub-periods (figure 5.2), each of these sub-periods was assigned a given constant circulating current and a constant

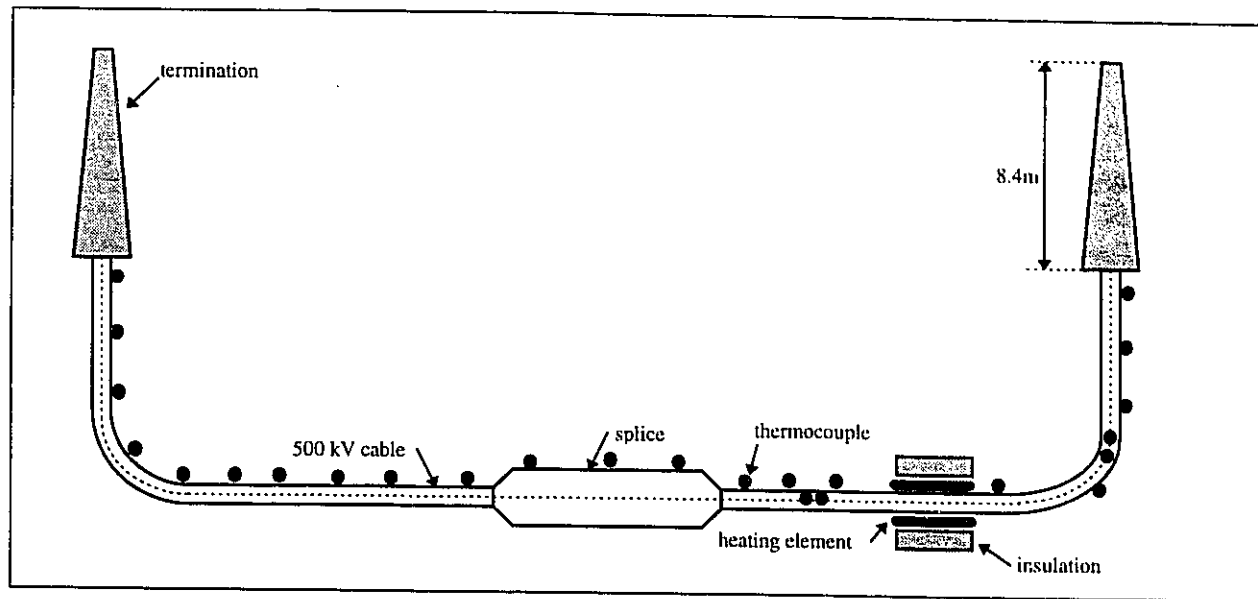


Figure 5.1 Test loop for the prototype test

auxiliary heating, based on the results of the preliminary analysis. The testing was carried on successfully for 30 cycles. A comparison between calculated and measured cable temperatures for one particular heating period is shown in figure 5.2.

5.1.1.2 Demonstration Test

For the demonstration test, a 130 m cable loop was installed outside in a concrete trough and covered by a weak mix concrete. A sketch of the test loop and the cable arrangement in the trough are shown in figures 5.3 and 5.4, respectively. More than 100 thermocouples and several thermal resistivity sensors were installed along and around the cable. The conductor temperature was also measured at different locations by inserting thermocouples through the oil channel. The thermocouples' signals were transmitted to the control room via an infrared beam.

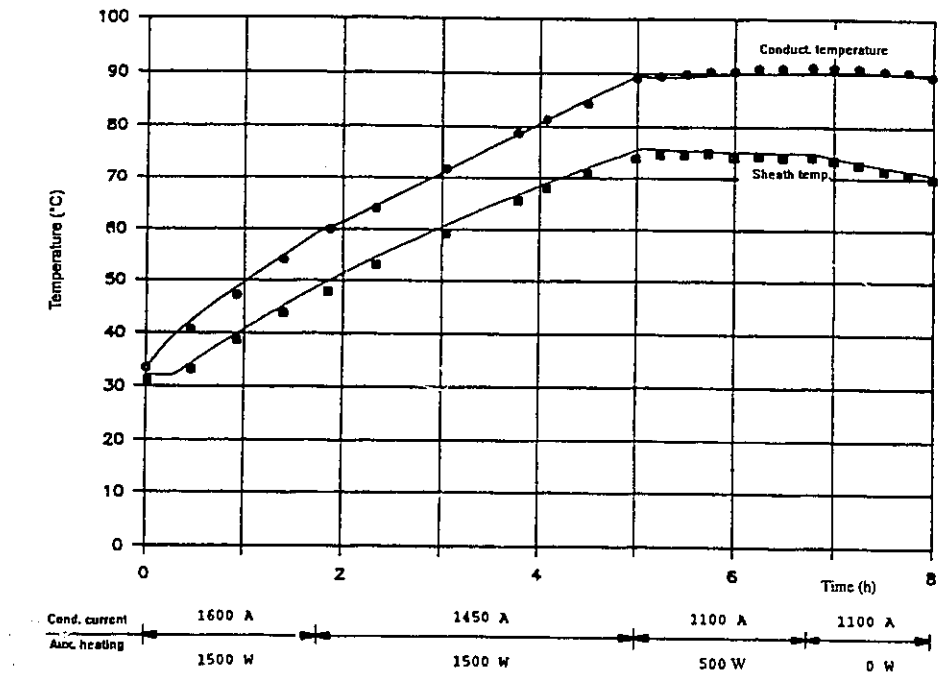


Figure 5.2 Prototype test: comparison between calculated and measured temperatures

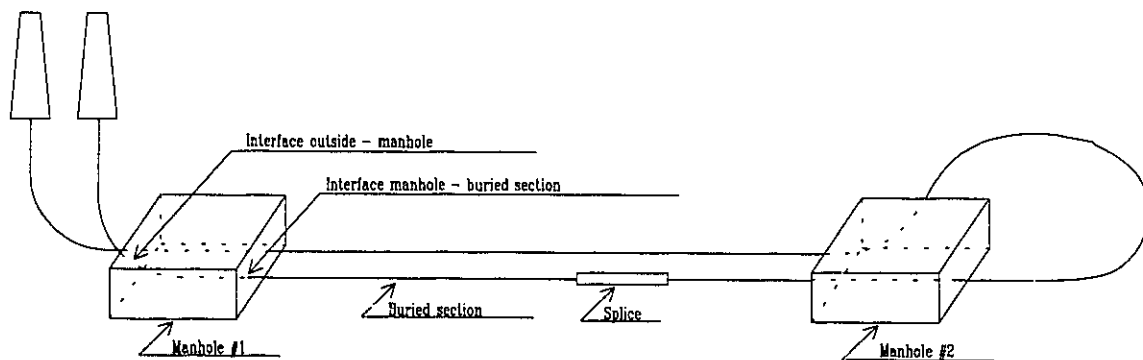


Figure 5.3 Test loop for the demonstration test

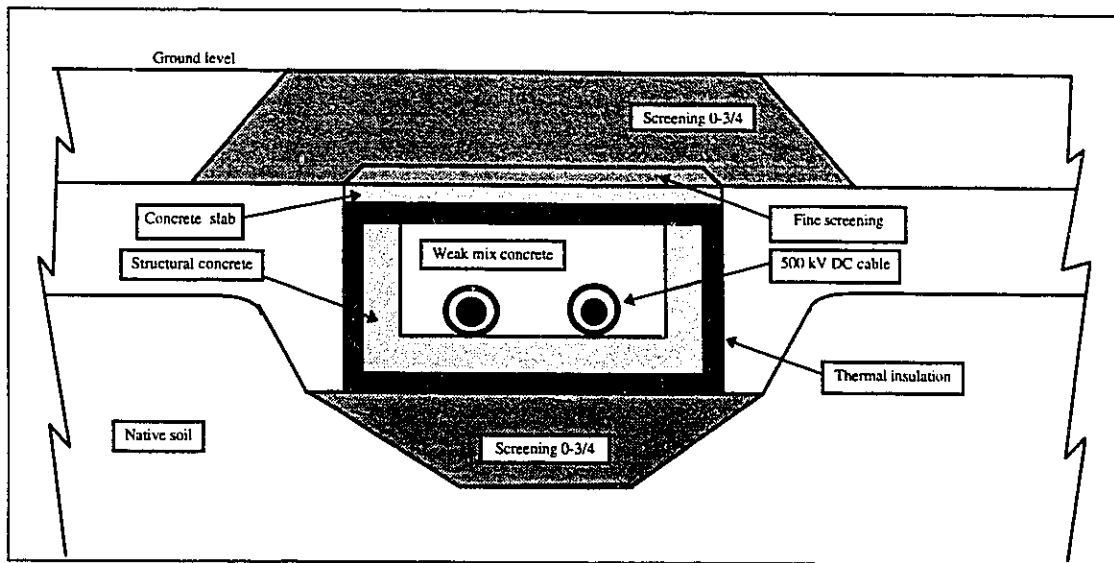


Figure 5.4 Typical cross-section in the demonstration test loop

Thermal cycling of the cable in the demonstration test differs from that applied in the prototype test. The heating and cooling periods are longer, due to the large thermal capacity of the backfill around the cable: six days were allowed to bring the conductor's temperature up to 90°C and one day for the cooling stage. Furthermore, for practical reasons, no auxiliary heating was applied on the outside surface of the cable. These reasons, together with the fact that the ambient temperature in Montréal changes significantly during the day and within each season, have made manual temperature control very tedious. Instead, a dedicated computer program was developed to conduct the testing automatically by modulating the current according to the desired pattern of temperature variation with time.

Prior to the construction of the test loop, a preliminary thermal analysis conducted by the finite element program (figure 5.5) had shown that, in order to carry out the test according to the specifications, a layer of 5 cm thermal insulation must be applied on the bottom and on the vertical walls of the concrete trough, and of 7.5 cm above the backfill of the weak mix concrete as shown in figure 5.4. The thickness of these layers was selected in terms of ensuring that a sufficiently high current can be circulated in the conductor to raise its temperature up to 90°C, and that the cable is stressed to its maximum limit by imposing the maximum permissible temperature gradient across the dielectric material.

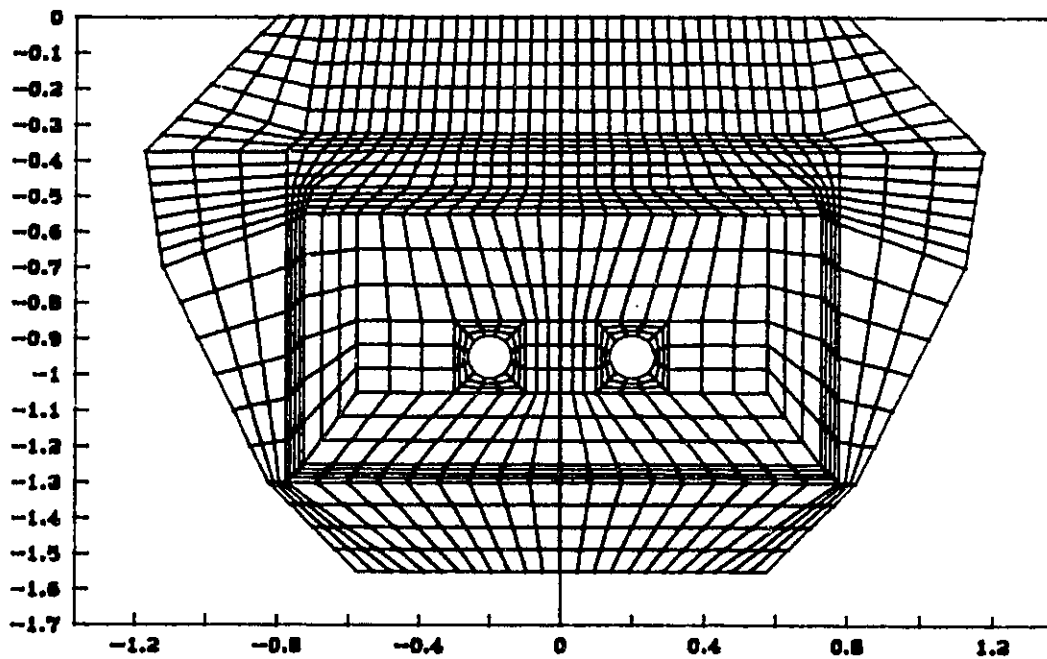


Figure 5.5 Finite element mesh of the trough

Figure 5.6 shows the history of load variation for a period of 2 consecutive cycles (14 days). For the sake of comparison, a numerical analysis, conducted prior to the experimentation at a slightly lower current level, exhibits good agreement with the measured data as shown in figure 5.7.

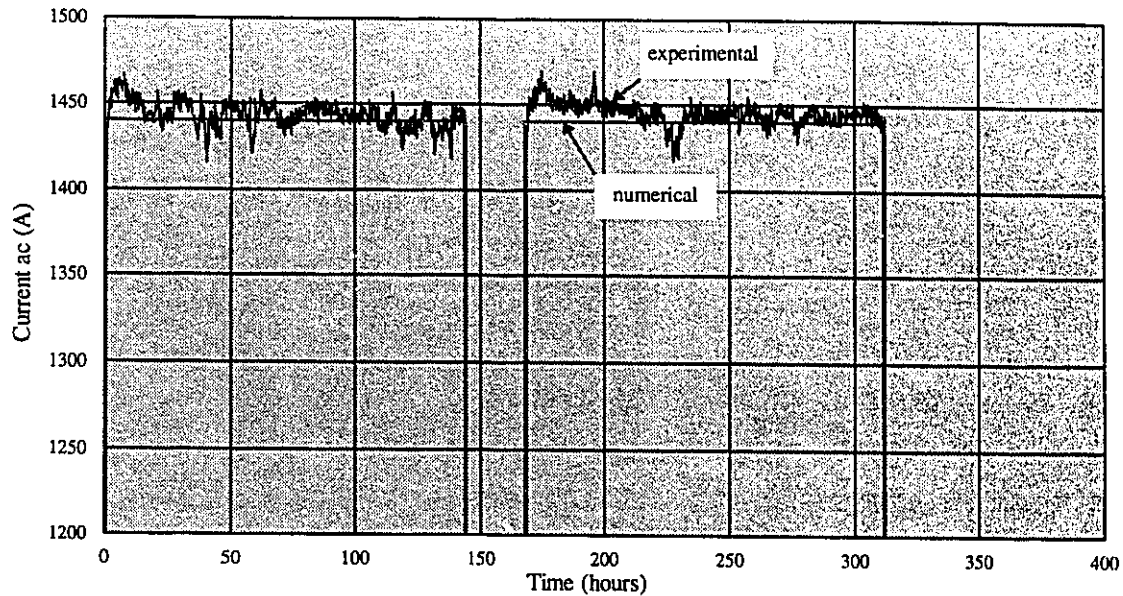


Figure 5.6 Experimental and numerical heating current levels in the demonstration test

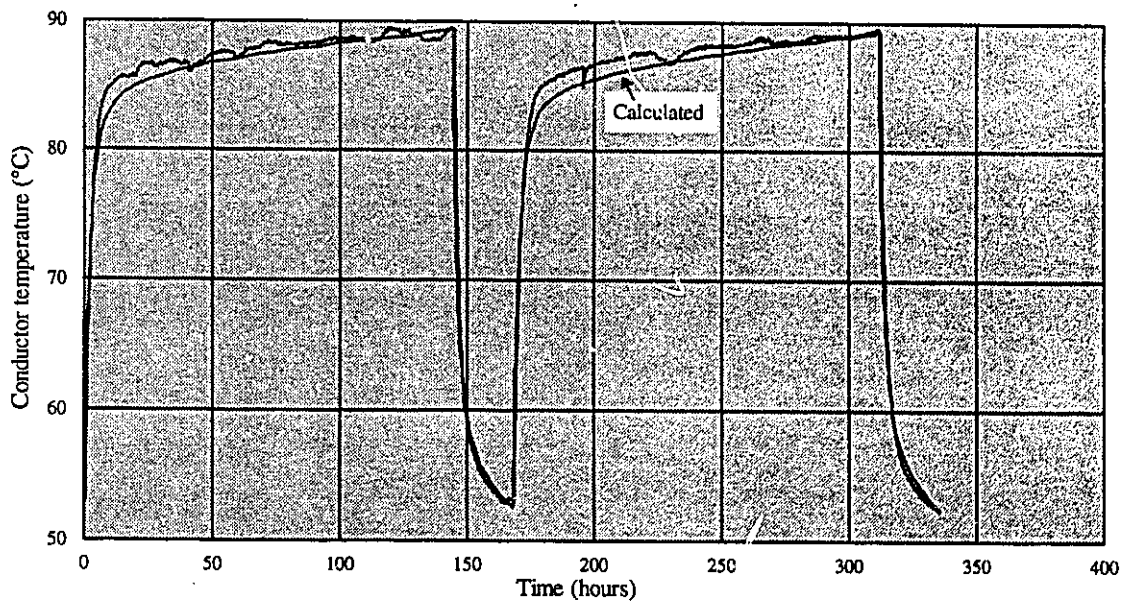


Figure 5.7 Demonstration test: comparison between calculated and measured temperatures

5.1.2 Distribution Duct Bank

The experimental duct bank at IREQ was built to test the current-carrying capacity of medium voltage distribution cables. The duct bank consists of a 100 m long, 20 PVC ducts of 11.4 cm inner diameter and 0.32 cm wall thickness, arranged in 4 rows of 5 ducts each (figure 5.8). For the test purposes, 8 ducts were left empty, namely: duct #1,#2,#6,#7,#11,#12,#16 and #17. Each of the remaining ducts is populated by three 25 kV cables representing the phases A, B and C of an AC electric circuit. The measurement stations were instrumented by thermocouples and thermal conductivity sensors. The cross-section of the duct bank and the average thermal conductivity values for the various materials present are shown in figure 5.9.

During one month, the load of the cables was modulated on an hourly basis to simulate the real life load cycle of a particular Canadian utility (figure 5.10). This cycle represents

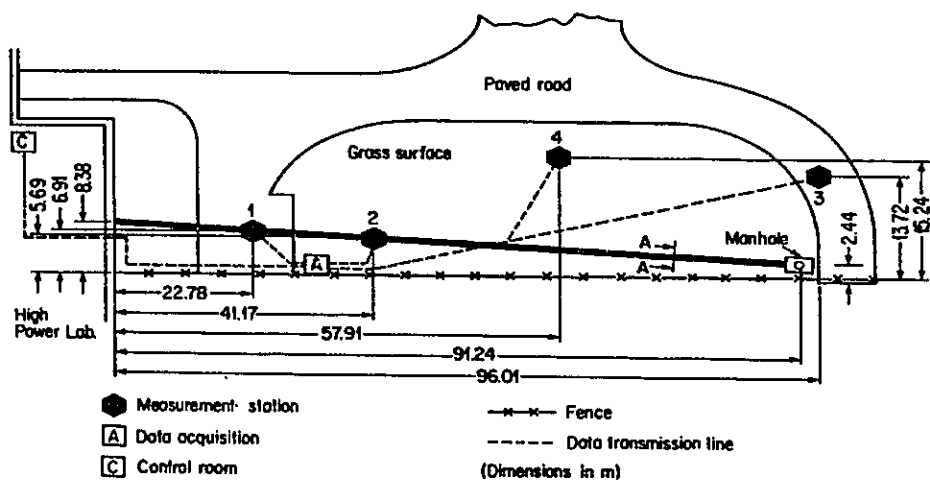


Figure 5.8 IREQ's experimental duct bank

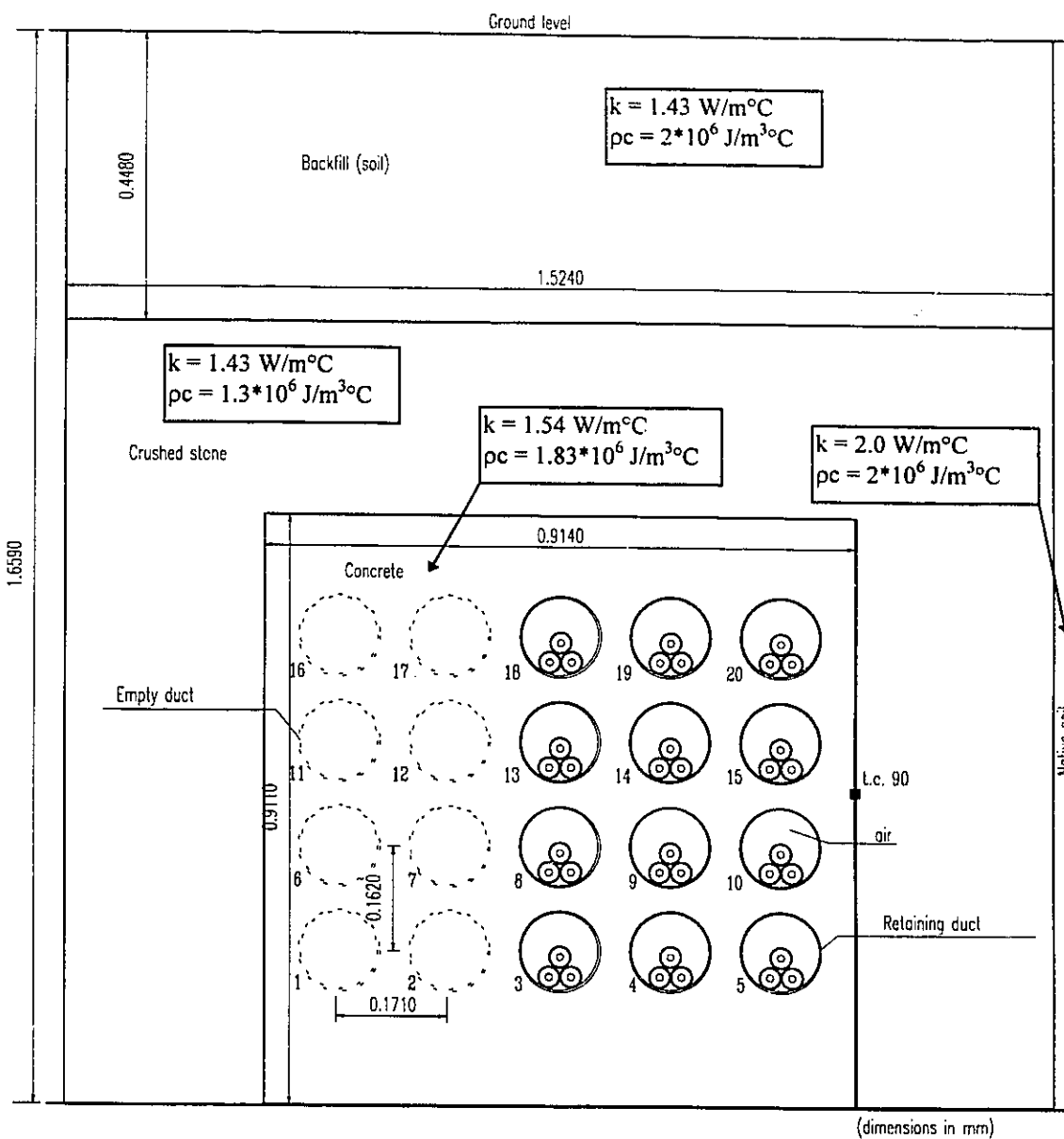


Figure 5.9 Cross-section of IREQ's experimental duct bank

the pattern of daily energy consumption in residential areas where the load is at its lowest level during night times and rises to the maximum in the middle of the day.

Figures 5.11 and 5.12 show a comparison between the calculated and the measured surface temperature of the hottest cable in the duct bank (duct # 14) and the coldest one located in duct #18. Comparisons at other locations in the duct bank are shown in figures 5.13 to 5.16. The sharp drop in cable surface temperature that occurred around the sixth day of the test, as can be seen in these figures, was caused by an accidental power failure that lasted for two hours.

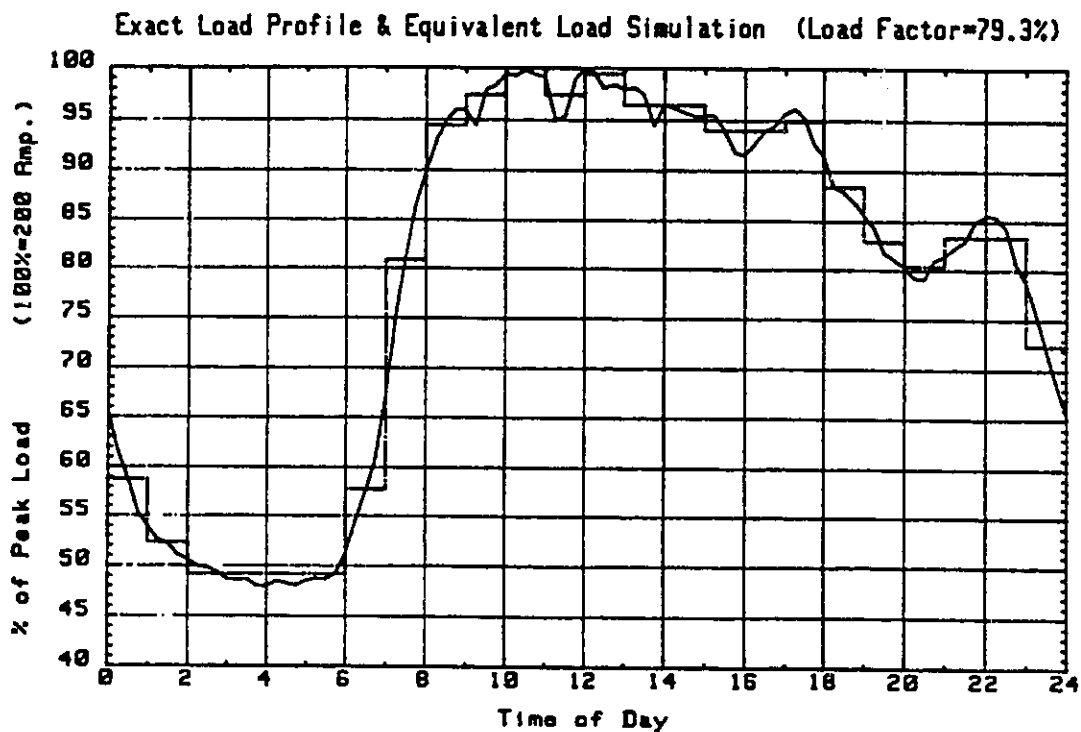


Figure 5.10 Applied daily load cycle

In this analysis, the 8 empty ducts are considered as ducts populated with unloaded fictitious cables. This approach gives similar results to the more general one that considers these boundaries (ducts' internal surfaces) to be exposed to closed cavity convection, conduction and radiation. We recall from chapter 2 that the heat exchange

inside a cavity (closed boundary) can be modeled by calculating, at each iteration, an average wall temperature that is imposed as a fictitious ambient temperature for an equivalent open boundary. We recall also that this complex calculation may be further simplified by using an empirical procedure based on the fictitious cable approach.

The air gaps between cables and retaining ducts are accounted for by including them in the finite element mesh. Thus, we make sure that these regions are actively participating in the global heat dissipation process. This procedure leads implicitly to an increase in the size of the heat path between the heat source and the heat sink (atmosphere), resulting in a lower cable temperature. Inversely, a higher cable temperature is obtained when using the conventional procedure (Heat Flux Approach) that considers the empty ducts as insulated boundaries and the other populated ducts as boundaries exposed to constant heat flux that is equivalent to the cables' losses.

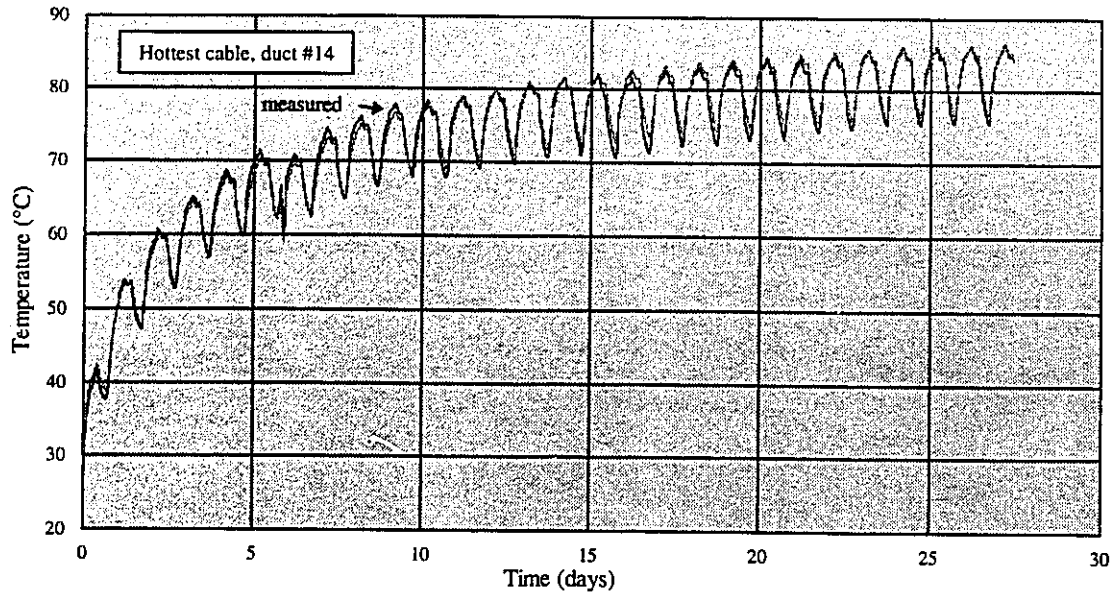


Figure 5.11 Comparison between numerical and experimental results
(hottest cable, duct #14)

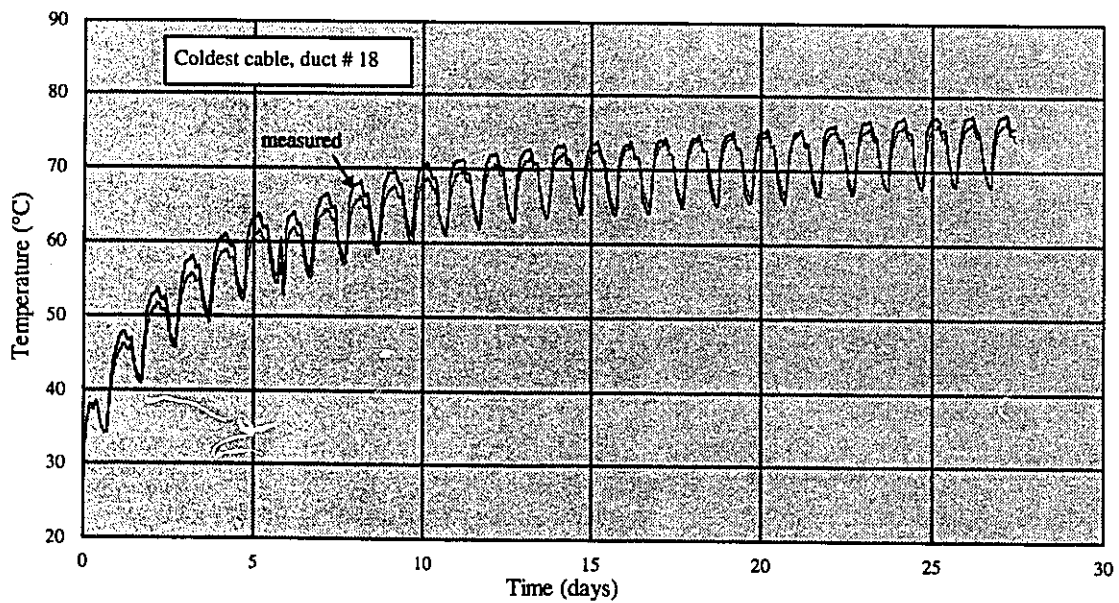


Figure 5.12 Comparison between numerical and experimental results
(coldest cable, duct #18)

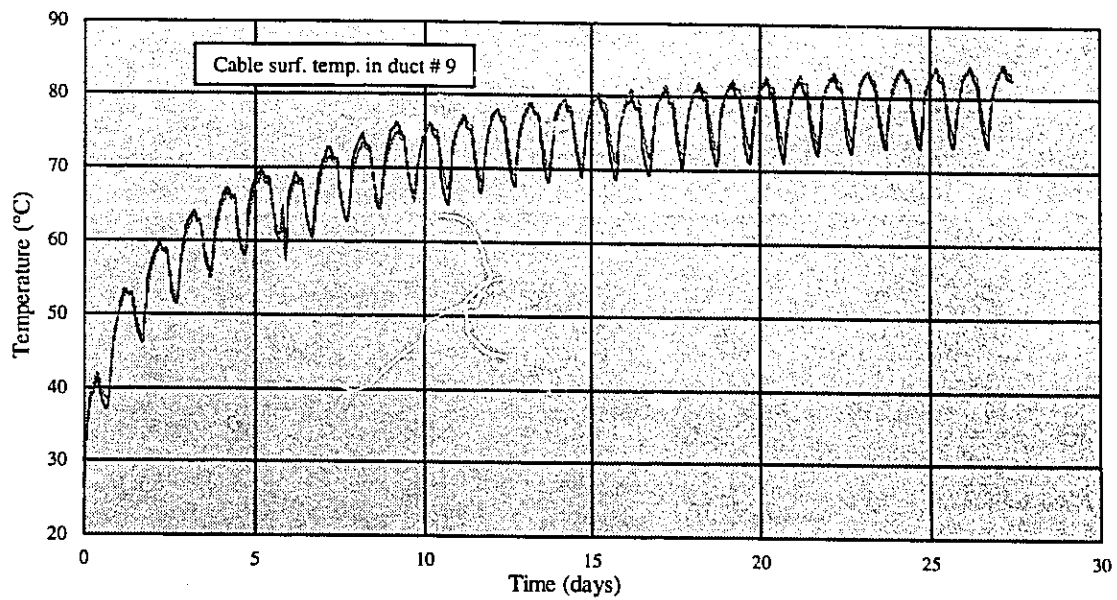


Figure 5.13 Comparison between numerical and experimental results
(cable surface temperature in duct #9)

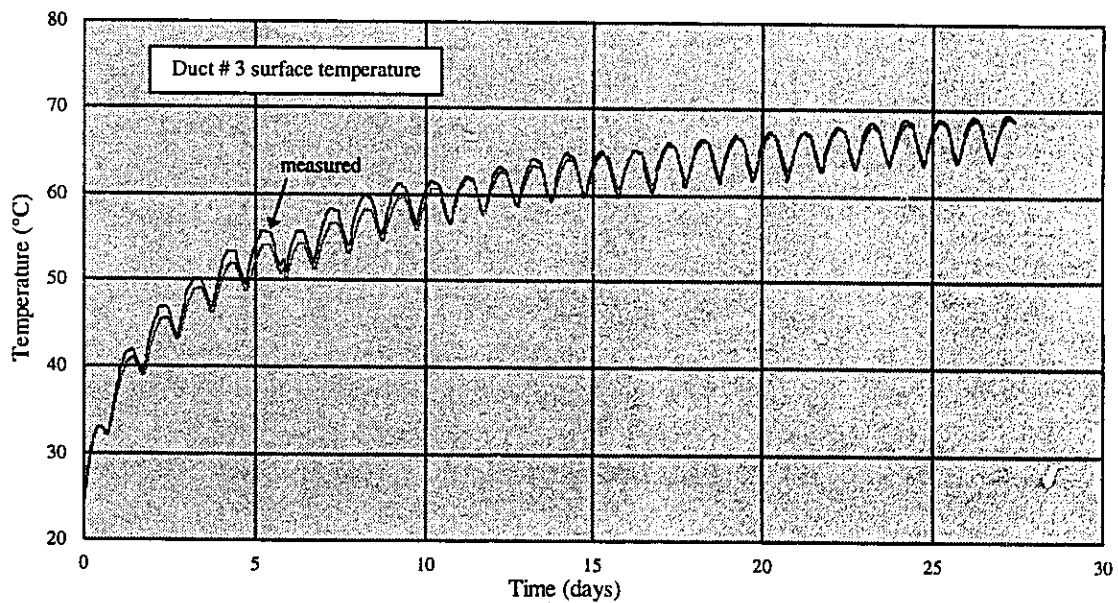


Figure 5.14 Comparison between numerical and experimental results
(surface temperature of duct # 3)

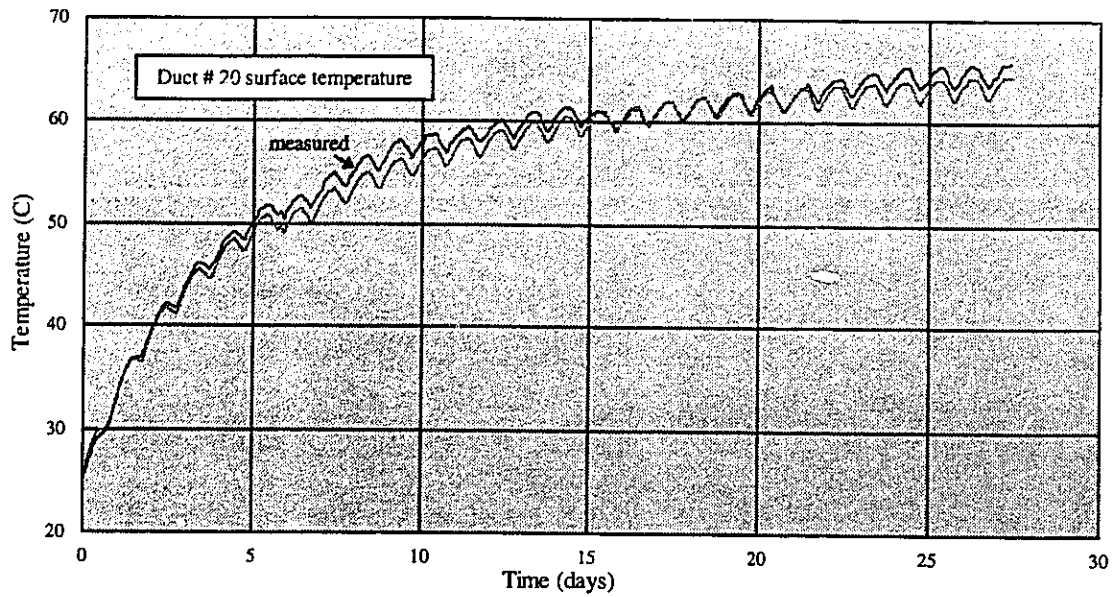


Figure 5.15 Comparison between numerical and experimental results
(surface temperature of duct # 20)

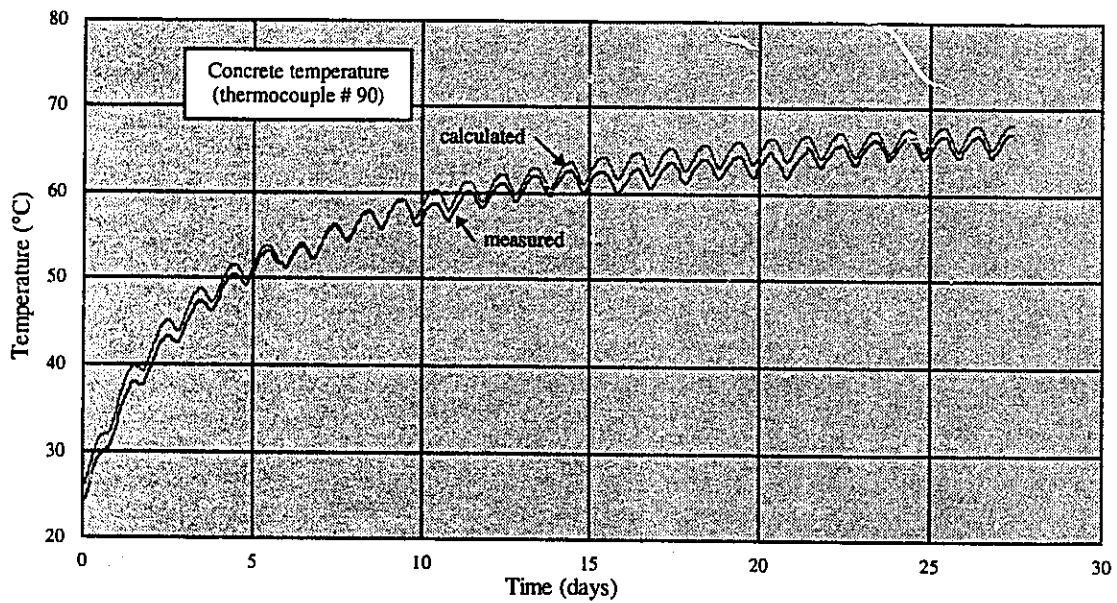


Figure 5.16 Comparison between numerical and experimental results
(Side wall of the concrete backfill: thermocouple #90)

5.2 Verification in Laboratory Installations

A laboratory mockup was built to verify the present finite element development, under stable ambient conditions, in steady-state and transient regimes. The mockup consists of a 3.66 m long sand box (figure 5.17), inside which, a 3 by 3 or 1 by 3 duct arrangements can be made. A constant temperature boundary condition can be maintained at both

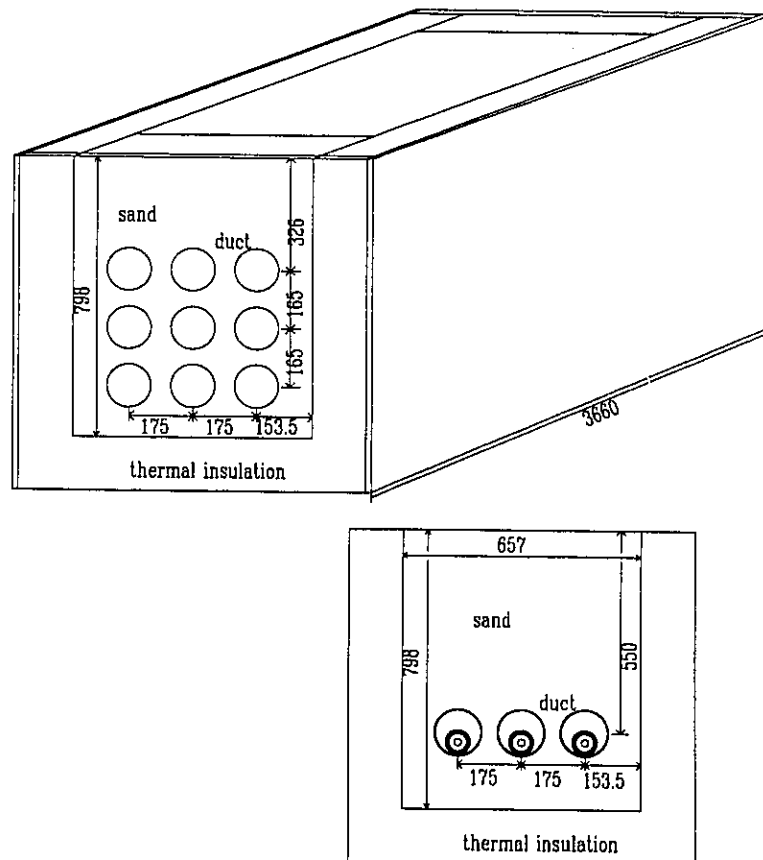


Figure 5.17 Experimental laboratory mockup

vertical walls and at the bottom wall by forced cooling. This is accomplished by circulating cold water inside copper tubes welded to a thick copper plate. During the tests, the water circulation was switched off since the presence of the copper plate alone was sufficient to ensure a closely uniform wall temperature along this boundary.

To avoid using high voltage and large circulating current as it is the case in full-size installations, the real cables were replaced by cylindrical metallic tubes of similar dimensions fitted with heating elements in the center. With this arrangement, only a current of few amperes is necessary to bring the cables' temperatures up to the desired values. The dielectric material of the real cables was replaced by fine sand having similar thermal characteristics.

Over 60 thermocouples were installed at strategic locations on and around the cables. The mockup was insulated at both ends to simulate a long cable route and consequently restricts the analysis to a two-dimensional case. The ducts can be populated by cables or can be left empty in order to simulate most of the existing real life installations.

The thermal conductivity of the sand layer in the mockup was measured by thermal needles. Its thermal capacity was measured by the calorimetric technique. The thermal characteristics of the other materials (copper and insulation) were taken directly from the

literature. In summary, the material thermal properties that have been adopted in the analysis are given in table 5.1.

	thermal conductivity (W/m°C)	thermal capacity (J/m ³ °C)
sand	0.26 - 0.27	1 200 000
insulation (vertical walls)	0.032	25 000
insulation (bottom wall)	0.04 - 0.044	25 000
copper	370.0	3 500 000

Table 5.1 Thermal characteristics of the mockup materials

It should be noted that the thermal conductivity of the insulation layer that has been used for the bottom wall was higher than the one of the side walls. This can be explained by the mechanical compression sustained by this layer during the instrumentation work (foot pressure).

Testing in the mockup went on for one year with 2 different configurations: a 1 by 3 duct arrangement to simulate transmission networks where cables are usually laid down in one row, and a 3 by 3 duct arrangement to simulate various typical distribution duct banks.

5.2.1 1 by 3 Duct Configuration

Several tests were conducted with this arrangement at various power levels in steady state and transient regimes. Additional tests were also done to examine the effect of unloaded cables and empty ducts on cable current-carrying capacity.

5.2.1.1 Steady-State, Cables Equally Loaded

This test was conducted with 4.5 Amp DC current, circulating through the heating elements of the cables connected in series. The test lasted for one month which was necessary to reach the steady-state condition. Figure 5.18 shows the finite element mesh of this arrangement (mesh of the air gaps and cables is not shown). The comparison between measured and calculated temperatures at various locations is quite satisfactory as shown in figure 5.19. The measured cable temperatures of 84.0, 87.7 and 84.5°C for the left, middle and the right hand sides cable is in good agreement with the calculated values of 84.0, 87.6 and 84.0°C, respectively.

The conventional analysis based on the Heat Flux Approach leads to higher cables' temperatures as expected (95.5°C instead of 87.7°C for the middle cable). This is caused by the exclusion of the air gaps from the global heat dissipation path. We recall from chapter 2 that this approach considers the heat losses in the cable to be imposed as a constant heat flux boundary condition at the wall of the retaining duct. Consequently, the region inside this boundary is automatically excluded from evacuating the heat generated in other ducts elsewhere in the installation.

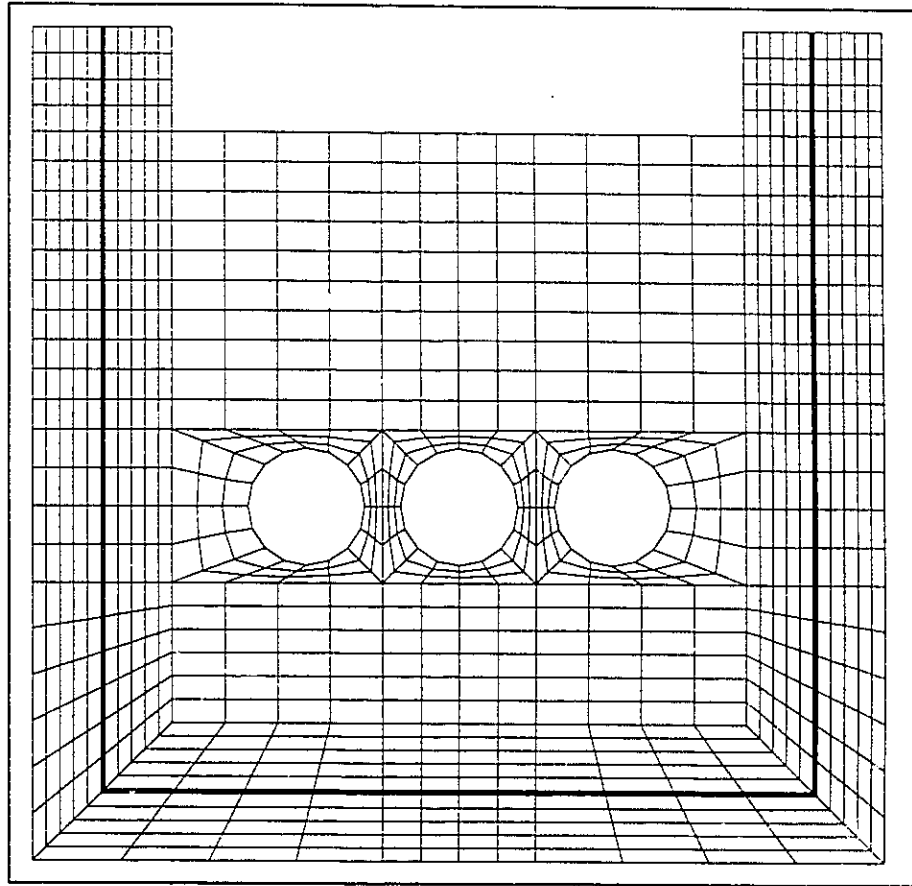


Figure 5.18 Finite element mesh of the mockup (configuration 1 by 3)

It can be seen that the difference between measured and calculated temperatures, based on the conventional Heat Flux Approach, is quite significant. In large duct bank installations, having several rows and columns, this difference may reach much higher levels as it will be noticed in the case of 3 by 3 duct configuration.

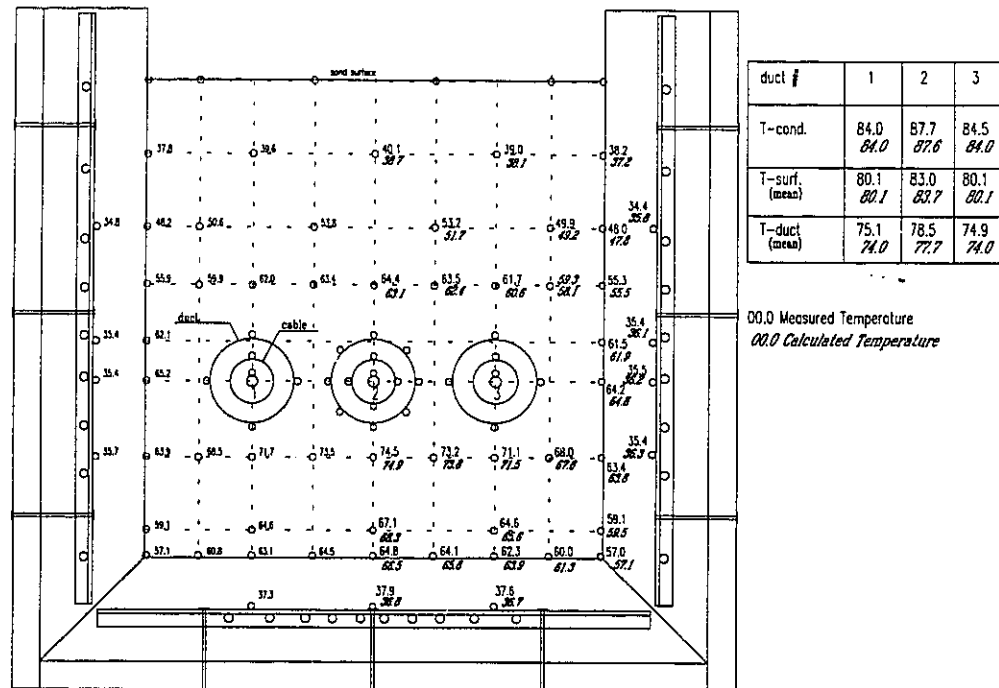


Figure 5.19 Comparison between numerical and experimental results
(steady-state, cables equally loaded, configuration 1 by 3)

5.2.1.2 Steady-state, middle cable unloaded

This test was conducted with the same power level as the previous one. A 4.5 Amp DC current was circulated in the cables located on the left hand side and on the right hand side of the mockup. The cable in the middle was left in place but kept unloaded. Again, the comparison between the calculated and measured temperatures is quite satisfactory as shown in figure 5.20.

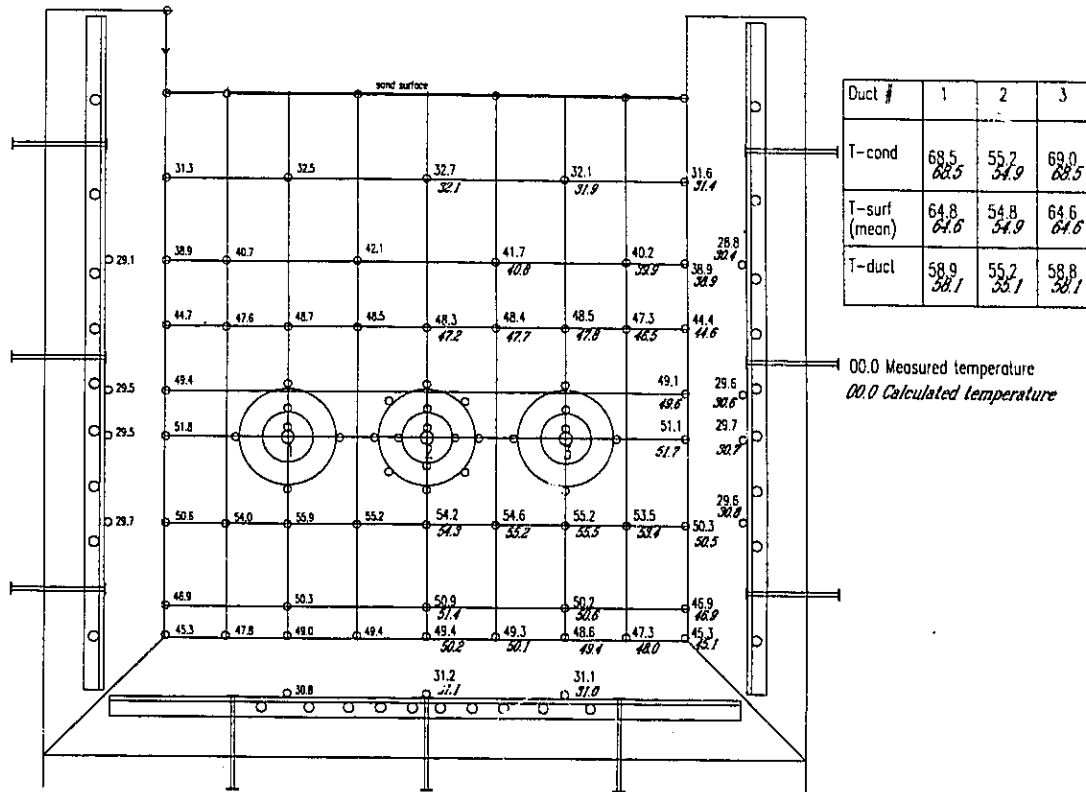


Figure 5.20 Comparison between numerical and experimental results (steady-state, cables unequally loaded, configuration 1 by 3)

At the end of this test, the middle cable was removed to simulate the effect of an empty duct. After 10 days of continuous loading, the test was stopped after no temperature variation was detected with respect to the previous temperature distribution that prevailed before removing the cable. This suggests that the empty ducts can be handled adequately, not only by the open boundary approach (boundary exposed to convection, conduction and radiation), but also by a much simpler approach that considers the empty duct as a populated one with a fictitious unloaded cable.

5.2.1.3 Transient Test, Middle Cable Unloaded

A load cycling test was conducted by varying the current according to the load cycle shown in figure 5.10. The calculated temperatures of the hottest cable and its retaining duct follow closely the measured temperatures as shown in figure 5.21.

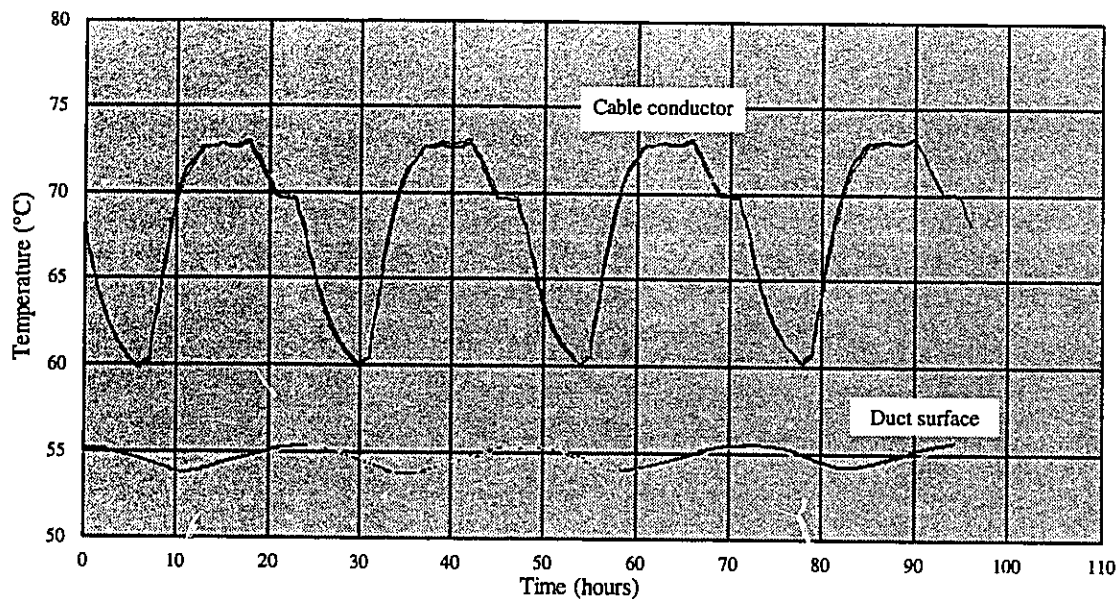


Figure 5.21 Comparison between numerical and experimental results
(Cyclic loading, cables equally loaded, configuration 1 by 3)

At the end of this test, an emergency condition was simulated by increasing suddenly the load to 5 Amp in the left hand side cable and to 6 Amp in the right hand side cable, while the middle one was kept unloaded. Two days later, the power was switched off to let the cables cool down. The comparison between the measured and calculated cables' temperature variation with time is shown in figure 5.22. A good agreement can be seen for the right hand side cable and for the unloaded one but not for the hottest cable. It is believed that the reason for that discrepancy may be due to the heating element which is made from Manganen that had an unstable electric resistance around 85°C, leading to a

relatively large change in Joule heat loss. This resistance is practically independent of temperature below 85°C.

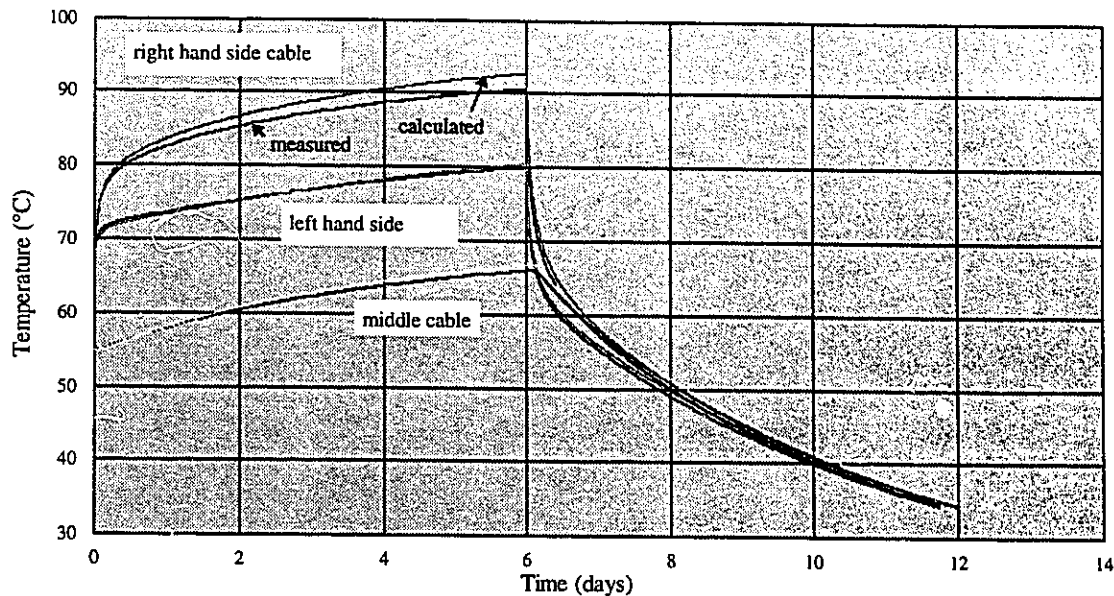


Figure 5.22 Comparison between numerical and experimental results (emergency loading, cables unequally loaded, configuration 1 by 3)

5.2.2 3 by 3 Duct Configuration

Having completed the 1 by 3 duct arrangement tests, the sand was removed and the mockup was modified to accommodate 9 ducts arranged in 3 rows by 3 columns. This configuration represents the great majority of full-size duct bank installations encountered at Hydro-Québec. The finite element mesh of this setup is shown in figure 5.23.

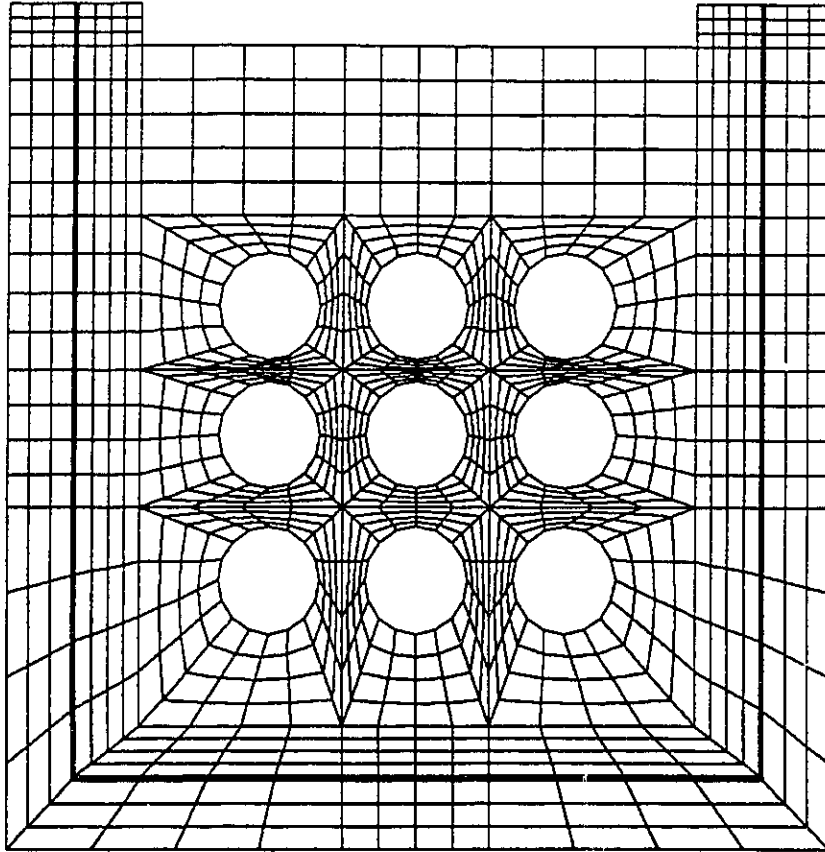


Figure 5.23 Finite element mesh of the mockup (configuration 3 by 3)

5.2.2.1 Steady-State, Cables Equally Loaded

In this test, a 2.7 Amp DC current was circulated across the heating elements of the 9 cables, connected in series. It took one month to reach the steady-state condition. The comparison between the calculated and the measured temperature distributions in the mockup, on and around the cables, is good as shown in figure 5.24.

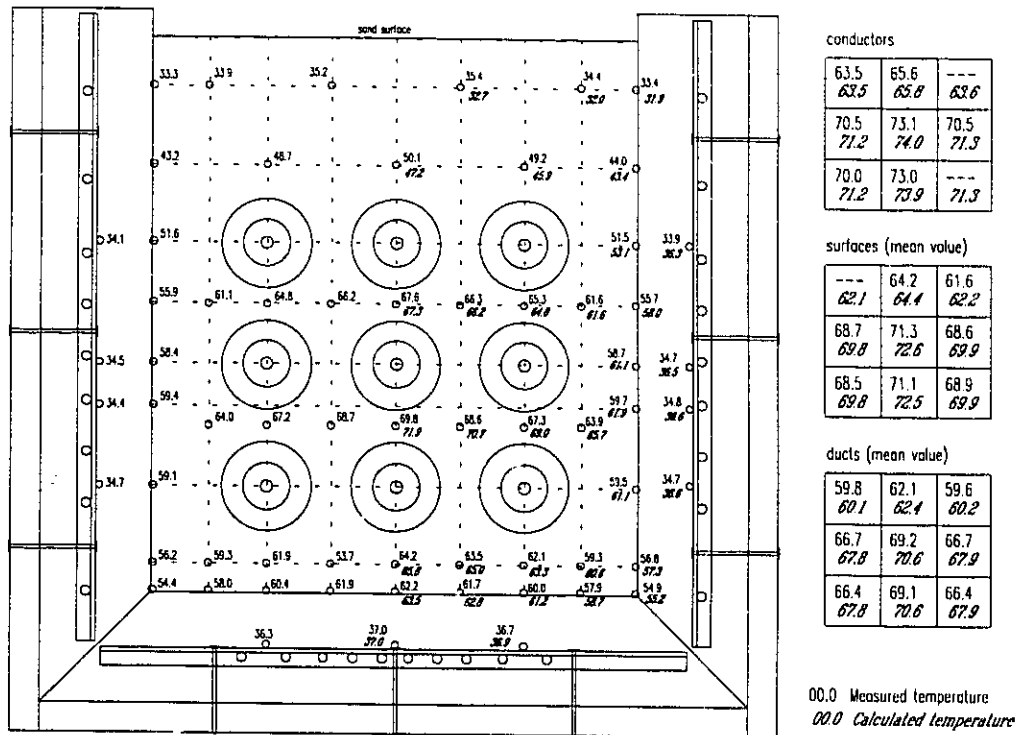


Figure 5.24 Comparison between numerical and experimental results
(steady-state, cables equally loaded, configuration 3 by 3)

As in the case of 1 by 3 duct arrangement, the calculation procedure considers the air gap between the cables and their retaining ducts as part of the heat path available to dissipate the heat generated elsewhere in the installation. This is insured by linking the finite element mesh outside the duct to the one inside the cable as has been explained in chapter 3. An equivalent thermal conductivity was assigned to the air gap in order to account simultaneously for the conduction, convection and radiation, as explained in chapter 2.

In order to demonstrate the importance of the role played by the air gaps on the overall heat dissipation, a conventional analysis (Heat Flux Approach) of the same mockup configuration was done by specifying a constant heat flux boundary condition at the walls of the ducts. The heat flux is calculated based on the heat losses inside these ducts. In this case, the difference between the calculated and measured maximum cable temperatures was found to be as high as 18.8°C for the hottest middle cable and 5.2°C for the cable on the left of the upper row.

5.2.2.2 Steady-State, Cables Unequally Loaded

In the first part of this test the power in the upper row of the mockup was switched off but the cables were left inside the ducts. At the end of 30 days of testing, with a DC current of 2.7 Amp circulating in the other 6 cables, the steady-state was reached. The comparison between calculated and measured temperature values is quite satisfactory as indicated in figure 5.25.

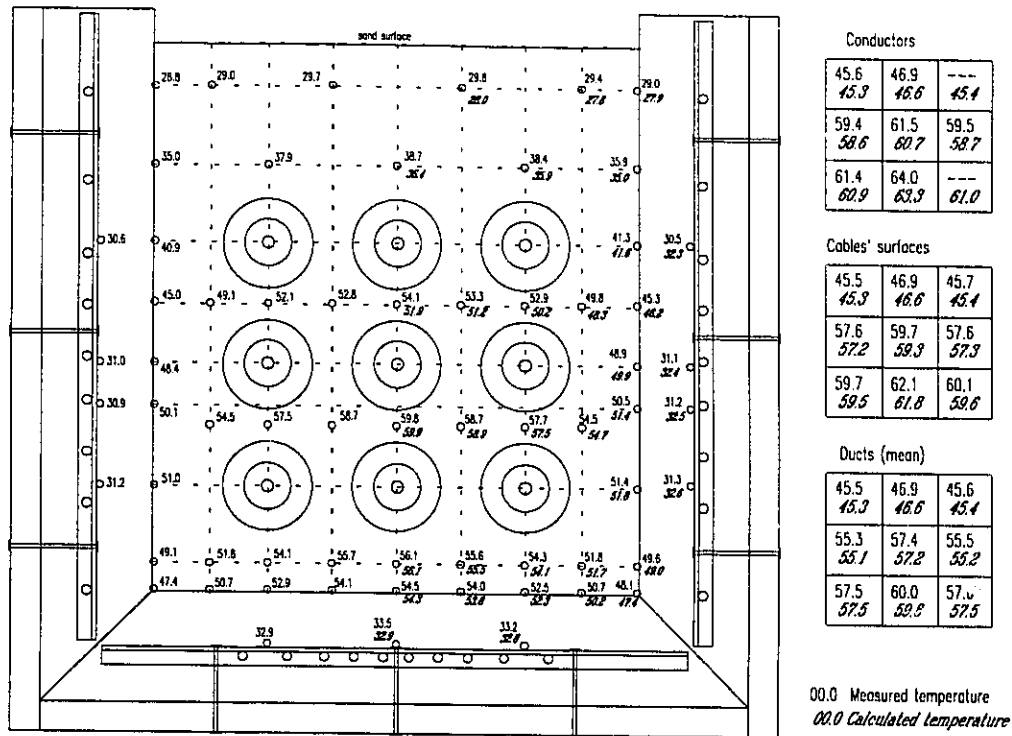


Figure 5.25 Comparison between numerical and experimental results (steady-state, cables unequally loaded, configuration 3 by 3)

In the second part of this test, the cables in the upper row were removed to examine the effect of empty ducts on the overall heat dissipation. No variation in the temperature distribution was detected, even after 20 days of testing under these conditions. This suggests, as it was found in the case of 1 by 3 duct configuration, that empty ducts can be simulated accurately by ducts that are populated with fictitious unloaded cables. In this case, the conventional Heat Flux Approach, which considers the empty ducts as insulated boundaries and the populated ducts as boundaries exposed to constant heat flux,

introduces a much greater difference between the measured and calculated temperatures when compared to the case of one row installation discussed previously. This difference may exceed 20°C, which is unacceptable.

5.2.3 Cables Exposed to Air

In practice, cable routes are usually composed of several sections located underground and of some sections exposed to ambient air and sun. Along the exposed sections, the cables are either naked or installed in a protective ducts. Several tests in the laboratory were conducted to cover both configurations. In the first case, where cables are exposed directly to ambient, the heat transfer mechanism between the cable and the air is well documented in the literature. It is a simple case of heat dissipation from a horizontal or a vertical heated cylinder to the ambient. Figure 5.26 shows a comparison between the calculated and measured temperature variation in time, in the case of a horizontal cable subjected to two steps load profile.

The more challenging case is the one where the cables are located inside a protective duct in either concentric or eccentric positions. In chapter 2, details are given about the way to evaluate the heat exchange between the cable and the retaining duct and also the procedure to include this part in the global finite element analysis. In this approach, the thermal resistance across the air gap caused by convection, conduction and radiation heat transfer, is calculated by adding the individual effects of each heat transfer mechanism.

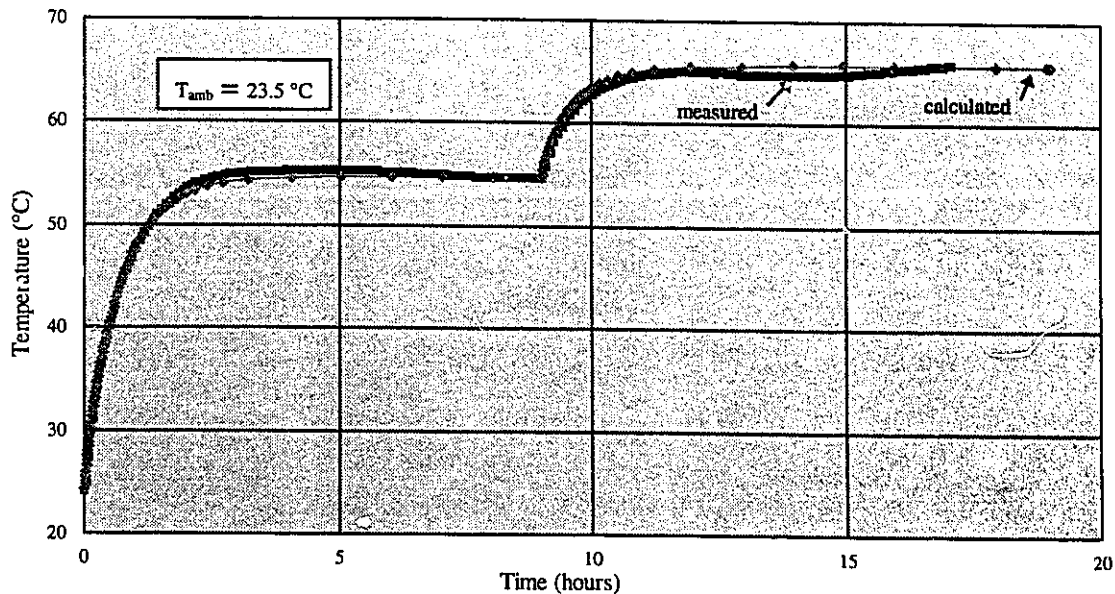


Figure 5.26 Comparison between numerical and experimental results
(transient analysis, cable naked exposed to air)

An equivalent thermal conductivity of the air space is calculated based on the outside diameter of the cable, inside diameter of the retaining duct and on the thermal resistance across the air gap. Several tests were conducted at various power levels with a concentric cable-duct arrangement and with the cable laying at the bottom of the duct. It was found that, for the same load conditions, the position of the cable inside the duct had little effect on its temperature (table 2.3). This finding supports the assumption discussed in chapter 2 where eccentric cable-duct configuration was simulated by a cable located in the middle of the duct. Figure 5.27 shows the comparison between the calculated and measured temperature variation of the cable conductor in the case of cable in duct.

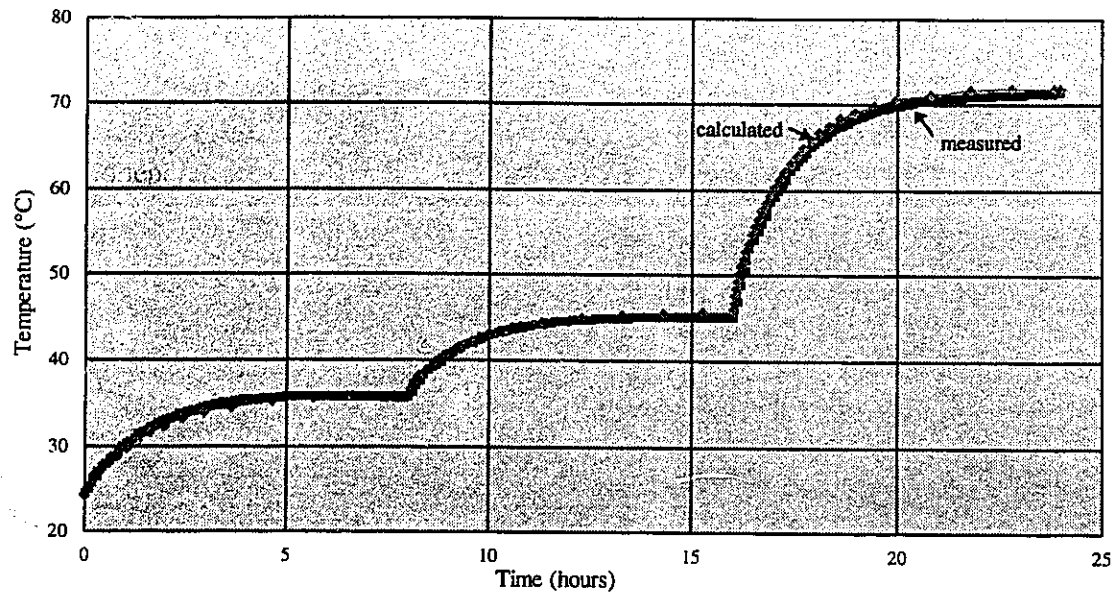


Figure 5.27 Comparison between numerical and experimental results
(transient analysis, cable in duct exposed to air)

6. Conclusions and Recommendations

6.1 Conclusions

This study focused on analyzing the complex heat transfer that takes place inside scattered cavities in solid bodies. The cavities are either empty or populated by some form of heat generating elements. Although such cavities may be encountered in various engineering problems, the present work was focused on their effects on the calculation of current-carrying capacity (ampacity) of underground cable installations. In this field, the ampacity analysis has traditionally been carried out by the analytical method of Neher-McGrath which suffers from several limiting assumptions and simplifications that affect its accuracy and limit its use to the analysis of simple geometries. One of these handicaps is its inability to accommodate empty ducts in the installation. The presence of such ducts, even in small number, however, can significantly affect the results of the analysis if they are not treated adequately.

The finite element technique, used in this study, was shown to give accurate ampacity calculations when compared to the results obtained from dozens of experimental tests conducted in full-size installations and in a laboratory mockup. In this study, we have introduced a new approach to cable ampacity calculation dubbed EFECAC (Economic Finite Element Cable Ampacity Calculation). This approach has the advantage of reducing significantly the size of the problem while maintaining the accuracy compared

to the Full-Mesh Approach. In the latter, the cable and the surrounding domain are fully meshed in a Cartesian coordinates system while, in the proposed one, the cables are meshed independently in a one dimension less polar coordinates system.

The second important development carried out in this study is the integration of the air gaps between cables and ducts into the domain of the analysis. In the conventional Heat Flux Approach, where heat losses in the cables are imposed as a constant heat flux boundary condition on the duct walls, the results of the analysis can deviate quite significantly from the real measured values.

Another perceived contribution is the analysis of the empty ducts located in distribution duct banks. We have shown that the complex analysis by Navier-Stokes and energy equations can be replaced by two simpler procedures. The first one consists in treating these ducts as open boundaries exposed to convection and radiation, the bulk temperature in this case being calculated by averaging the cavity wall temperatures at each iteration. The second approach consists in considering a small fictitious unloaded cable inside these ducts which considerably simplifies radiation calculations and finally yields a conduction equivalent problem. These approaches have, therefore, the advantage of being simpler to implement in computer programming and requiring less computing time.

The introduced computer programs based on the various developments described in this thesis represent an important step in improving the accuracy of the analysis of

underground cable installations, especially for Hydro-Québec, where they are actually in use for optimizing and designing existing and future underground installations.

In addition, the extensive experimental verifications carried out in the field and laboratory have proven the reliability and flexibility of these programs to treat complex problems with relative ease.

6.2 Recommendations

In the present development, the heat transfer in the surrounding native soil and backfills was treated as pure conduction. The thermal conductivity and thermal capacity of these materials depend on their granular composition, their compacting rate and their moisture content. Therefore, these properties must be measured or estimated for each of the individual material present in a duct bank. For a design purpose, it is common to conduct a thermal conductivity survey along the cable route and then to consider the worst conditions. During operation, the heat generated in the cables drives the moisture away leading sometimes to an important drop in thermal conductivity. This phenomenon is more pronounced in the case of intense heat flux emanating from the cables (during emergency for example). The moisture migration in porous media, the effect of various parameters and the ability of these media to retain their moisture under intense heat flux is a study worthwhile pursuing. The analysis of this problem requires a coupled solution

of the heat and mass transfer partial differential equations, as well as physical and chemical characterizations of the materials.

Some of the simplifications considered in this study, namely replacing a three phase cable installation by a single one and neglecting the cable/duct eccentricity effect, were validated experimentally. It is recommended, however, to conduct some detailed finite element analyses and to explore other methods such as the boundary integral and the finite volume techniques to solve this problem, perhaps in a more accurate manner.

In the present development, the analysis of the combined free convection radiation and conduction heat transfer was done using segregated finite element techniques. This means that the Navier-Stokes and energy equations were solved inside the cavities independently of the Fourier equation inside the solid domain. This technique has the advantage of reducing the size of the problem. Providing that one has the necessary large computing power and speed, it is suggested to solve all these equations in a coupled manner. In this case, the stream function no-penetration condition along wall cavities must be assigned different values, one for each cavity or duct that are present in the installation. A proper formulation must be derived to uniquely determine these stream function values, as has been done for the multiply connected problems of viscous flow over an arbitrary airfoil or over multiple airfoils [31].

The proposed finite element code to solve the cable ampacity problem is limited to 2D cases which generally covers most underground installations. However, for more general applications, it is recommended to develop a 3D version in the future.

References

- [1] Neher J.H. and McGrath M.H., "Calculation of the Temperature Rise and Load Capability of Cable Systems", *AIEE Transactions*, Vol. 69, pp. 752-772, 1957.
- [2] Kennelly A.E., "On the current Carrying Capacity of Electric Cables Submerged, Buried or Suspended in Air", *Minutes, Ninth Annual Meeting, Association of Edison Illuminating Companies*, N.Y., 1893.
- [3] Cyme International Inc., "Cable Ampacity Program (CAP)", *Canadian Electrical Association*, Contract #138 D 375C, December 1991.
- [4] Anders G.J., "Advanced Computer Programs for Power Cable Ampacity Calculations", *IEEE Computer Applications in Power*, Vol. 3, No. 3, July 1990.
- [5] De Vahl Davis G. and Jones J.P., "Natural Convection in a Square Cavity: a Comparison Exercise", *International Journal for Numerical Methods in Fluids*, Vol. 3, pp. 227-248, 1983.
- [6] Tsui Y.T. and Tremblay B., "On Transient Natural Convection Heat Transfer in the Annulus Between Concentric Horizontal Cylinders with Isothermal Surfaces", *Int. J. Heat Mass Transfer*, Vol. 27, No. 1, pp. 103-111, 1984.
- [7] Roache P.J., "Computational Fluid Mechanics" Hermosa Publishers, Albuquerque, New Mexico, 1972.
- [8] Dhatt G., Fomo B.K. and Bourque C.A., "A ψ - ω Finite Element Formulation for the Navier-Stokes Equations", *International Journal for Numerical Methods in Engineering*, Vol. 17, pp. 199-212, 1981.
- [9] Stevens W.N., "Finite Element Stream Function-Vorticity Solution of Steady Laminar Natural Convection", *International Journal for Numerical Methods in Fluids*, Vol. 2, pp. 349-366, 1982.
- [10] Campion-Renson A. and Crochet M.J., "On the Stream Function Vorticity Finite Element Solutions of Navier-Stokes Equations", *International Journal for Numerical Methods in Engineering*, Vol. 12, pp. 1809-1818, 1978.
- [11] Peeters M.F., Habashi W.G. and Dueck E. G., "Finite Element Stream Function-Vorticity Solution of the Incompressible Navier-Stokes Equations", *International Journal for Numerical Methods in Fluids*, Vol. 7, pp. 17-27, 1987.

- [12] Habashi W.G., Peeters M.F., Guevremont G. and Hafez M.M., "Finite Element Solutions of the Compressible Navier-Stokes Equations", *AIAA Journal*, vol. 25, No. 7, pp. 944-948, July 1987.
- [13] Chaaban M. and Bédard N., "Heat Transfer Between Cables and Retaining Duct in an Electrical Distribution System", *A.S.M.E. paper 85-HT-11*, 1985.
- [14] Huebner K. H., "The Finite Element Method for Engineer". 2nd edition, John Willey & Sons, 1983.
- [15] Siegel R. and Howel J.R., "Thermal Radiation Heat Transfer", McGraw-Hill, 1972.
- [16] Buller, F.H. and Neher J.H., "The Thermal Resistance Between Cables and Surrounding Pipe or Duct Wall", *AIEE Transactions*, Vol. 69, pp. 342-349, 1950.
- [17] McAdams W.H., "Heat Transmission", McGraw-Hill, 3rd edition, New York, 1954.
- [18] Kuehn T.H. and Goldstein R.J., "An Experimental and Theoretical Study of Natural Convection in the Annulus Between Horizontal Concentric Cylinders", *J. Fluid. Mech.*, Vol. 74, pp. 695-719, 1976.
- [19] Cho C.H., Chang K.S. and Park K.H., "Numerical Simulation of Natural Convection in Concentric and Eccentric Horizontal Cylindrical Annuli", *ASME Transactions*, Vol. 104, pp. 624-630, 1982.
- [20] Farouk B. and Guceri S.I., "Laminar and Turbulent Natural Convection in the Annulus Between Horizontal Concentric Cylinders", *Journal of Heat Transfer*, Vol. 104, pp. 631-636, 1982.
- [21] Chaaban M., Habashi W.G. and Leduc J., "A New Approach to Cable Ampacity Calculation Using the Finite Element Method", *IEEE, Proceedings of the 91st meeting of the insulated conductors committee*, Chapter 22, Birmingham, England, July 1992.
- [22] Chaaban M., Habashi W.G. and Leduc J., "A finite Element Approach for Coupling Axisymmetric and Cartesian Domains in Underground Cable Calculations", *Proceedings of the Numerical Methods in Heat Transfer conference*, Pineridge Press, pp. 1565-1575, 1993.
- [23] Chaaban M., Leduc J. And Royer C., "User-Friendly Package of Finite Element Programs for Cable Ampacity Calculation in Complex Installations", *IEEE, Special ICC Meeting in Birmingham, UK*, July 1992.

- [24] Chaaban M., Leduc J. and Belec M., "Logiciel TEMPCAB : Calcul de l'Échauffement des Câbles Haute Tension en Régimes Permanent et Transitoire", *Institut de Recherche d'Hydro-Québec*, IREQ-93-315, December 1993.
- [25] Chaaban M., Leduc J. and Belec M., "Logiciel MASSIF Transitoire: Calcul de l'Échauffement des Canalisations Souterraines de Distribution", *Institut de Recherche d'Hydro-Québec*, IREQ-93-299, November 1993.
- [26] Chaaban M., Leduc J., Couderc D., Trinh N.G. and Belec M., "Evaluation of HVDC Cables for the St. Lawrence River Crossing of Hydro-Québec's 500 kV Line - Part III : Thermal Behavior", *IEEE Transmission and Distribution Conference*, Dallas, Texas, pp. 117-121, September 1991.
- [27] American Society of Heating, Refrigerating and Air Conditioning Engineers, "ASHRAE Handbook of Fundamentals", New York, 1972.
- [28] Chaaban M., "Programme de Calcul de Charge des Câbles Souterrains de Distribution", *Institut de Recherche d'Hydro-Québec*, IREQ-2791, 1984.
- [29] Chaaban M. and Leduc J., "Mise à Jour du Logiciel MASSIF: Calcul de Charge admissible dans les Câbles Souterrains de Distribution", *Institut de Recherche d'Hydro-Québec*, IREQ-4479, November 1989.
- [30] Couderc D., Trinh N.G., Belec M., Chaaban M., Leduc J. and Beauséjour Y., "Evaluation of HVDC Cables for the St. Lawrence River Crossing of Hydro-Québec's 500 kV Line - Part I : Dielectric and Accelerated Aging Test", *IEEE Transmission and Distribution Conference*, Dallas, Texas, September 1991.
- [31] Guevremont G., "Finite Element Vorticity-Based Methods for the Solution of the Incompressible and Compressible Navier-Stokes Equations", *Ph.D. Thesis*, Concordia University, Montréal, Québec, Canada, 1993.